Evaluating the Retrofit of Highway Bridges Using Fluid Viscous Dampers

by

Asim Rustum

A thesis
presented to the University of Waterloo
in fulfillment of the
thesis requirement for the degree of
Master of Applied Science
in
Civil Engineering

Waterloo, Ontario, Canada, 2012

AUTHOR'S DECLARATION

I hereby declare that I am the sole author of this thesis. This is a true copy of the thesis, including any required final revisions, as accepted by my examiners.

I understand that my thesis may be made electronically available to the public.

Abstract

Highway bridges function as the arteries of our society. Hence, it is essential that they remain operational following an earthquake. Unfortunately, a significant number of bridges worldwide, including in Canada, were constructed prior to the development of modern seismic design provisions. In many cases, such bridges are expected to perform poorly during earthquakes. According to a report published in 2000 by Ministry of Transportation of Ontario (MTO), in eastern Ontario alone, there are over 70 bridges that are structurally deficient. Current methods to retrofit these bridges to bring them into compliance with the existing codes would entail substantial structural modifications. Examples of such modifications include the replacement of existing rocker bearings with elastomeric bearings, structural strengthening of piers, and enlarging the bearing surfaces. These methods involve substantial cost, effort, and materials.

An alternative means to retrofit structurally deficient bridges is investigated in this thesis. This method involves using a combination of elastomeric bearings and fluid dampers to retrofit highway bridges. In principle, these devices work in the same way as shock absorbers in automobiles. They absorb shock and dissipate the vibration energy to the environment as heat. In the case of bridges, earthquakes impart the shock to the structure. Before these devices can be implemented in practice, there are many issues that need to be understood with respect to their performance and modelling. Moreover, a comparative assessment between popular retrofit options employing isolation systems needs to be undertaken to verify and provide a benchmark to assess their performance.

The Mississippi River Bridge near Ottawa is chosen as a test structure to conduct this study. This bridge already contains an advanced isolation system, and has an extensive documentation available for modelling and verification. Various retrofit options will be studied and compared with the existing isolation design for this bridge. In all cases, the effect of soil-structure interaction is included. A comprehensive set of performance indices are used to evaluate the performance of various retrofit options. All the models are constructed in the open source software, OpenSees.

The research demonstrates that the proposed approach is a viable retrofit method for highway bridges. Moreover, compared to advanced isolation systems, retrofit using elastomeric bearings with viscous dampers was successful on transferring lower loads to the substructure, and resulted in lower superstructure displacements. Though this study involved one bridge, it has provided a computational test bed to perform further studies and has provided valuable insight into the modeling and performance of retrofit solutions.

Acknowledgements

First, I would like to thank my supervisor Dr. Sriram Narasimhan, who accepted me as his M.Sc. student without any hesitation. He offered me advice, patiently supervising me and always guiding me in the right direction. He always welcomes us with a smile and has a solution to any problem we have or confront. Without his guidance and constant encouragement throughout this research I couldn't have finished my thesis successfully.

I would like to thank all the personnel at the University of Waterloo who were friendly, joyful, and rewarding people to work with. Thanks to all the professors who taught me, gave me knowledge, assistance and guided me throughout the M.Sc.

My sincere gratitude and appreciation to the Ministry of Transportation of Ontario (MTO) for their financial support which was essential in conducting this research work.

Finally, I would like to thank my parents who are always there for me. I am grateful for their encouragement and consistent support. I wish to dedicate this thesis to my mother and my father whose lifetimes have been devoted to my education.

Table of Contents

List of Figures

List of Tables

Chapter 1
Introduction and Objectives

1.1 Introduction

Many highway bridges in use today do not meet the current seismic design codes requirements. The high number of recent bridge failures due to seismic events (e.g. 1989 Loma Prieta and 1994 North Ridge earthquakes) has raised concerns regarding the vulnerability of bridges to earthquakes. Accordingly, the seismic demands (i.e. perceived seismic risk) by national design codes for bridges and other structures have increased over the years, in response to such failures. This leaves a large inventory of bridges that have been designed and built according to the old seismic requirements, which are now deemed structurally deficient (Priestley & Seible, 1996). There is an urgent need to retrofit such bridges and make them code compliant according to current code provisions.

Developing cost-effective and safe bridge retrofits has become one of the highest priorities for public safety today. Several researchers have developed novel retrofit methods and techniques to improve the performance of traditional retrofits. Most of the bridge failures occur at the bridge piers or columns. In most instances, nearly 80% of the bridge mass is concentrated in the bridge superstructure. This concentration of mass translates to a disproportionate concentration of lateral load in the superstructure during a seismic event. Hence, increasing the seismic resistance of a bridge requires retrofitting of the piers to withstand the higher lateral loads transferred from the bridge superstructure to the foundation. Moreover, bridge superstructures have a relatively high elevation, which results in high moment force magnitudes at the bridge footings. This over-turning moment can potentially cause bridge foundation piles to pull-out or could lead to the overturning of the bridge.

The second, perhaps more common mode of failure in moderate seismic zones such as Ontario, is the unseating of bridge supports during a seismic event. This is typically caused due to the failure of bearings, resulting in an incomplete lateral load transfer from

the superstructure to the substructure. According to a screening study by the Ministry of Transportation of Ontario (MTO) (Bagnariol & Au, 2000), there are several bridges in the Ottawa region susceptible to this mode of failure (see Figure 1).

Figure 1. Bridge unseating during a seismic event in Chile.(Yu, 2010)

The current retrofit methods to address the above vulnerabilities can be broadly classified into two categories. The first being the traditional structural strengthening approach, which includes strengthening the piers to be able to support the high lateral load resulting from the bridge superstructure, replacing the vulnerable bearings (e.g., rockers) and expanding the seat-widths to accommodate the large displacement demands. The second approach involves the use of control devices such as isolation bearings and viscous dampers to reduce the magnitude of lateral load transfer from the superstructure to the sub-structure. The basic idea in this approach is to enhance the energy dissipation of the

input seismic energy through the addition of control devices. This approach is cost-effective and could be conducted in a rapid manner for a large inventory of bridges. The focus of this thesis will be on this second approach.

The idea of using vibration isolators is to reduce the ground movement transferred from the foundation to the superstructure. Reducing the movement transferred to the bridge superstructure prevents or reduces the inertial forces in the superstructure. As a result, relatively low levels of substructure forces need to be stabilized during a seismic event. Implementing base isolation bearings lengthens the fundamental natural period of the bridge structure. This filters out the high energy components of the seismic event. The high flexibility in the isolation elements allows for large displacements in the isolation layer; however, these deformations in the isolation layer reduce the deformations in the superstructure elements.

For buildings, an isolation system is typically placed at the base of the structure, however, in bridges, the vibration isolation bearings are placed between the superstructure and the substructure of a bridge (see Figure 2). This allows for differential movement between the deck and the substructure which, consequently, reduces the deck acceleration, the force transferred to the substructure, and the deck displacement in many cases.

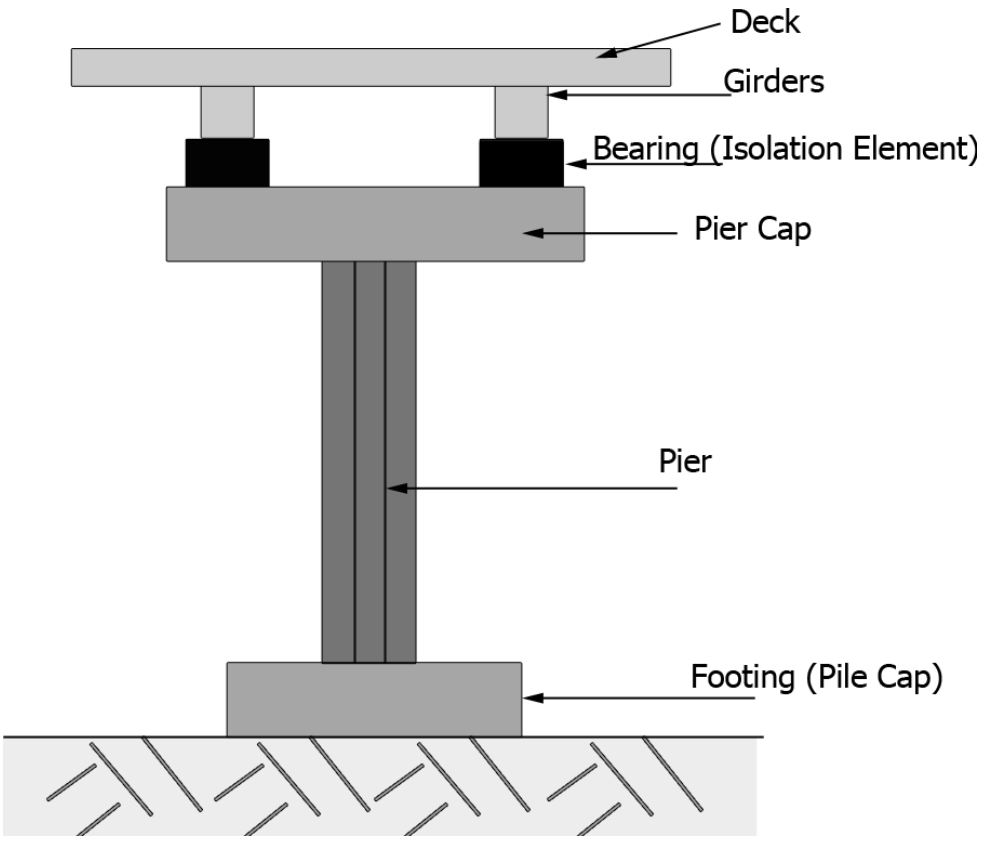

Figure 2.Vibration isolation bearings location in bridges.

Isolation bearings can be one or a combination of the following: linear system, e.g., springs and elastomeric bearings; nonlinear system, e.g., friction pendulum bearings (FPS); and elasto-plastic systems, such as bilinear steel or elastomeric bearings with lead plugs (called, lead-rubber bearings (LRBs)).

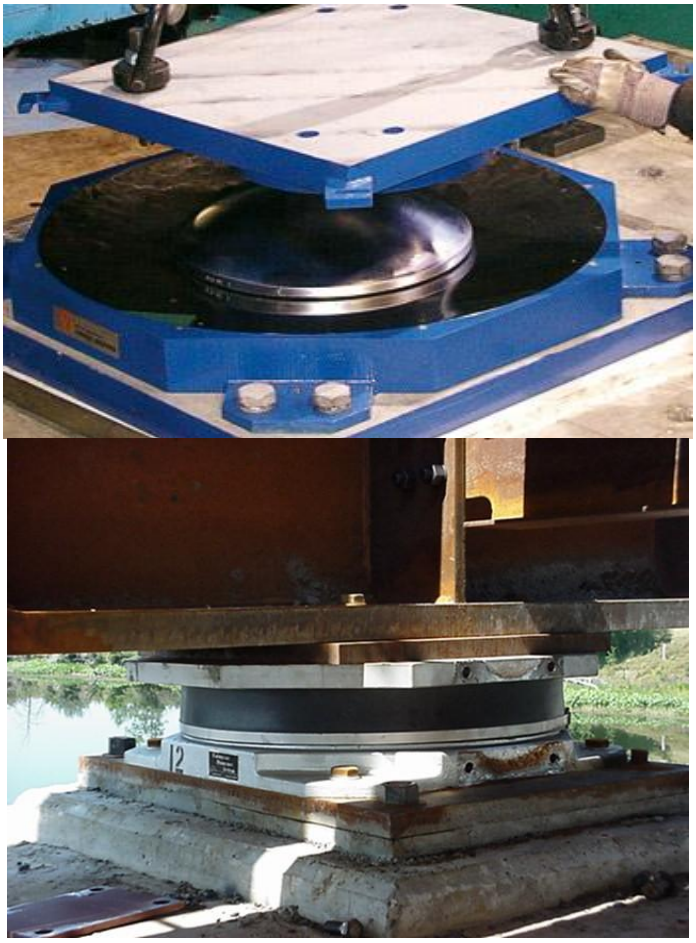

Figure 3. Friction pendulum bearings (top)(Maurer) and elastomeric bearings (bottom)(MTO, 2010)

While the use of isolation systems such as FPS and LRB have been extensively studied in the literature, they are often used in bridges located in regions of severe earth shaking (e.g., British Columbia, California). They tend to be relatively expensive and require significant design effort. In regions of moderate seismic activity, simpler options employing fluid viscous dampers in conjunction with rubber elastomeric pads may provide a viable alternative, and are worth investigating. The main advantage of this approach over LRB or FPS isolation systems is their lower cost, and the possibility to retrofit a large portfolio of bridges in a relatively short period of time.

This thesis investigates the use of linear elastomeric bearings in parallel with fluid viscous dampers for the retrofit of existing highway bridges. The stiffness of the elastic element is kept constant while varying the damping coefficient of the fluid viscous dampers. The performance of this retrofit strategy will be compared to other traditional isolation systems (e.g., FPS). The bridge used for this study is the Mississippi River Bridge located near Ottawa, Ontario. The bridge is 374 m long bridge with 6 spans, and five piers and two abutments supporting the bridge. The bridge has an existing hybrid (FPS+linear elastomeric) isolation system, which provides an excellent platform to compare the performance of various retrofit alternatives. Seismicity specific to this region of Ontario will be considered.

1.2 Objective and Scope

The main objectives of this thesis are the following:

- To demonstrate the effectiveness of bridge retrofits using a combination of linear elastomeric bearings and fluid viscous dampers
- To compare the performance of the proposed strategy with more sophisticated and versatile isolation systems such as FPS systems
- To evaluate the performance of the proposed retrofit method for long-span highway bridges in the Ontario region

The scope of this thesis will be limited to one long-span bridge in Ontario. Numerical studies will be conducted on models based on design drawings, and information gathered from soil reports at the time of design. Extrapolating the results of this study to general cases would require the analysis of a statistically meaningful set of short, medium and long span bridges, and is not attempted here. However, it is expected that the models developed here will provide a versatile computational test bed future studies on this subject.

Chapter 2
Background

2.1 Bridge Seismic Design

Many tend to think that bridges are rather simple structural systems, primarily because of their geometry. However, despite their simple shape and the relatively ease of design to serve its main purpose, the seismic design aspects have proven to be more challenging. Some of the older bridges that were designed to resist seismic loads were damaged by seismic events that were smaller than what was prescribed by the codes (Priestley & Seible, 1996). Priestley & Seible (1996) also suggested that those failures were mainly due to the elastic design concept followed at that time. In reinforced concrete structures, elastic design considers the gross section (un-cracked section) which under-estimated the overall displacement resulting from a seismic event. However, over the years, bridge seismic design and analysis has matured. Sophisticated seismic design and analysis methods taking into account the inelastic response of the bridge and the effect of soil-structure interaction have been developed and incorporated into bridge design.

While significant advances into the analysis procedures have been achieved over the years, there has been a simultaneous upward adjustment of the perceived seismic risk by the codes. This has translated to a substantial increase in the seismic loads expected to be carried by the bridge (Mitchell et al., 2010). Recent research has pointed to possible amplification of the free-field ground motions by the embankments. This problem is particularly serious for short-span highway bridges (N. Makris & Zhang, 2001). Consequently, a large inventory of older bridges (pre-1980s) needs retrofitting to improve their seismic performance and to bring them into code compliance.

2.2 Bridge Response

Evaluating the bridge response accurately is a critical step in achieving a good design. The seismic response evaluation of late 1980's freeway bridges and over crossings has been investigated thoroughly by several researchers. The seismic responses of several over-crossings were recorded under different earthquakes events, and validated using refined FE models (McCallen & Romstad, 1994; Meng & Lui, 2002; Zhang & Makris, 2002).

Highway bridges and overcrossings can be categorized by the primary structural materials used in their construction: reinforced concrete bridges, pre-stressed reinforced concrete bridges, and reinforced concrete deck on steel girders bridges. Each type has its preferred application and span limit. However, all these types can be modeled in a similar fashion. One of the early models for predicting the seismic responses is to use a stick model to represent the superstructure of a bridge (Maragakis & Jennings, 1987).

Stick models provide a numerically expedient means to evaluate bridge responses and to include the effects of soil-structure interaction. Full three-dimensional models, especially for the entire bridge, are expensive and in many cases un-necessary. The stick model has been extensively used to model medium and short span bridges. The stick model is usually used when the superstructure of the bridge is assumed to remain elastic throughout the seismic event. Many studies have tested the validity of stick models (McCallen & Romstad, 1994; Meng & Lui, 2002; Zhang & Makris, 2002).

McCallen and Romstad (1994) evaluated several dynamic response characteristics of the Meloland road over crossing. The evaluation was based on two different modelling approaches: idealized finite element model using a simplified stick model and a full scale three-dimensional finite element model. Frequencies, mode shapes and time histories were simulated for both the aforementioned models. McCallen and Romstad (1994) also modeled the soil behaviour at the end embankments using bilinear and simple nonlinear elements. The results from the two models agreed reasonably well; however, the results

deviated significantly in some modes due to the skewness of the overcrossing which is hard to capture using the stick model. The time history analysis of the stick model and the full model were compared to the recorded bridge response due to the 1979 Imperial Valley earthquake (M 6.4). The response predictions from both the models were in reasonable agreement with in situ measurements.

In another study, the validity of stick model was studied more rigorously (N. Makris & Zhang, 2001; Zhang & Makris, 2002). Two overcrossings, Meloland road overcrossing and Painter street overcrossing, were both modeled with a simplified stick model and a full-scale model. The first six modes were compared based on modal frequencies, modal damping ratios, modal shapes and time history responses. The comparison showed that the stick model is reliable when the bridge is not skewed. The issue of short skewed bridges was investigated in several other studies (Ghobarah & Tso, 1973; Meng & Lui, 2002; Yi Meng & Lui, 2000). Some of those studies provide refining methods to improve the predictions obtained from stick models. One study suggests the use of two stick models linked with skewed rigid links (Meng & Lui, 2002) as an option. They concluded that the effect of the bridge skewness is marginal for longer span bridges.

Zhang and Makris (2002) also compared the model results of the Meloland overcrossing with the results of the same bridge obtained by McCallen and Romstad (1994). The differences in the two studies are small; however, those differences could be explained by the different approaches used by the authors in calculating the soil-structure interaction. McCallen and Romstad (1994) discretized the soil in the embankments using finite elements; whereas, Zhang and Makris (2002) used an analytical approach to calculate the properties of the springs and viscous dampers that simulate the effects of embankments and piles. The latter is much simpler and yields reasonable results for most applications.

2.3 Soil-Structure Interaction

Soil-structure interaction, especially for short to medium span bridges, is one of the most difficult aspects to model and quantify. The overestimation of kinematic soil stiffness has led to many failures in bridges, e.g., due to pounding and other high unpredicted soil deformation (N. Makris & Zhang, 2001; Maragakis & Jennings, 1987).

Starting in the late 60's many researchers investigated the dynamic properties of soil deposits when subjected to dynamic loading (Hardin, 1965; Idriss, Seed, & Serff, 1974; Seed & Idriss, 1970; Seed & Idriss, 1969; Tatsuoka, Iwasaki, & Takagi, 1978). Many of these studies showed that the shear moduli and damping coefficient are highly variable with soil strain amplitudes among other factors, such as the number of loading cycles, during a seismic event.

Seed & Idriss (1970) studied the dynamic soil moduli and damping in sand deposits and saturated clays. Their report provided graphical relations between soil strain of sand deposits with shear moduli and damping. For example, a sample graph showing the relationship of shear modulus and damping with shear strain for sand deposits is presented in Figure 4.

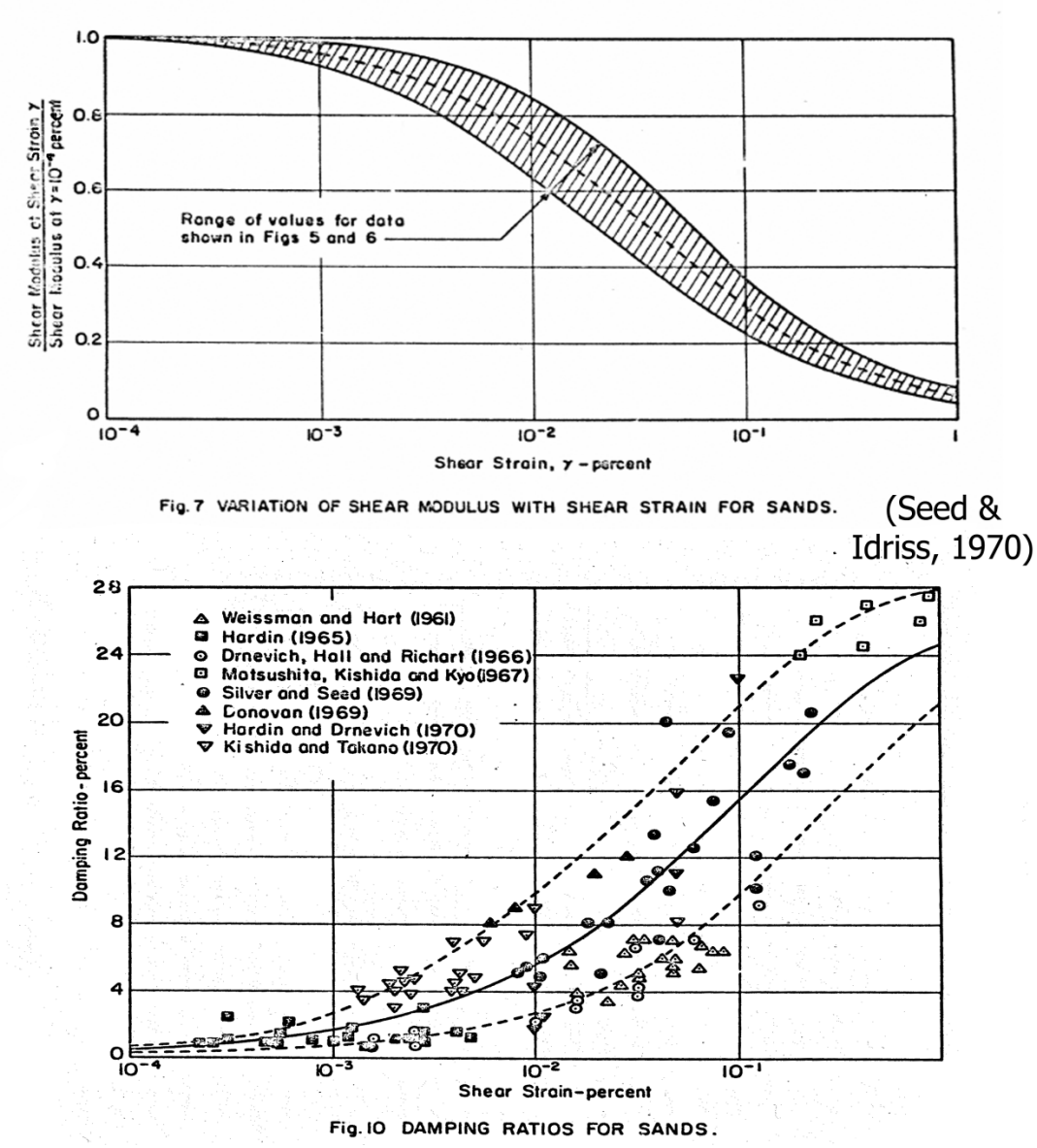

Figure 4. Soil dynamic shear moduli for sand and saturated clay relationships with soil strain (Seed & Idriss, 1970) .

Those results were then used by other researchers to measure the dynamic response of soil deposits and soil structures such as embankments and earth dams (Gazetas, 1987;

Idriss, et al., 1974). Idriss, et al. (1974) used the strain-shear moduli and strain-damping coefficient relationships to predict the response of soil deposits using the concept of variable damping finite element analysis. Gazetas (1987) studied the response of embankments and earth dams providing an analytical approach for analysing such soil structures under dynamic loadings. This analytical approach was used by other researchers for estimating the embankment kinematic response under seismic loads which, consequently, helps to simulate the embankment resilience by representing it with springs and viscous dampers (N. Makris & Zhang, 2000, 2001).

Analysing the soil-pile interaction was also of interest to many researchers (Nicos Makris, 1994; N. Makris & Gazetas, 1992) among others. N. Makris & Zhang (2001) provided a report with a detailed step by step description of the analytical approaches to analyse both the embankment and the piles soil-structure interaction. This report shows how to simulate the soil-structure interaction by implementing soil springs and viscous dampers. Furthermore, N. Makris & Zhang (2001) also provided a validation study to the analytical solution by comparing the responses of the analytical solution, a 3D finite element model, and the recorded responses. The two bridges considered in the validation analysis are the Meloland overcrossing and the Painter Street bridge which have an extensive database of recorded seismic responses.

In a recent study (Kotsoglou & Pantazopoulou, 2007), the embankment-structure interaction is studied analytically and numerically. Kotsoglou & Pantazopoulou (2007) calculated the kinematic response analytically using a rectangular 2D shear wedge, whereas the shear wedge has an equivalent height to the embankment and a wider crest; also, a 3D FE element model of the embankment is used to calculate kinematic response and compare to the analytical solution response. The results of the 2D rectangular shear wedge were consistent with the 3D model and field records. Kotsoglou & Pantazopoulou (2007) concluded that high deformations occur at the embankments during moderate or strong ground motions which lead to high unexpected displacements at the centre bent of

short bridges. Consequently, using multiple long flexible columns is more desirable to accommodate the deformation at the bent than high strength piers.

2.4 Bridge Retrofitting

Due to the increased seismic risk, inadequate initial designs and aging, the need to retrofit deficient bridges is now more urgent than ever. There are two main approaches to the retrofit of structurally deficient bridges: (i) Structural strengthening of the weak elements in the bridges, e.g., piers, or increasing the seat-widths, or (ii) energy dissipation and dynamic modification using control devices such as seismic isolation bearings on their own or in conjunction with fluid dampers to reduce the seismic loads in the structure.

2.4.1 Retrofit using structural strengthening

Strengthening of seismically vulnerable bridge elements is currently the most commonly used retrofit approach. One method is strengthening the columns of the bridge by providing confinement to the reinforced concrete columns such as: steel shells, reinforced concrete jacketing, and fibre reinforced polymer FRP jacketing. Those columns are commonly retrofitted due to a lack of sufficient ductility, shear strength, and lap splice clamping (Priestley & Seible, 1996; Walker & Karbhari, 2007). However, strengthening of bridge piers increases the stiffness of such piers which, in turn, attracts more loads. Moreover, the increased capacity to flexural loads and shear loads may not be sufficient if other elements such as foundations and pier caps were not considered in the retrofit design (Priestley & Seible, 1996).

Although, steel jacketing of columns has shown to perform well in past earthquakes (Priestley & Seible, 1996), this process can be very costly and needs substantial effort.

2.4.2 Retrofit using control devices

Primarily two control devices are extensively used in earlier studies of seismic isolation systemss: seismic isolation bearings and fluid viscous dampers. Most studies have used a combination of these devices for retrofit. Primarily, the control strategies have been used at the initial design stage, and only recently for the purposes of retrofit (Delis, Malla, Madani, & Thompson, 1996; N. Makris & Zhang, 2003, 2004).

2.4.3 Seismic Isolation Bearings

Seismic isolation systems can be very effective in retrofitting old bridges and in the design of new bridges. Examples of isolation bearings include the elastomeric bearings, lead-rubber bearings and friction pendulum bearings (see Figure 5). Isolation bearings work by lengthening the natural period of the bridge, thereby reducing the superstructure forces induced due to ground motions. Adding energy dissipation capability to the isolation system (using a lead plug or fluid dampers) adds to the performance of the isolation system.

Elastomeric rubber bearings are the most commonly used type of bearings. This type of bearings can be categorized based on the materials used in their construction; low-damping rubber elastomeric bearings, elastomeric bearings with a lead plug (LRBs) and high-damping rubber elastomeric bearings (Naeim & Kelly, 1999). Low-damping rubber elastomeric bearings use low damping natural or synthetic rubber pads reinforced with steel plates. The steel reinforcement increases the vertical stiffness of the bearing elements. The low-damping rubber pads are made of highly elastic material with very small damping during deformation. As a result, the elastomeric bearing attains a stiffness that is very close to linear stiffness. The advantage of such bearings is the ease of manufacturing and ease in modelling (Naeim & Kelly, 1999).

LRBs are similar to low damping elastomeric bearings, however, the bearing contain a lead plug inserted into the rubber pads to enhance their energy dissipation. The lead plug is constrained to deform by the rubber pads when the bearing is deformed. The lead plugs

yield at a certain point, which gives the elastomeric bearing a bilinear stiffness (Naeim & Kelly, 1999). The last type of elastomeric bearings, high-damping rubber elastomeric bearings, has a hysteric force-displacement response. The stiffness of the rubber pads reduces under high strain levels. This kind of behaviour helps dissipate the vibration energy and improves the seismic performance. However, this type of bearing is hard to model and simulate for analysis at the design stages (Aiken, 1997; Naeim & Kelly, 1999).

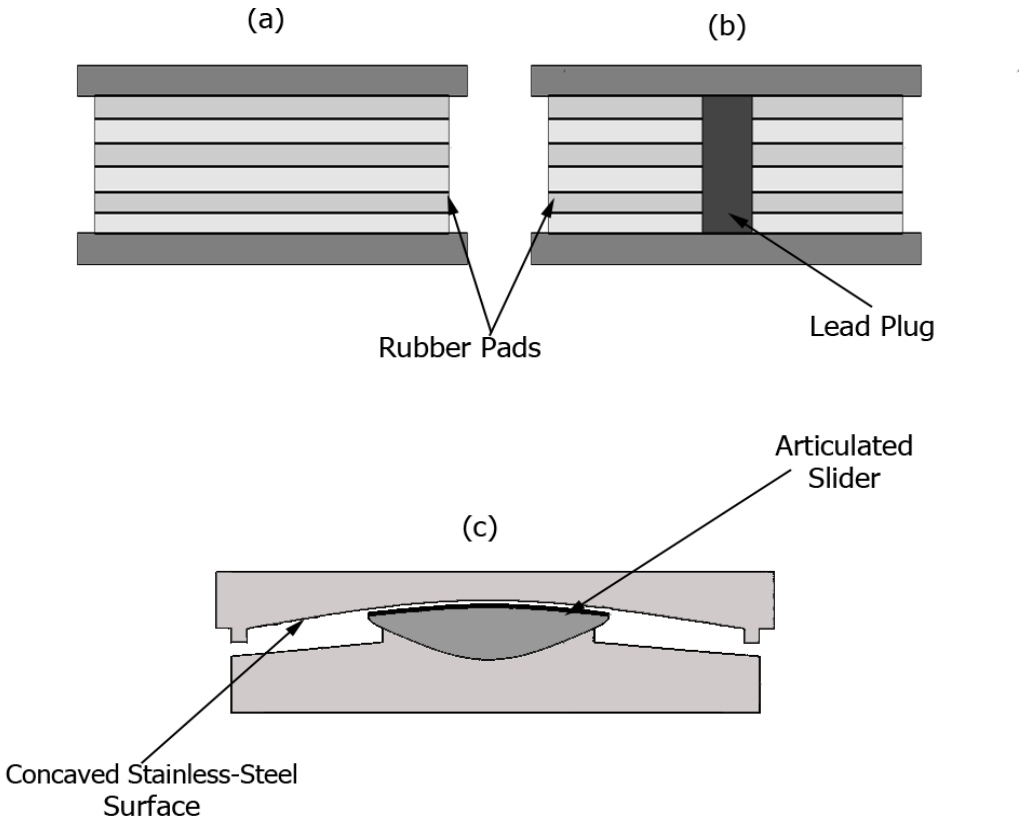

Figure 5. a) Low damping or high damping elastomeric bearing, b) Lead plug elastomeric bearing, c) Friction pendulum bearing.

Friction pendulum bearings primarily rely on the friction force between two contacting surfaces. The shear force developed in the bearing is mainly due to the friction between

the two sliding sides (Figure 5 (c)). Friction pendulum bearings are usually designed with a concave sliding surface which provides a re-centering balancing force, which also increases the apparent stiffness of the bearing at high deformations (Eröz & DesRoches, 2008). The behaviour of the friction pendulum bearings is strongly non-linear. Ideally, the non-linear behaviour of the friction pendulum can be described as a bilinear force-deformation response. However, literature shows that the assumption of a constant normal load on the bearing is not necessary accurate. In other words, the behaviour of the bearing can become much more complicated due to the varying vertical normal force on the bearing in real structures (Eröz & DesRoches, 2008).

2.4.4 Fluid Viscous dampers

Fluid dampers are essentially energy dissipative devices, similar in construction and functionality to shock absorbers in automobiles. They dissipate energy by transferring oil between two chambers via an orifice. In many applications, fluid viscous dampers are used in conjunction with an isolation system (see Figure 6). These viscous dampers provide additional damping to the structure, which helps in dissipating the vibration energy and in reducing the bearing deformations as well as the forces transferred to the substructure in some cases (Delis, et al., 1996; N. Makris & Chang, 2000).

Isolation bearings have the advantage that they improve the seismic performance of bridges; however, they can induce unexpected forces to the structure if they are not designed with caution. Such a scenario is the P-delta effect of the deformed bearings. The horizontal deformation of the isolation bearings shifts the vertical load application point, which creates de-stabilizing moments on both the substructure and the super structure. Another scenario is the pounding of the deck at the abutments and any adjacent structures resulting from excessive deformations at the bearings . The deformations allowed should be calculated accurately, and designed carefully, to avoid such a scenario. Many instances of pounding have been reported in the literature (Priestley & Seible, 1996).

Figure 6. Hwy 91/5 crossing in Orange County equipped with fluid viscous dampers. (Agrawal, Tan, Nagarajaiah, & Zhang, 2009)

Adding fluid viscous dampers to an isolation system limits these excessive displacements of the deck, thereby limiting the potential effects of isolator instability, unseating and pounding. Equipping bridges with isolation bearings and dissipation devices such as viscous dampers for improving the seismic performance have been recorded worldwide: The Vincent Thomas suspension bridge, California; The Rion Antirion cable-stayed bridge, Greece; the San Francisco-Oakland Bay Bridge; the Coronado Bridge near San Diego, California (N. Makris & Chang, 2000; N. Makris & Zhang, 2003).

Chapter 3
Modelling

Modelling is a key aspect in analyzing the response of highway bridges to seismic loading. In this regard, it is crucial to balance the complexity of the model with the computational overhead. Key sources of nonlinearities arise from the isolation system and sub-structure elements. Idealizations, especially for the nonlinear elements, are explained in the current chapter. As well, the idealization of the effects of embankments, piles and foundations are explained in detail.

The main test-bed considered for analysis is the Mississippi River bridge, located near Ottawa. This bridge is already outfitted with a hybrid isolation system, and the details of design using the response spectrum method has been reported in the literature (Murat Dicleli, 2002). This chapter is aimed at setting up a model for time-history analysis using OpenSees, an open source finite-element programming environment (McKenna, McGann, Arduino, & Harmon, 2010).

3.1 General Layout

Mississippi River Bridge is located 50 km west of Ottawa is a set of two independent bridges, east and west spans. Only one bridge, the west bridge is considered here. The bridge has a total length of 374 m, which is divided into six spans. The longest span is 85 m, which crosses over the river. The shortest spans are 40 m at the east end of the bridge and 54 m at the west end of the bridge. The remaining bridge spans are 65 m long each. The bridge has five piers and two abutments (See Figure 8).

Figure 7. Mississippi River Bridge. (MTO, 2010)

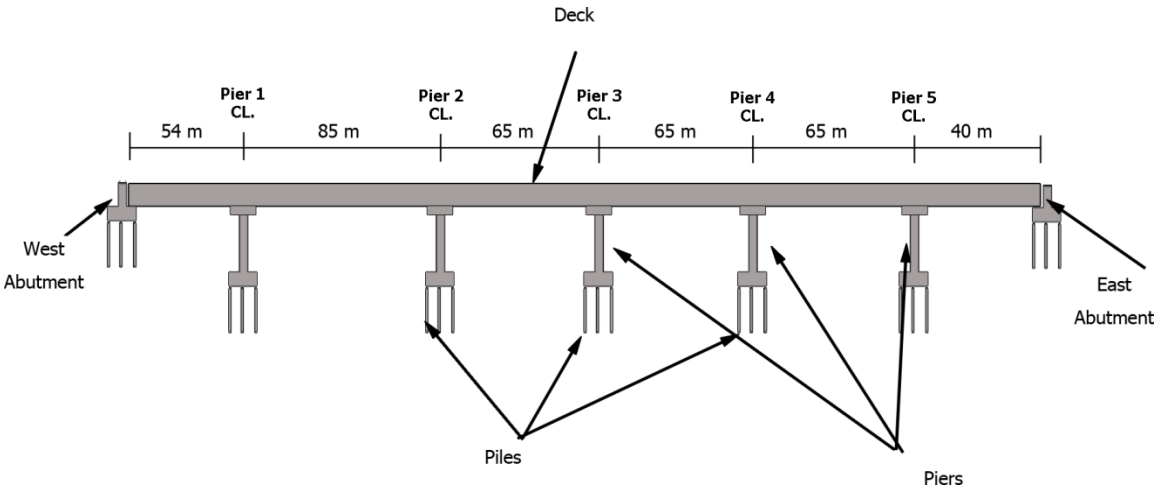

Figure 8. Mississippi River Bridge elevation.

The bridge deck is a reinforced concrete slab on steel girders. The deck is 225 mm thick reinforced concrete supported on four steel girders. The deck and girders of the bridge span continuously between the abutments, where the 120 mm expansion joints are located. The steel girder height ranges from 2.2 m at the abutments, piers 3, 4 and 5 and at the mid-spans, to a height of 4.2 m at piers 1 and 2 (See Figure 9).

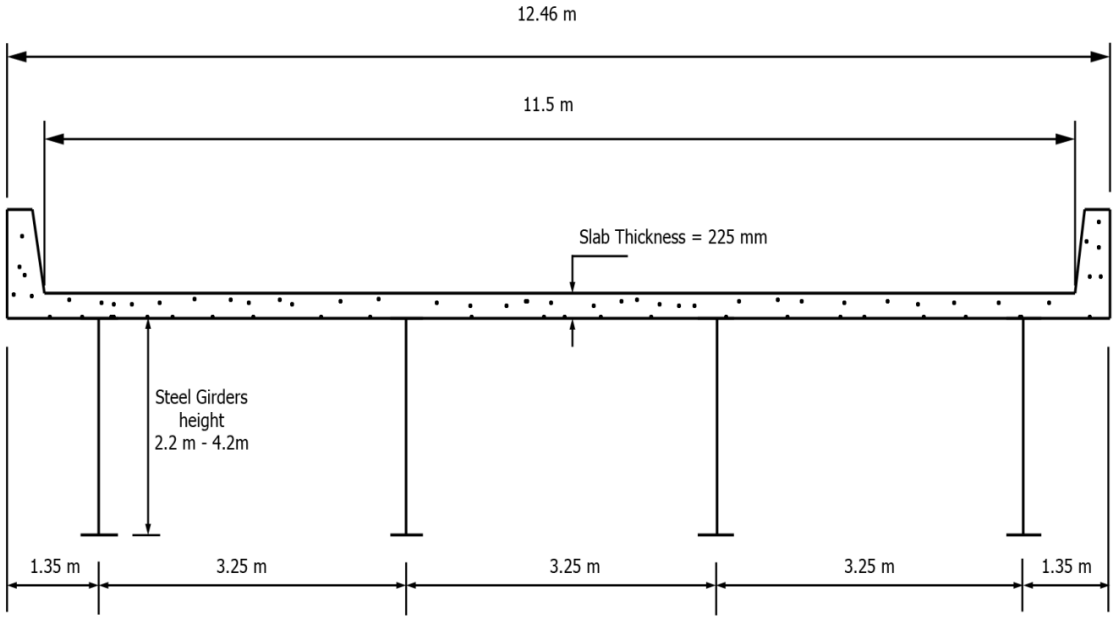

Figure 9. Mississippi River Bridge deck cross-section.

The bridge piers are reinforced concrete frames with two circular columns and a pier cap connecting the two columns and supporting the bearings. The columns heights range from 5.7 m to 7.8 m with a fixed radius of 1.8 m (see Figure 10).

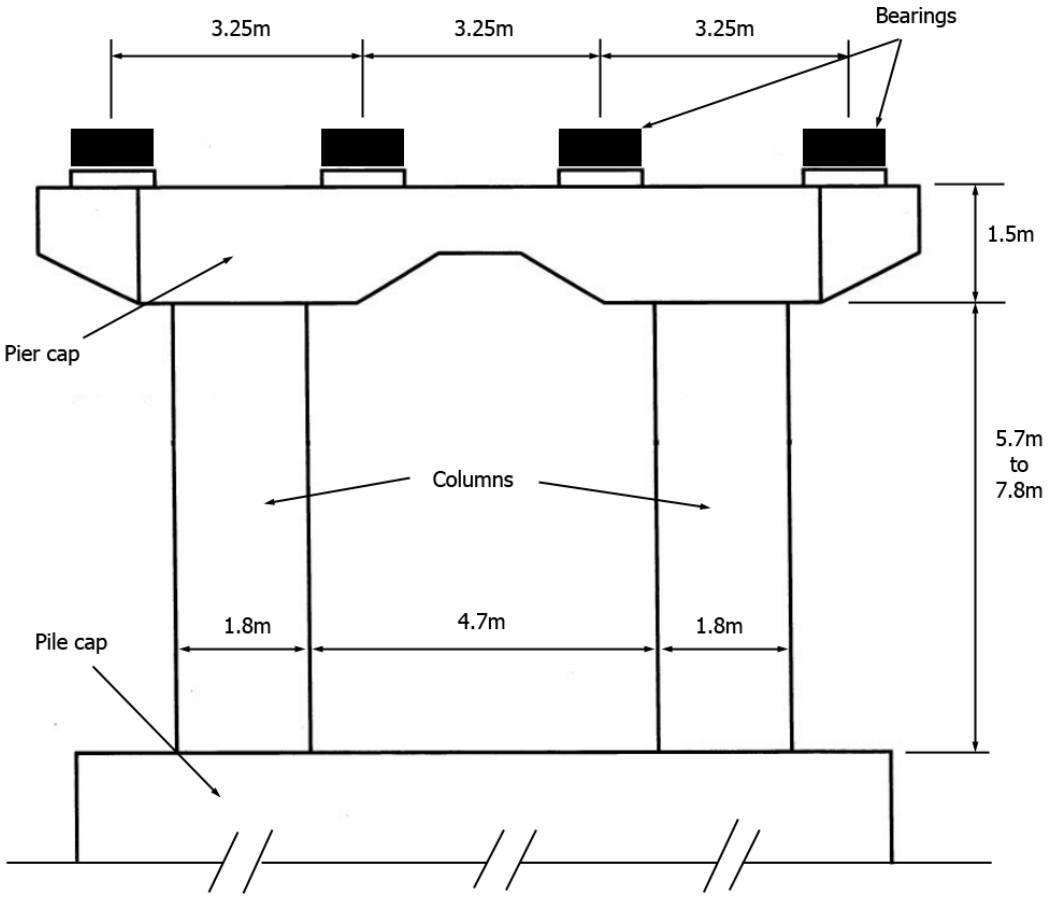

Figure 10. Mississippi River Bridge piers.

Both piers and abutments are supported by steel HP310×110 piles: 28 pile at the piers and 24 piles at the abutments. The lengths of the piles range from 41 m to 55 m and are connected at the top by a reinforced concrete pile cap, which supports the piers and abutments. The underlying soil is divided into three different soil layers. The upper layer is a dry silty clay soil with a varying depth around 4 m. The next layer is about 30 m deep and is made of stiff clay, while the third layer (24 m deep) before the limestone bed rock is made of a very stiff clay soil. The bridge is equipped with vibration isolation bearings between the superstructure and the substructure of the bridge. Single concaved friction pendulum bearings are used at the piers and elastomeric pads bearings at the abutments (Murat Dicleli, 2002).

3.2 Bridge Idealization

A 3D finite element model was built to simulate and represent the dynamic behaviour of the Mississippi River Bridge when subjected to seismic loading. The model is a mixture of linear and nonlinear elements, which also includes the effect of the soil-structure interaction at the pile foundations and the embankments. The general model was built based on model updates and calibrations from various researches (McCallen & Romstad, 1994; Murat Dicleli, 2002; Zhang & Makris, 2002). The bridge model used is similar to Murat Dicleli (2002) model of the same bridge. However, Murat Dicleli (2002) used the response spectra analysis to analyze the bridge which requires linearization of the structure to get the representative fundamental periods. The linearization included linearization of bearings, linear elements for the piers and did not include the effect of soil damping. Hence, it is expected that the aforementioned model would be conservative in predicting the responses.

3.2.1 Deck Idealization

It is generally accepted that the bridge superstructure remains elastic throughout a seismic event (McCallen & Romstad, 1994; Meng & Lui, 2002; Zhang & Makris, 2002). Hence, 3D elastic beam elements were used to model the bridge deck. This type of modelling is

commonly known as a Stick Model (see Figure 11.). The size of each segment (beam element) is 1 m long which results in a total of 374 elements for the deck. The deck mass was assumed to be 14,580 kg/m; the distributed mass was lumped at the nodes between the segments. The vertical location of the beam elements is located at the centre of gravity of the superstructure. The entire deck is assumed to be in full composite action under seismic loading. Accordingly, the moment of inertia of the beam elements about the vertical axis (y-axis) and the lateral axis (z-axis) are 59.50 m^4 and 3.55 m^4, respectively (Murat Dicleli, 2002). Rigid transverse in-plane elements were used to simulate the bridge superstructure at locations above piers and abutments. These in-plane rigid elements provide a better representation of the bridge dynamic interaction between the piers or abutments and the deck. The in-plane rigid elements contain four rigid vertical elements at the girder locations that are linked at the bottom to the bearing elements (see Figure 11).

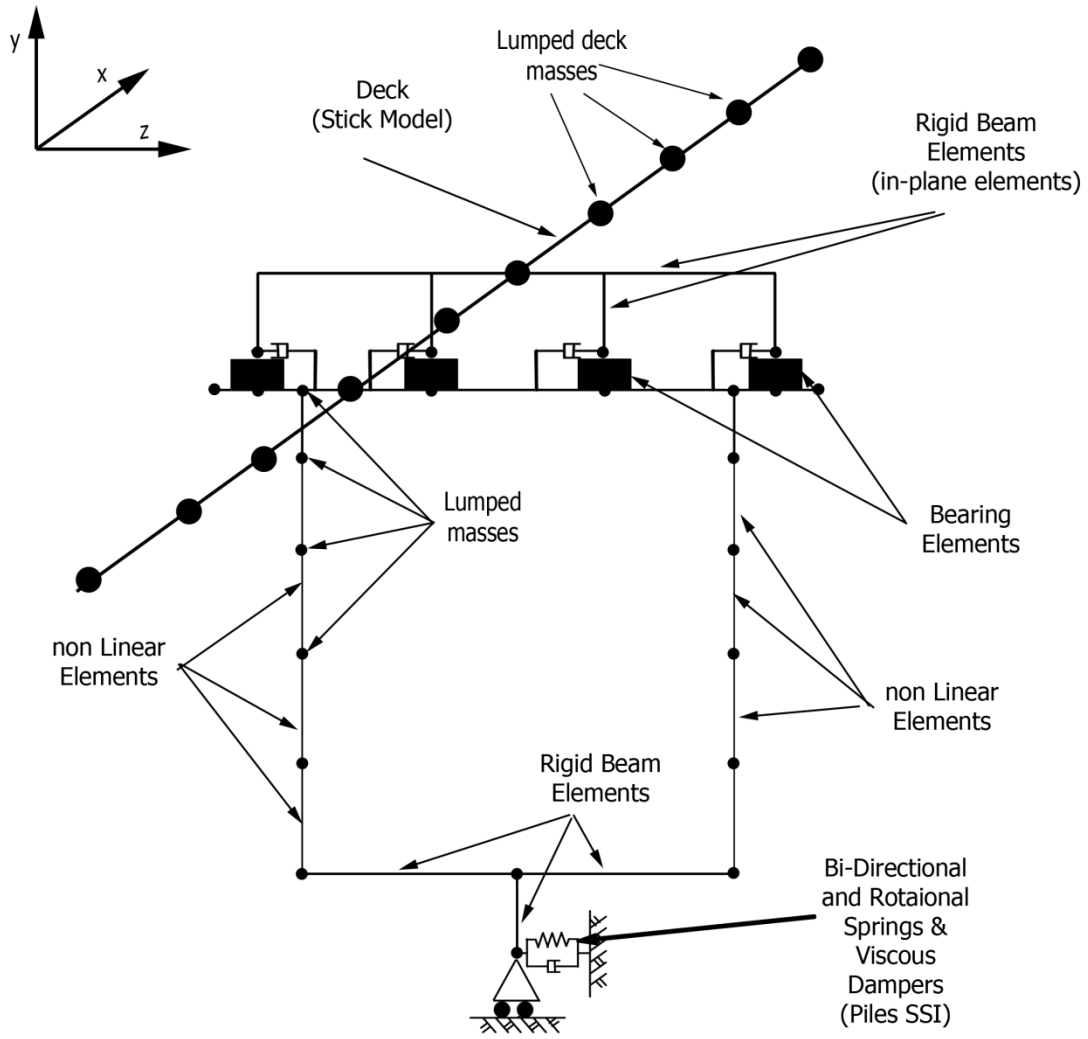

Figure 11. Mississippi River Bridge deck and pier models.

3.2.2 Pier Idealization

Non-linear 3D beam-column elements were used to model the piers. The pier cap has 8 nodes and 7 linear beam elements. The pier cap mass is lumped at the nodes. Four of the cap nodes are located under the aforementioned vertical rigid in-plane elements. The nodes of the pier cap and the deck rigid elements are connected together by the bearing elements (see Figure 11).

Bridges failures under seismic loads usually occur at the piers. Accordingly, the columns are modeled as non-linear elements. The non-linearity of the columns helps to capture any failure that may occur in the columns during an earthquake event. The columns are divided into 4 elements while each element has 7 integration points. The columns mass was lumped at the nodes connecting the segments. The section of the column elements was modeled as a fibre section. In other words, the section of the column is divided into a number of fibres (see Figure 12) where the fibres follow a predefined stress-strain curve when subjected to loading.

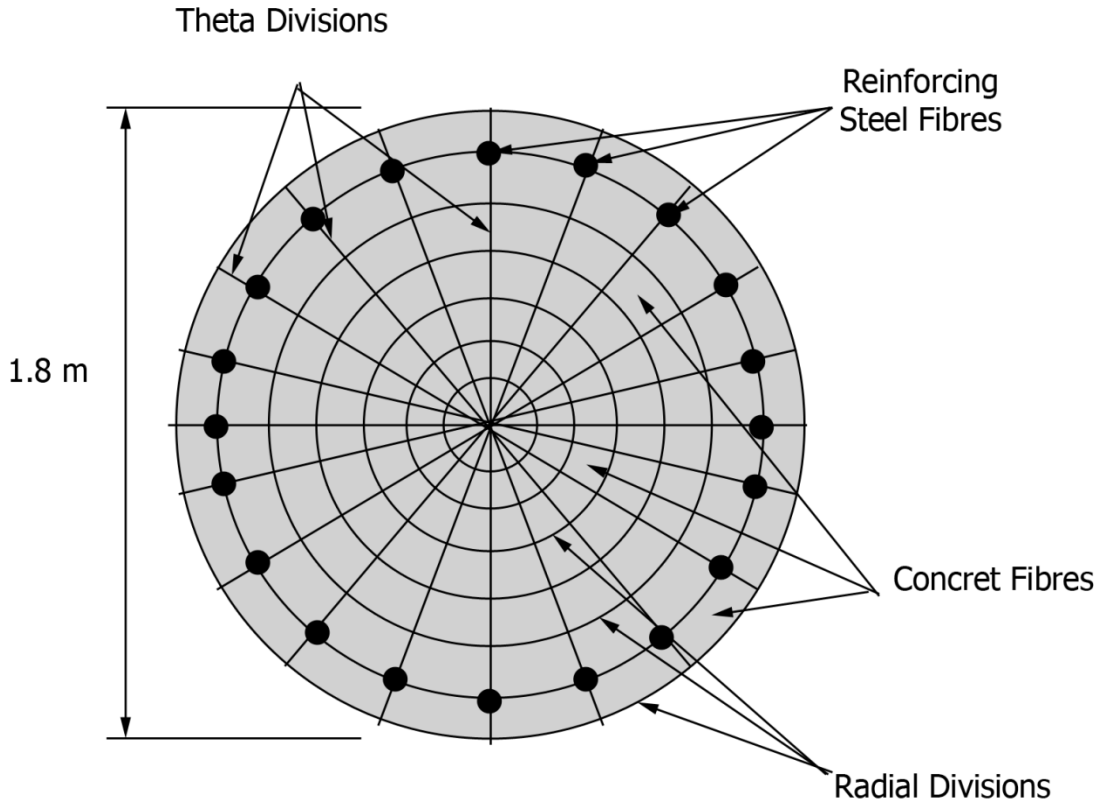

Figure 12. Columns fibre section.

The column elements were divided into 57 by 140 radial divisions (rings) and theta divisions (wedges), respectively. The pier columns consist of 32 steel bars, which were also included in the column section fibres with a predefined stress strain relationship. The stress-strain curves of the column concrete and the reinforcing steel were built-in OpenSees. The built-in materials Concrete02 and Steel02 were used for the concrete fibres and the steel fibres, respectively. Both of the materials are defined based on certain variables that OpenSees requires as inputs (see Figure 13). The actual steel and concrete properties of the columns were used to define the stress-strain curves of the materials in OpenSees. The concrete material variable $\grave{f}c$ is 35 MPa, E_0 is 26.6 GPa, ey is 2.6e-3, $\grave{f}cu$ is 7 MPa and ec is 11.3e-3, while the reinforcing steel material variable Fy is 400 MPa and Es is 200 GPa.

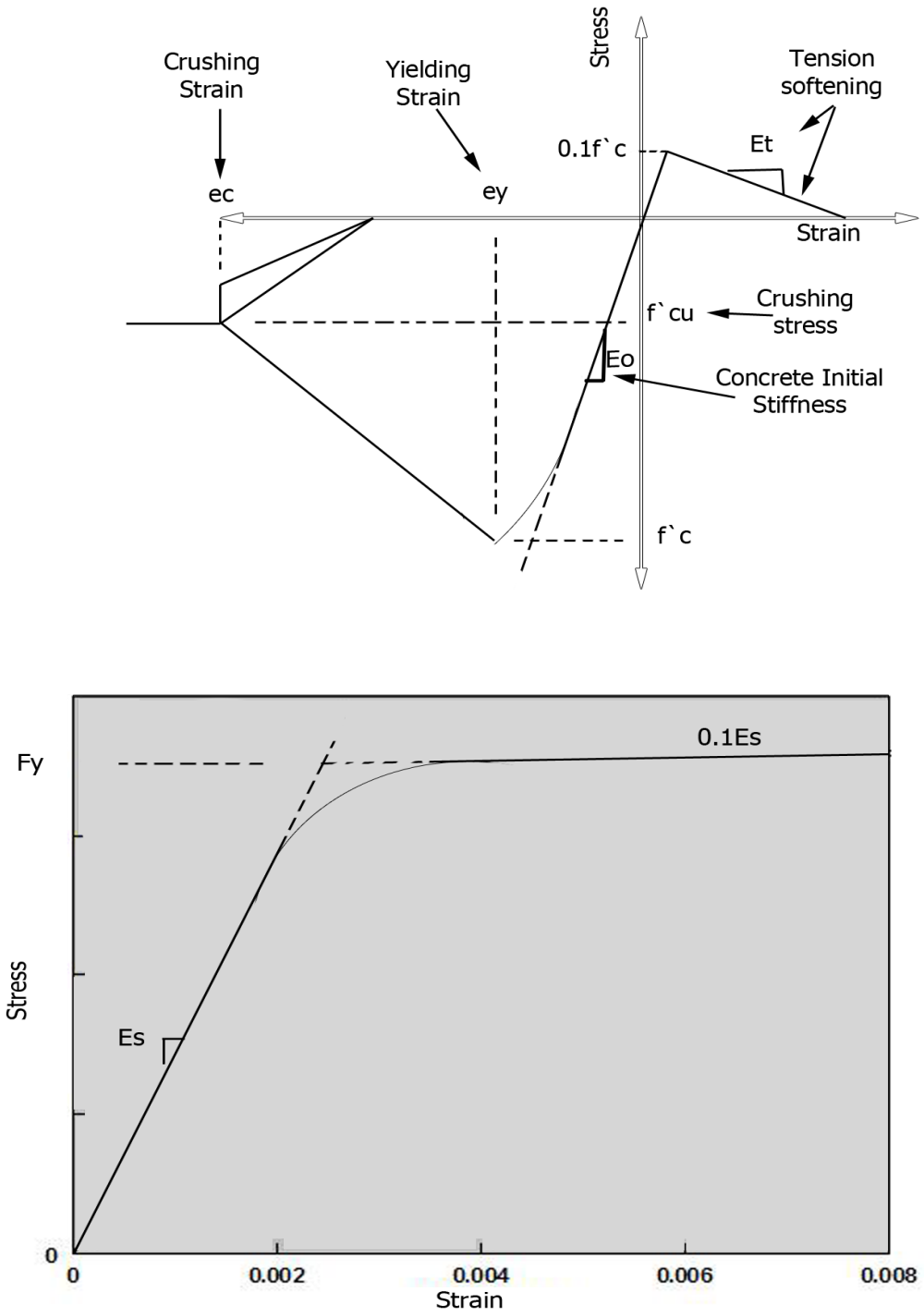

Figure 13. Concrete02 and Steel02 OpenSees materials stress-strain curves.

To simulate the pier footings (pile caps) two horizontal and one vertical rigid elements were used (see Figure 11). These elements were placed at the top of the piles to interface with the soil-structure interaction elements. The height of the pile cap vertical element was made equal to the footing depth.

3.3 Soil-Structure Interaction Idealization

Soil-structure interaction can have a significant effect on the dynamic response of the bridge. However, this effect is highly dependent on the bridge structure, the soil properties at the location and the seismic event. This section discusses the simulation of the soil-structure interaction and the procedure used to simulate the soil-structure interaction for both embankments and piles (see Figure 14).

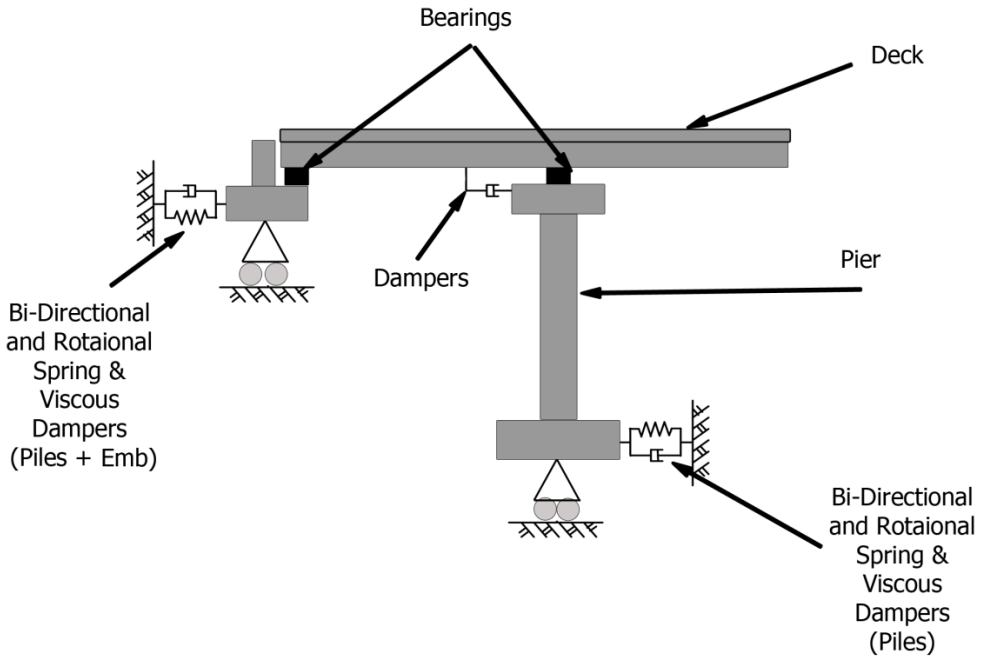

Figure 14. Schematic drawing of the soil-structure interaction idealization.

3.3.1 Embankment Idealization

There exist different methods with varying degree of complexity to simulate the soil-structure interaction at the embankments and piers. At its most advanced form, large 3D finite element models of the soil structure and the bridge structure are created. This requires significant numerical overhead for analysis, and may be suitable for cases where the effects of soil play a dominant role in the bridge response. Another popular method is to simplify the soil structure into parallel springs and viscous dampers to simulate the effect of soil-structure interaction. This method is simple, and has extensively been used for analyzing highway crossings, especially for medium to long-span bridges. The underlying principle in this method is the shear beam approximation for embankments. This method will only be briefly described in this thesis; the readers are referred elsewhere for an in-depth discussion (Gazetas, 1987; N. Makris & Zhang, 2000, 2001).

3.3.1.1 Kinematic Response

In the shear beam approximation the embankment is modeled as an infinitely long shear beam. The shear beam is assumed to have a trapezoidal shape representing the shape of the modeled embankment (see Figure 15).

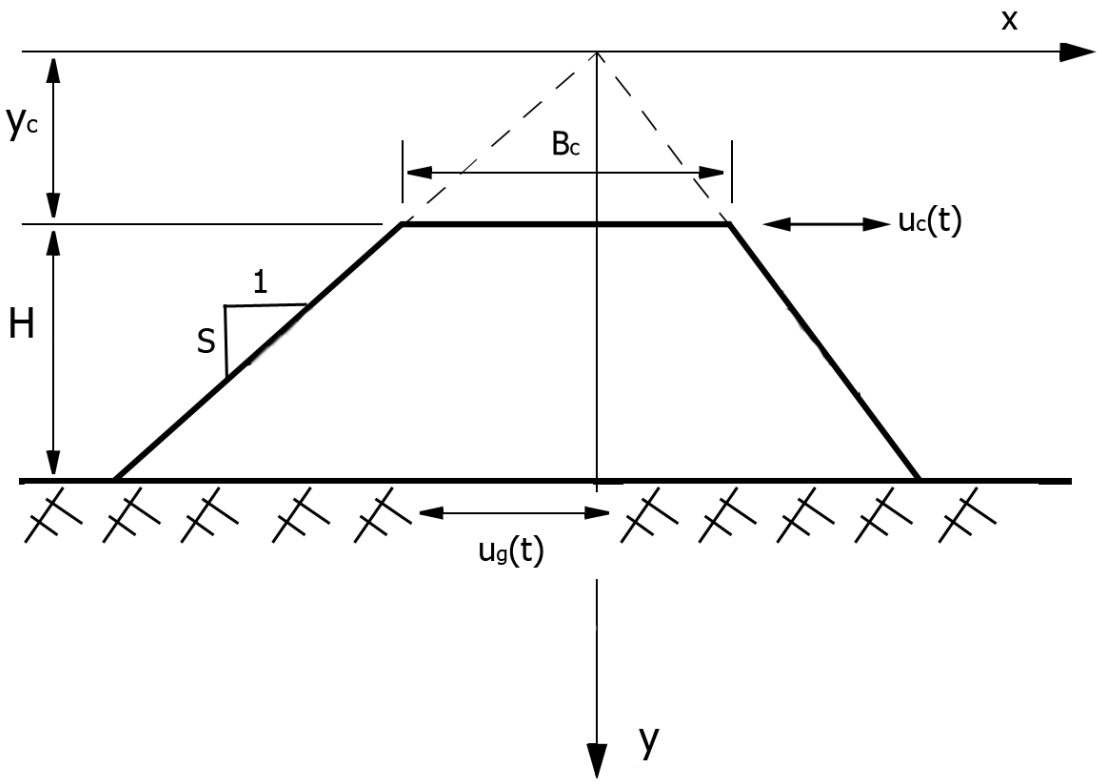

Figure 15. Schematic drawing of the embankment shear beam model.

Figure 15 shows the infinitely long shear beam cross section. This shear beam is subjected to a free field ground motion $\ddot{u}_{g(t)}$ from the bottom of the embankment. The embankment has a height of H and a crest width of B_c. The embankment crest is at y_c while the bottom of the embankment is at $(y_c + H)$ where y is the distance from the point where the extended lines of the embankment sides meet. The slope of the embankment sides is S, however, the shape can be non-symmetric where the two sides of the embankment can have different slopes. The deformation in the shear beam is only assumed to happen in the horizontal direction (along the X-axis); also the deformation of the shear beam is independent of the x location. Taking a unit length of the shear beam and assuming a plane strain condition, the resulted equation of motion is:

$$\rho_s \frac{\partial^2}{\partial t^2}\left[u_x(y,t)+u_g(t)\right]=\frac{1}{y}\frac{\partial}{\partial y}\left(G_s(y)\times y\times\frac{\partial}{\partial y}u_x(y,t)\right) \qquad 3.1)$$

where u_x and u_g are the embankment displacement and the ground displacement, While G_s and ρ_s are the soil shear modulus and the soil density of the embankment material. G_s is variable and proportional to the confining pressure, however, in this case G_s is assumed to be constant and independent of y.

The shear beam equation of motion has an analytical solution, which is given by (N. Makris & Zhang, 2001):

$$\left|R(\omega)\right|=\left|\frac{u_x(y_c,\omega)+u_g(\omega)}{u_g(\omega)}\right|=\left|\frac{b_1J_0(ky_c)+b_2Y_0(ky_c)}{u_g(\omega)}\right| \qquad 3.2)$$

This solution is in the frequency domain where the quantity in interest here is the kinematic response function $\left|R(\omega)\right|$ of the shear beam. $\left|R(\omega)\right|$ is the absolute value of the ratio between the embankment crest amplitude $\left[u_x(y_c,\omega)+u_g(\omega)\right]$ and the base displacement $u_g(\omega)$. $u_x(\omega)$ and $u_g(\omega)$ are the Fourier transformations of the embankment relative displacement and the ground displacement, respectively.

b_1 and b_2 are given by

$$b_1=\frac{u_g(\omega)}{J_0\left(k\left(y_c+H\right)\right)-\frac{J_1(ky_c)}{Y_1(ky_c)}Y_0\left(k\left(y_c+H\right)\right)} \qquad 3.3)$$

$$b_2 = b_1 \times -\frac{J_1(ky_c)}{Y_1(ky_c)} \qquad 3.4)$$

J_0 and Y_0 are the first and second kind zero-order Bessel functions while J_1 and Y_1 are the first and second kind first-order Bessel functions. $k = \omega / V_s$ where ω is the frequency and V_s is the embankment soil shear velocity.

In order to get the crest displacement the following expression is used

$$u_x(y_c, \omega) = \left[R(\omega) \times u_g(\omega)\right] - u_g(\omega) = u_g(\omega)\left[R(\omega) - 1\right] \qquad 3.5)$$

From the previous equations the effect of the embankment shape is represented in the values of y_c and H while the soil shear modulus and density are represented by V_s, where $V_s = \sqrt{G_s/\rho_s}$.

It was mentioned earlier that G_s is assumed to be constant. Hardin (1965) noted based on experimental studies, that the soil small-strain shear modulus is almost independent of the frequency; nevertheless, the value of G_s is highly dependent on the soil strain γ_s. Accordingly, the dynamic shear modulus is set to take the simple form of

$$G_s(\omega) = G\left(1 + i\eta \,\mathrm{sgn}(\omega)\right) \qquad 3.6)$$

Where G and η are the soil shear modulus and the soil damping coefficient and are independent of the frequency variable ω. The function $\mathrm{sgn}(\omega)$ only takes the negative or the positive sign of ω. However, in this analysis only positive values of ω were used. As mentioned earlier the values of η and G are dependent on the embankment soil strain which requires an iteration solution to find the correct values. Figure 16 shows the

variation of the soil damping coefficient η and the soil shear modulus G normalized to G_{max} with the soil strain γ_s. Those curves were averaged from a range of curves suggested by different researchers (Seed & Idriss, 1970; Tatsuoka, et al., 1978).

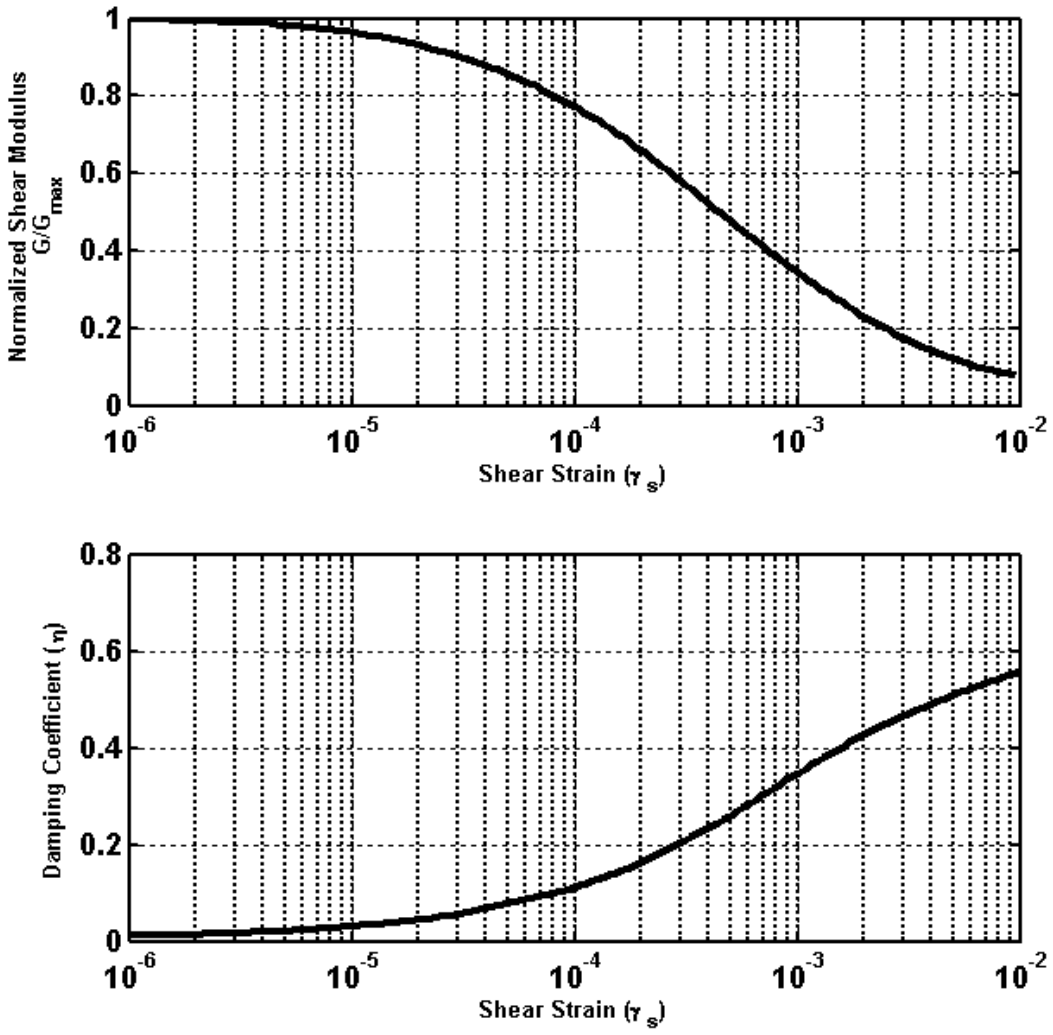

Figure 16. Soil damping coefficient and normalized shear modulus variation with shear strain.

In order to find the values of η and G an arbitrary strain value γ_s is first selected and used to get the values of η and G from Figure 16. Using η and G in Equation (3.6) and then substituting the value of $G_s(\omega)$ into equations (3.4) and (3.5), the crest relative displacement response in the frequency domain is calculated $u_x(y_c,\omega)$. The crest relative displacement in time domain $u_x(y_c,t)$ is then calculated by computing the inverse Fourier transformation of $u_x(y_c,\omega)$. The Fourier transformations and the inverse Fourier transformations are calculated using the built-in commands FFT and IFFT, respectively, in MATLAB. Using the crest response, the soil strain for the next iteration is calculated by assuming an average strain equals two thirds of the max crest displacement divided by the height of the embankment, H. The previous procedure is repeated until the soil strain converges.

Figure 17 shows the crest responses of the Mississippi River Bridge embankments under ten different ground motions (which are described in Chapter 4). This figure shows that values of η and G for the embankment soil can vary significantly depending on the seismic event. Strong ground shaking events result in higher soil strains in the embankments, which increases the damping and reduces the stiffness of the embankments.

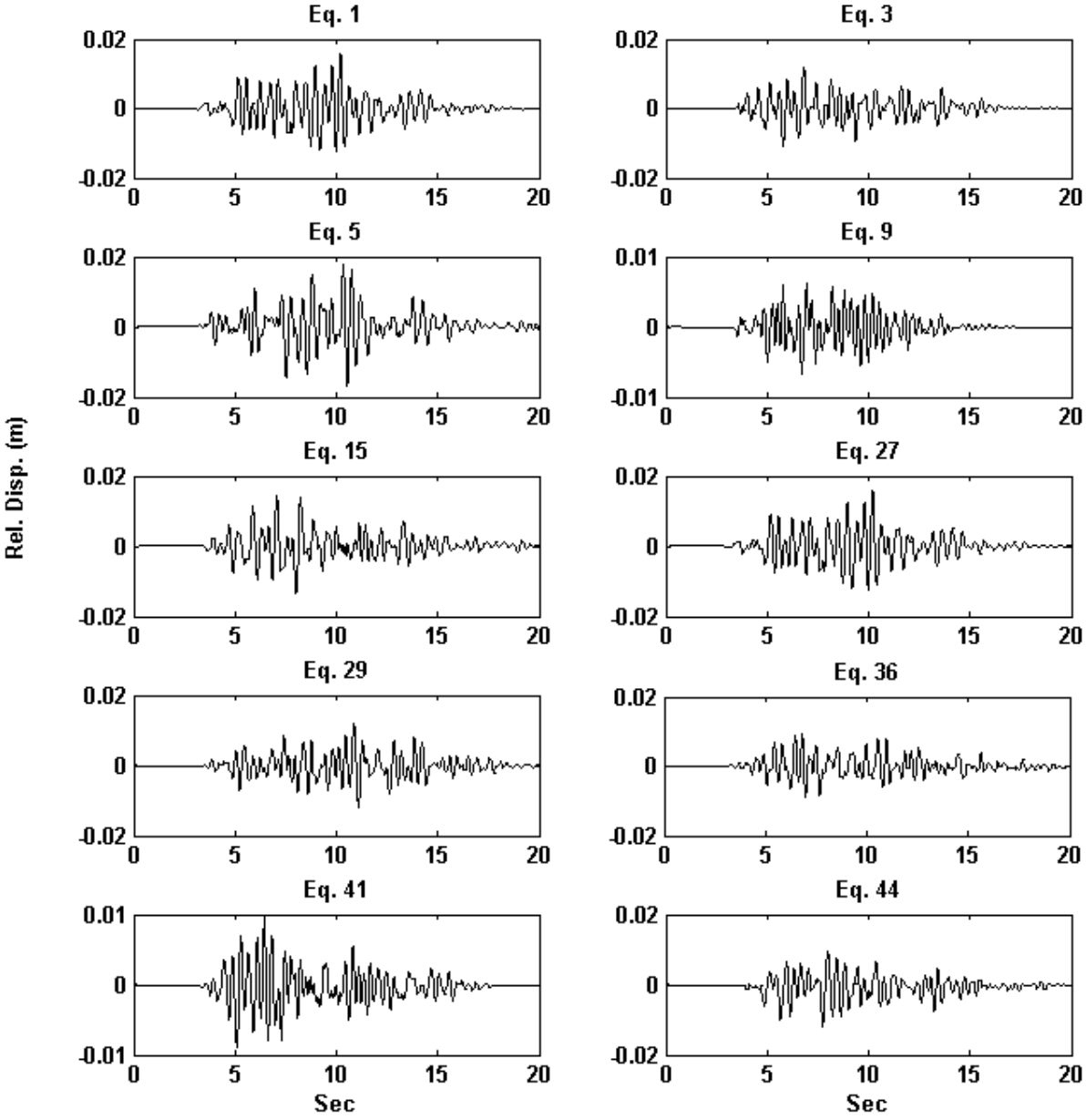

Figure 17. Relative crest displacements for selected earthquakes.

3.3.1.2 Embankment Resilience

After finding embankment crest response and the values of η and G , the resilience and damping of the embankments are calculated using

$$k(\omega) = G_s \times B_c \times k \times \frac{J_1(ky_c) \times Y_0(k(y_c + H)) - J_0(k(y_c + H)) \times Y_1(ky_c)}{Y_0(k(y_c + H)) \times J_0(ky_c) - J_0(k(y_c + H)) \times Y_0(ky_c)} \quad 3.7)$$

Instead of having different values of springs and dashpots for each earthquake, average values of η and G were assumed.

Where $k(\omega)$ is the dynamic stiffness of the embankment when subjected to a cyclic force $p_x e^{i\omega t}$ on one side of the embankment wedge (see Figure 18).

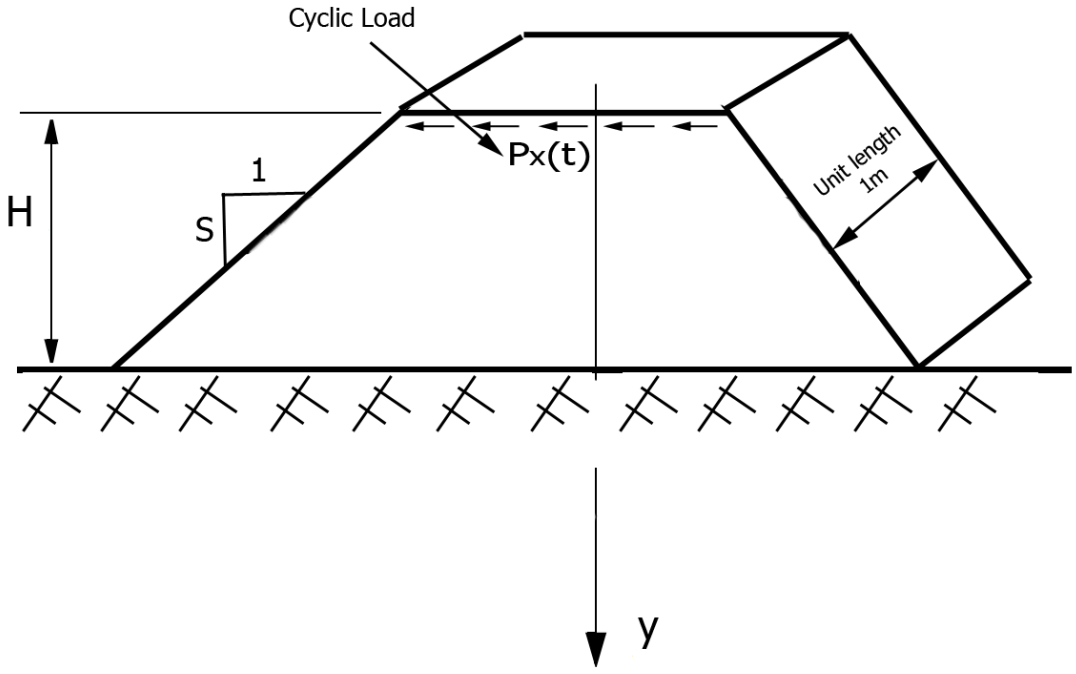

Figure 18. Embankment cross section subjected to a cyclic force at the tip.

To find the stiffness of a unit length of the embankment the real part of $k(\omega)$ is plotted with respect to the frequency. A horizontal line is drawn across the curve to represent the lower frequencies (see Figure 19).

To find the damping coefficient per unit length of the embankment, the imaginary part is plotted with respect to the frequency. An inclined line that passes through the origin is drawn to capture the curve at the lower frequencies as well (see Figure 19). The damping coefficient per unit length will be equal to the slope of this line.

After the stiffness per unit length and the damping coefficient per unit length of the embankment are measured, the values are multiplied by the critical length

$$L_c = 0.7\sqrt{B_c \times H \times S} \qquad 3.8)$$

Where L_c is the critical length of the embankment and it is a shape dependent variable. Increasing the embankment crest width, the embankment height or the embankment slope, will result in an increase in the critical length of the embankment.

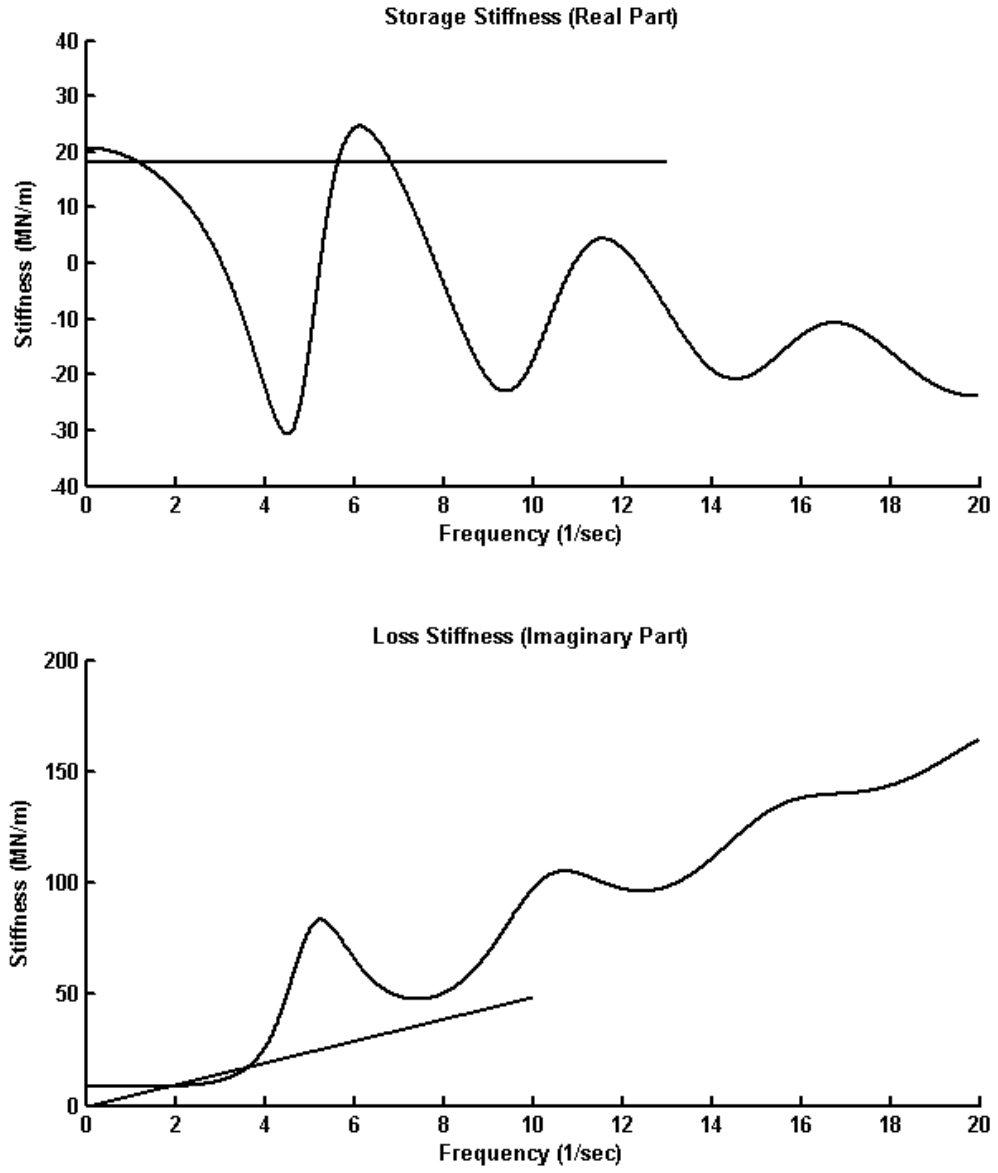

Figure 19. The real part (top) and the imaginary part (bottom) of the embankment dynamic stiffness. $\eta = 0.4, G = 0.27$, $H = 5.02m$ *and* $y_c = 3.115m$.

3.3.2 Pile Foundation Idealization

Seismic records show that the pile cap motion can be different from the free field motion when the excitation has high frequency components. On the other hand, in case the free field motion has only low frequency components the pile cap motion can be very close to the free field motion (N. Makris & Gazetas, 1992; N. Makris & Zhang, 2001).

Mississippi River Bridge has five piers and two abutments. Each pier and abutment is supported by 28 and 24 HP310x110 piles, respectively. The underlying soil is highly cohesive clay varying from stiff at the top 20m to 30m layer to very stiff at the below 20m layer. However, the piles are driven approximately 50 m in the soil stratum which is assumed to be homogeneous.

In order to simulate the soil structure interaction at the bridge piles an analytical approach was followed. This approach calculates the dynamic stiffness of a single pile in both lateral and vertical directions and then builds a stiffness matrix for the whole pile system. The stiffness matrix accounts for the geometry of the piles distribution, and also for the direction of the earthquake waves. Different dynamic stiffness matrices are constructed to account for both horizontal directions, vertical direction and for the three rotational directions. The pile cap is assumed to be rigid and the piles move as one unit at the pile cap. However, unlike the case for the embankment response, the analytical approach doesn't account for the effect of the seismic event on the dynamic stiffness of the piles. This analytical solution is only briefly described in this report. A more rigorous description and validation can be found elsewhere (Nicos Makris, 1994; N. Makris & Gazetas, 1992; N. Makris & Zhang, 2001).

3.3.2.1 Single Pile Dynamic Stiffness

To calculate the dynamic stiffness of a pile group, the stiffness of a single pile needs to be calculated. The single pile stiffness depends both on the pile shape and material as well as the surrounding soil. The single pile dynamic stiffness consists of two parts real part for storage stiffness and an imaginary part for loss stiffness (N. Makris & Zhang, 2001):

$$K_{x,s}(\omega) = \frac{E_p \times I_p \times R^3 \times \left(r_1^2 + r_2^2\right)}{r_1 - ir_2} \qquad 3.9)$$

where $K_{x,s}(\omega)$ is the dynamic stiffness of a single pile. E_p is the pile modulus of elasticity. I_p is the pile moment of inertia where in this case, due to the piles cross-section, the piles will have two different moment of inertias and both needs to be accounted for. The r_1 and r_2 values can be found from the following equations

$$r_1 = -a^3 - b^3 - 3a^2b + 3ab^2 \qquad 3.10)$$

$$r_2 = a^3 - b^3 + 3a^2b - 3ab^2 \qquad 3.11)$$

The values of R, a, b and θ can be calculated based on the following equations. However, the equations vary based on how the exciting frequency compares to the soil-pile characteristic frequency $\bar{\omega}_x = \sqrt{k_x(\omega)/m}$. $k_x(\omega)$ being the frequency dependent soil stiffness and m being the mass per unit length of the pile

$$R = \left[\frac{\left(k_x(\omega) - m \times \omega^2\right)^2 + \left(\omega \times c_x(\omega)\right)^2}{\left(4I_p \times E_p\right)^2}\right]^{1/8} \qquad \omega < \bar{\omega}_x$$

$$R = \left[\frac{\left(k_x(\omega) - m \times \omega^2\right)^2 + \left(\omega \times c_x(\omega)\right)^2}{\left(I_p \times E_p\right)^2}\right]^{1/8} \qquad \omega > \bar{\omega}_x \qquad 3.12)$$

$$a = \cos\left(\frac{\theta}{4}\right) + \sin\left(\frac{\theta}{4}\right), b = \cos\left(\frac{\theta}{4}\right) - \sin\left(\frac{\theta}{4}\right) \qquad \omega < \bar{\omega}_x$$

$$a = \cos\left(\frac{\theta}{4}\right), \qquad b = -\sin\left(\frac{\theta}{4}\right) \qquad \omega > \bar{\omega}_x \qquad 3.13)$$

$$\theta = \tan^{-1}\left[\frac{\omega \times c_x(\omega)}{\left(k_x(\omega) - m \times \omega^2\right)}\right] \qquad \omega < \overline{\omega}_x$$
$$\theta = \tan^{-1}\left[\frac{-\omega \times c_x(\omega)}{\left(m \times \omega^2 - k_x(\omega)\right)}\right] \qquad \omega > \overline{\omega}_x \qquad \textit{3.14)}$$

For simplicity, researchers suggest that $k_x(\omega)$ can be approximated by a constant and $c_x(\omega)$ can calculated from the following approximate expression (N. Makris & Gazetas, 1992; N. Makris & Zhang, 2001).

$$k_x \approx 1.2E_s$$
$$c_x(\omega) \approx 2d\,\rho_s V_s\left[1+\left(\frac{V_{La}}{V_s}\right)\right]a_0^{-1/4} + \eta\frac{k_x}{\omega} \qquad \textit{3.15)}$$

Where η is the soil damping coefficient and can be taken as 0.1(Nicos Makris, 1994; N. Makris & Gazetas, 1992; N. Makris & Zhang, 2001). E_s is the soil modulus of elasticity and ρ_s is the soil density. $a_0 = \omega \times d / V_s$ which is a dimensionless frequency of excitation, d is the diameter of the pile, and V_{La} is the wave velocity and called Lysmer's Analogue (N. Makris & Zhang, 2001).

$$V_{La} = \frac{3.4}{\pi(1-\nu)}V_s \qquad \textit{3.16)}$$

Figure 20 shows the plot of the real and the imaginary parts of equation (3.9) with respect to a_0. The plots are normalized to the pile static stiffness. The figure also shows that the excitation frequency only has a marginal effect on the dynamic stiffness of a single pile.

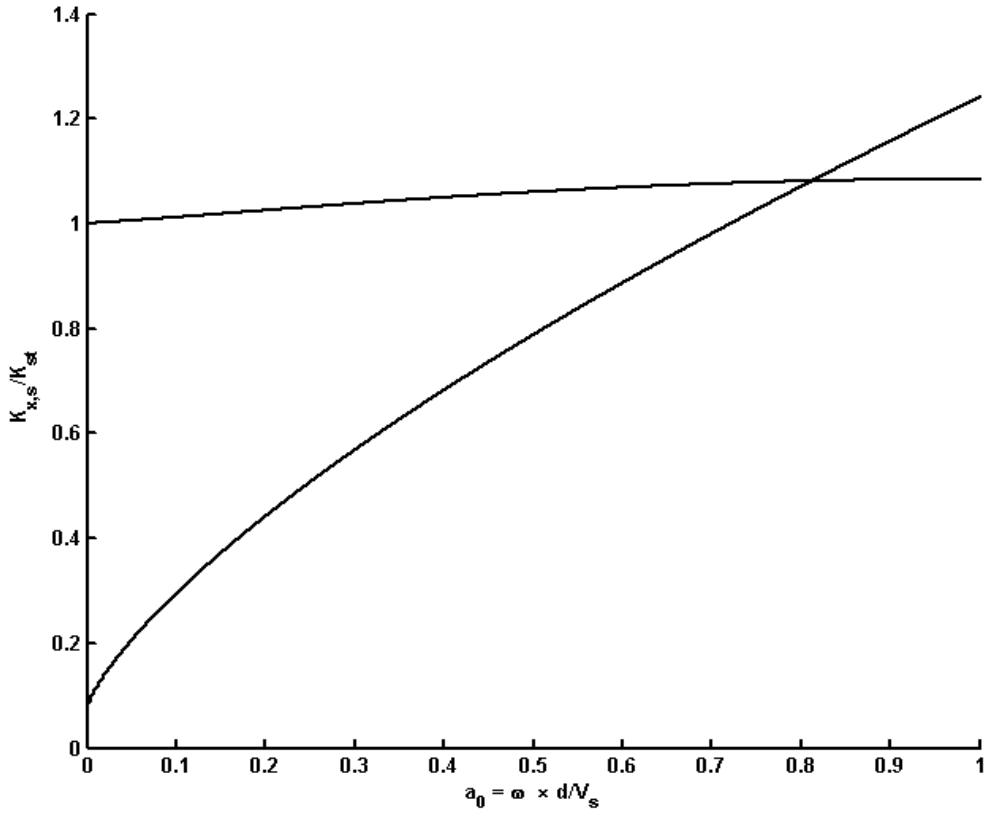

Figure 20. Normalized single pile dynamic stiffness for both parts real and imaginary in the horizontal direction.

To find the vertical dynamic stiffness of a single pile, the following expressions are used (N. Makris & Zhang, 2001):

$$K_{y,s} = \frac{R \times E_p \times A_p}{\cos\left(\frac{\theta}{2}\right) - i \sin\left(\frac{\theta}{2}\right)} \qquad \omega < \bar{\omega}_y$$

$$K_{y,s} = \frac{-R \times E_p \times A_p}{i \cos\left(\frac{\theta}{2}\right) + \sin\left(\frac{\theta}{2}\right)} \qquad \omega > \bar{\omega}_y \qquad \textit{3.17)}$$

Where A_p is the pile cross sectional area, $\bar{\omega}_z = \sqrt{k_y(\omega)/m}$ is the vertical soil-pile characteristic frequency, R and θ can be found using the following formulas.

$$R = \left[\frac{\left(k_y(\omega) - m \times \omega^2\right)^2 + \left(\omega \times c_y(\omega)\right)^2}{\left(A_p \times E_p\right)^2} \right]^{1/4} \quad 3.18)$$

$$\theta = \tan^{-1}\left[\frac{\omega \times c_y(\omega)}{\left(k_y(\omega) - m \times \omega^2\right)} \right] \quad 3.19)$$

3.3.2.2 Pile Group Dynamic Stiffness

In a pile group, the piles are relatively close to each other. This results in a dynamic interaction between the piles, once excited. This interaction results in a loss in the overall stiffness of the pile group. To find the lateral stiffness of a pile group the following equation is used (Nicos Makris, 1994; N. Makris & Gazetas, 1992; N. Makris & Zhang, 2001).

$$K_{x,G} = K_{x,s} \sum_{i=1}^{N} \sum_{j=1}^{N} \varepsilon_x(i,j) \quad 3.20)$$

Where $K_{x,G}$ is the pile group lateral stiffness,

$$\varepsilon_x(i,j) = \alpha_x(i,j)^{-1} \quad 3.21)$$

Where $\alpha_x(i,j)$ is an interaction matrix that describes how the piles interact based on the excitation frequency, the geometric distribution of the piles, the soil properties, and the direction of interest.

$$\alpha_x(i,j)=\begin{bmatrix} 1 & \alpha_x(1,2) & \alpha_x(1,3) & .. & \alpha_x(1,N) \\ \alpha_x(2,1) & 1 & \alpha_x(2,3) & .. & \alpha_x(2,N) \\ \alpha_x(3,1) & \alpha_x(3,2) & 1 & .. & \alpha_x(3,N) \\ : & : & : & & : \\ \alpha_x(N,1) & \alpha_x(N,2) & \alpha_x(N,3) & .. & \alpha_x(N,N)=1 \end{bmatrix} \quad 3.22)$$

Each of $\alpha_x(i,j)$ elements describes the interaction factor between two piles, and N is the total number of piles. The elements of $\alpha_x(i,j)$ can be found using

$$\alpha_x(S,\theta)=\alpha_x(S,0)\times\cos^2(\theta)+\alpha_x\left(S,\frac{\pi}{2}\right)\times\sin^2(\theta) \quad 3.23)$$

$$\alpha_x(S,0)=\frac{3}{4}\varphi(S,0)\frac{k_x(\omega)+i\omega c_x(\omega)}{k_x(\omega)+i\omega c_x(\omega)-m\omega^2} \quad 3.24)$$

$$\alpha_x\left(S,\frac{\pi}{2}\right)=\frac{3}{4}\varphi\left(S,\frac{\pi}{2}\right)\frac{k_x(\omega)+i\omega c_x(\omega)}{k_x(\omega)+i\omega c_x(\omega)-m\omega^2} \quad 3.25)$$

where S is the distance between the two piles in interest, and θ is the angle between the line joining the two piles and the direction in interest (loading direction) (see Figure 21).

$$\varphi(S,0)=\left(\frac{d}{2S}\right)^{1/2}\exp\left[-\left(\frac{\eta}{2}+i1\right)\frac{\omega\left(S-\frac{d}{2}\right)}{V_{La}}\right] \quad 3.26)$$

$$\varphi\left(S,\frac{\pi}{2}\right)=\left(\frac{d}{2S}\right)^{1/2}\exp\left[-\left(\frac{\eta}{2}+i1\right)\frac{\omega\left(S-\frac{d}{2}\right)}{V_s}\right] \qquad 3.27)$$

To get the vertical stiffness and the rotational stiffness of the pile group the same procedure is followed.

$$K_{y,G}=K_{y,s}\sum_{i=1}^{N}\sum_{j=1}^{N}\varepsilon_y\left(i,j\right) \qquad 3.28)$$

$$\alpha_y=\left(\frac{d}{2S}\right)^{1/2}\exp\left[-\left(\beta_s+i\right)\frac{\omega\left(S-\frac{d}{2}\right)}{V_s}\right] \qquad 3.29)$$

where $K_{y,G}$ is the pile group vertical dynamic stiffness, and ε_y is the inverse of α_y.

For the rotational dynamic stiffness the same vertical interactive factors matrix is used.

$$K_{r,G}=K_{y,s}\sum_{i=1}^{N}x_i\sum_{j=1}^{N}x_j\times\varepsilon_y\left(i,j\right) \qquad 3.30)$$

where $K_{r,G}$ is the rotational stiffness of the pile group, x_i and x_j are the distances of pile i and j from the rotational axes (see Figure 21).

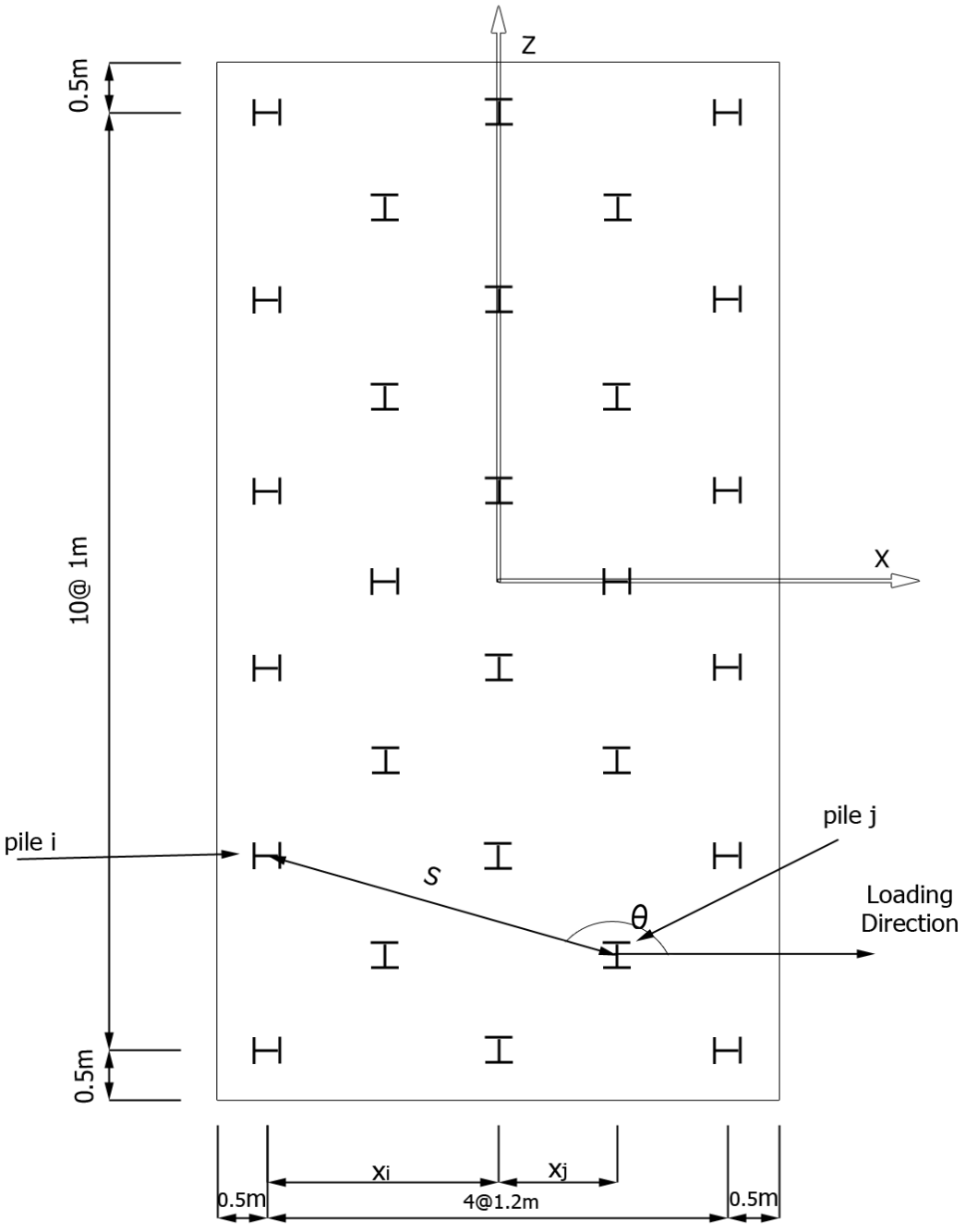

Figure 21. Schematic drawing of piers footing piles describing the angle of loading Θ , the distance between piles S , and the distances x_i and x_j .

Figure 22 and Figure 23 show the stiffnesses of the Mississippi River Bridge abutments piles and piers piles for different degrees of freedom. The first two plots in the figure titled "*Horizontal lateral (z)"* show both the real part and the imaginary part of the pile group lateral stiffness. The y-axis is normalized to the lateral static stiffness of a single pile multiplied by the number of piles in the group. The stiffness of the representing spring can be measured from the plots by passing a horizontal line through the curve in the lower frequency region. To get the lateral damping coefficient, the slope of a line passing through the origin of the plot is taken (see Figure 22). This damping coefficient will have the units of (*N×sec/m)* and is used to define the representing damping element.

The second and third sets of plots in Figure 22 and Figure 23 are the storage stiffnesses and loss stiffnesses for the longitudinal direction and the vertical direction, respectively. The vertical y-axes are normalized to N times the static stiffness of a single pile. The same procedure previously mentioned is used to get the stiffness and the damping coefficients for any desired degree of freedom.

The rotational stiffness about the x-axis and the z-axis are plotted on the next two sets of plots in Figure 22 and Figure 23. However, in those plots the y-axes shows the stiffness of the pile group divided by the group static stiffness.

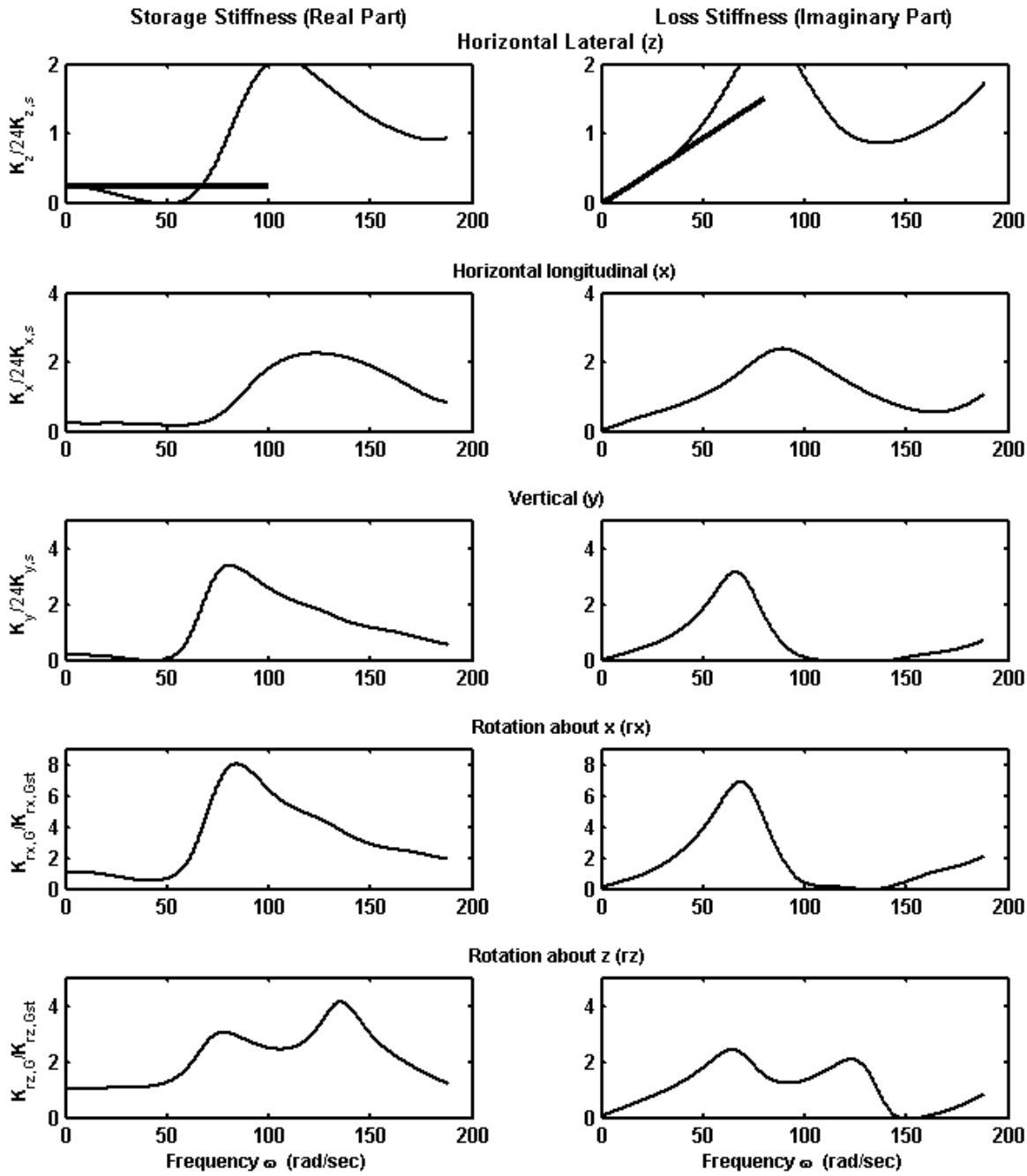

Figure 22.Abutments piles stiffness and damping.

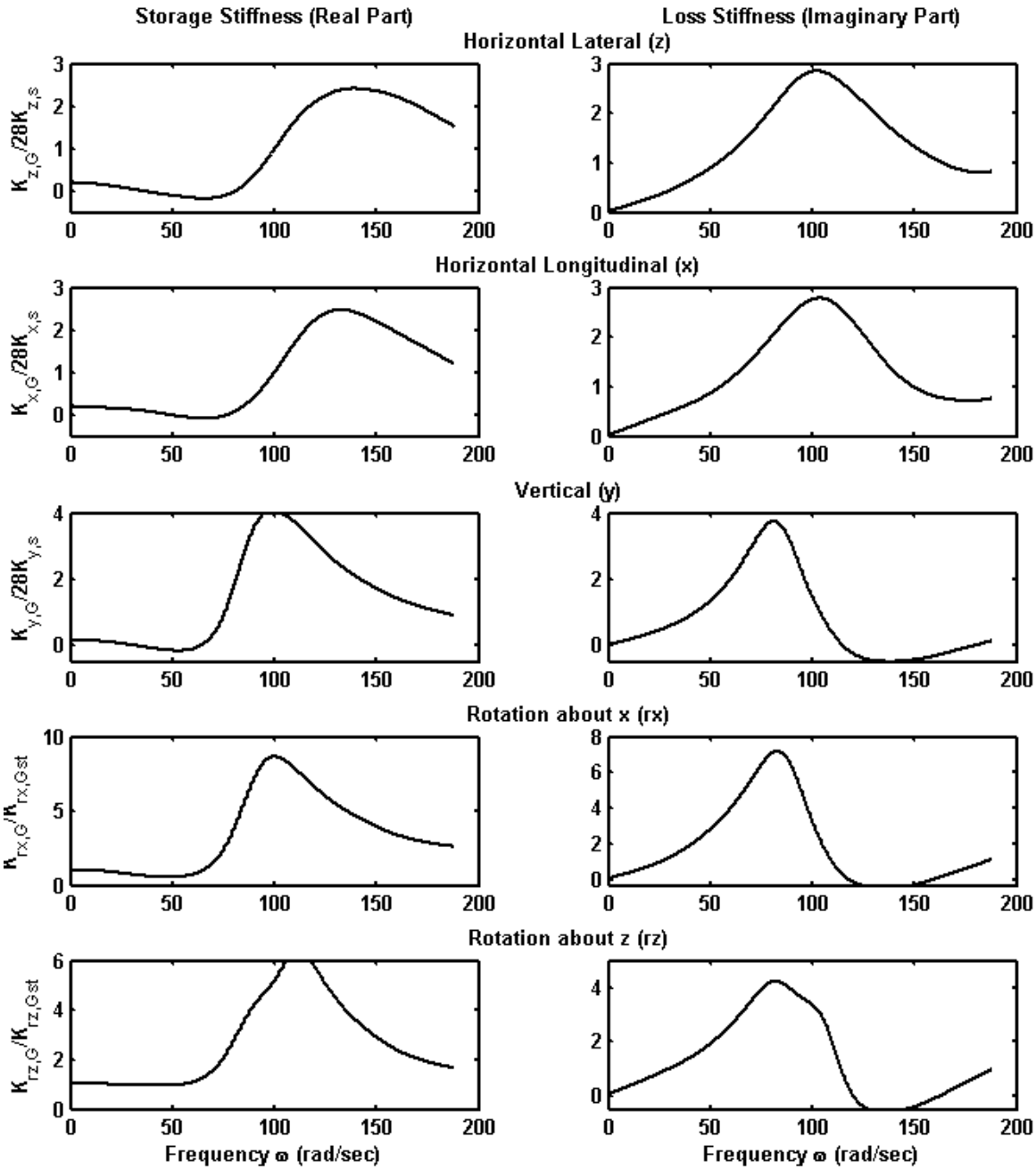

Figure 23. Piers piles stiffness and damping.

Table 1. Piles Soil-Structure Interactions.

Degree of Freedom	Piers		Abutments	
	Stiffness (MN/m)	Damping (MN*sec/m)	Stiffness (MN/m)	Damping (MN*sec/m)
Translational (Z)	173.64 (118.76)	13.526383	176.07+17.72*	14.08+4.90*
Translational (X)	131.18 (111.96)	10.218656	133.02+17.72*	10.64+4.90*
Translational (Y)	fixed	fixed	fixed	Fixed
	Stiffness (MN.m/rad)	Damping (MN.m.sec /rad)	Stiffness (MN.m/rad)	Damping (MN.m.sec /rad)
Rotational (rz)	6492.71 (5688.16)	224	5295.20	190.4
Rotational (rx)	16786.30 (19445.0)	672	22865.4	1008

Note:

* The embankment stiffness and damping are added to the abutments pile stiffness.

The numbers in brackets are the those calculated by (Murat Dicleli, 2002).

Table 1 shows the piles and the embankments springs and dashpots coefficients. The table shows both the rotational and the translational stiffness. Also the spring values used by Murat Dicleli (2002) for the piers are shown. Murat Dicleli (2002) constructed to separate orthogonal frames simulating the pile and piles cap. The piles were attached to springs with simulating the soil stiffness. By calculating the pile cap stiffnesses in different directions the SSI springs are obtained. The discrepancies in the stiffnesses

could be due to the soil modulus estimation, and the dynamic interaction between the piles. The embankments stiffness and damping was added to the abutment piles stiffness and damping. The results in the table show that the rotational stiffness of the pile caps about the x-axis is more than two times larger than the rotational stiffness about the z-axis. In other words, the geometry of the piles distribution (pile cap) can have a significant role on the rotational stiffness. However, this factor is not of a significant effect for the translational stiffness.

3.4 Bearings

Bearings are used to isolate the bridge superstructure from the substructure. The Mississippi River Bridge in its current condition has Friction Pendulum bearings (FP) at all the piers and Linear Elastomeric bearings (LE) at the abutments. Each pier and abutment supports four bearings located under the girders of the superstructure (see Figure 11).

Both bearing types are modeled using the open source software OpenSEES. OpenSEES provides built-in bearing elements that simulate the FP bearings and LE bearings. The properties and models for the bearings are described in the following.

3.4.1 Friction Pendulum Bearings

The FP bearing has two sides, the lower side is an articulated slider and the upper side is a concaved sliding surface. The FP bearing elements are mainly friction dependent elements; in other words, the lateral force it exerts is proportional to the normal force applied to the element and the friction coefficient. Nevertheless, the concaved FP bearings exerts another component of lateral force which is proportional to bearing displacement (Eröz & DesRoches, 2008; Murat Dicleli, 2002).

$$F = \mu N \ \mathrm{sgn}\left(\delta\right) + \frac{N}{R} D \qquad 3.31)$$

Where F is the bearing lateral force, μ is the friction coefficient, N is the normal force applied to the bearing, R is the concaved surface radius, D is the bearing displacement and $\mathrm{sgn}(\delta)$ is a signum function that accounts for the direction of movement.

The force displacement hysteric curve of the friction pendulum bearing is shown in Figure 24.

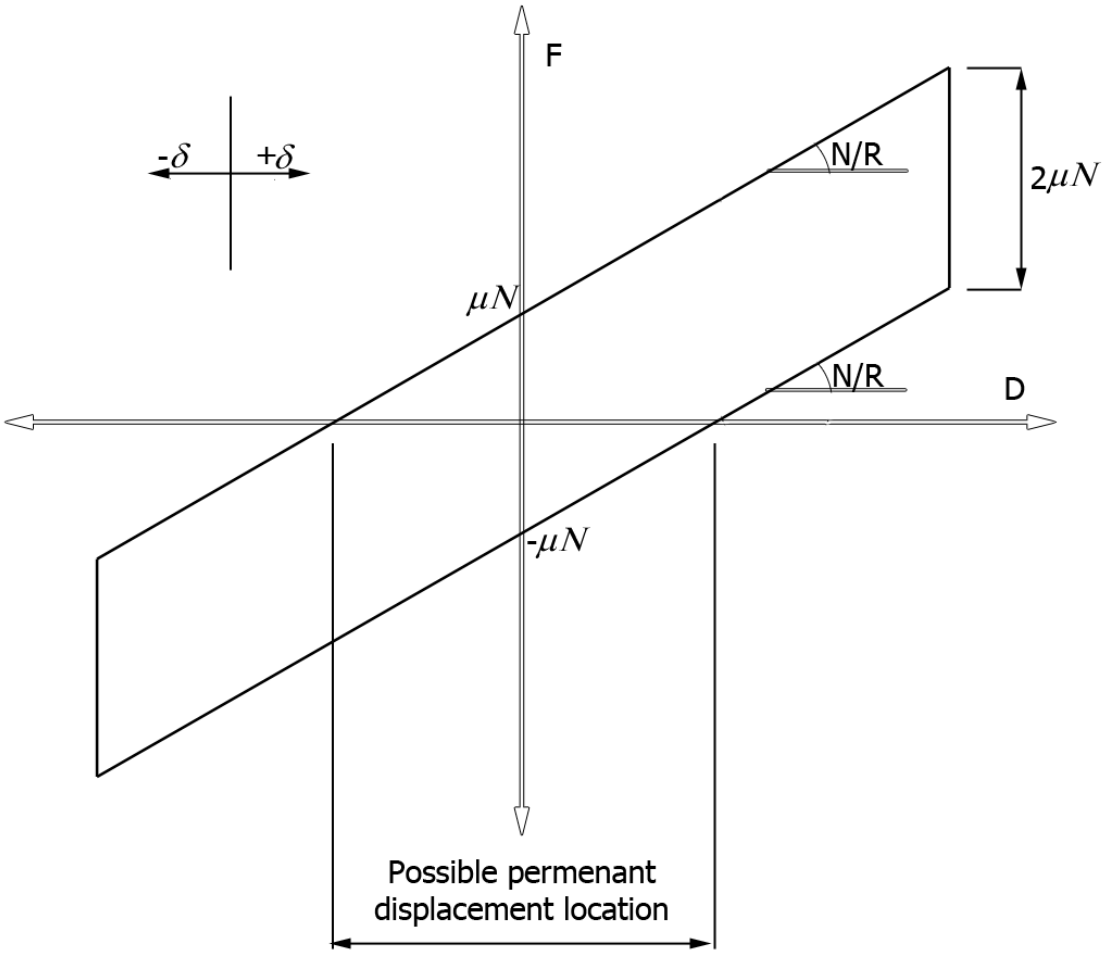

Figure 24. Force displacement hysteric loop of a friction pendulum bearing.

This hysteric loop can only be realized if the normal force N is constant during the seismic event. However, the normal force is not constant in real structures, and can be highly variable depending on the event and the structure shape. Eröz & DesRoches (2008) show that the normal force can reach a maximum of 3.5 times the static normal force in some cases and a minimum of zero in other cases. The hysteric loop also shows that the friction pendulum bearing can have a maximum permanent displacement of $D = \mu R$ when the bearing is displaced during a seismic event.

OpenSEES also considers other factors in defining the single concaved FP bearing element; the height of the articulated slider and the yield displacement. The height of the articulated slider effects the moments caused due to the bearing displacement; the yield displacement is the displacement needed for the bearing to reach the yield force μN when at rest.

The friction pendulum bearings used for the bridge has a friction coefficient μ of 0.07, a concaved surface with a radius R of 2.235m and a maximum deformation $D_{\max}$ of 178mm (see Figure 25).

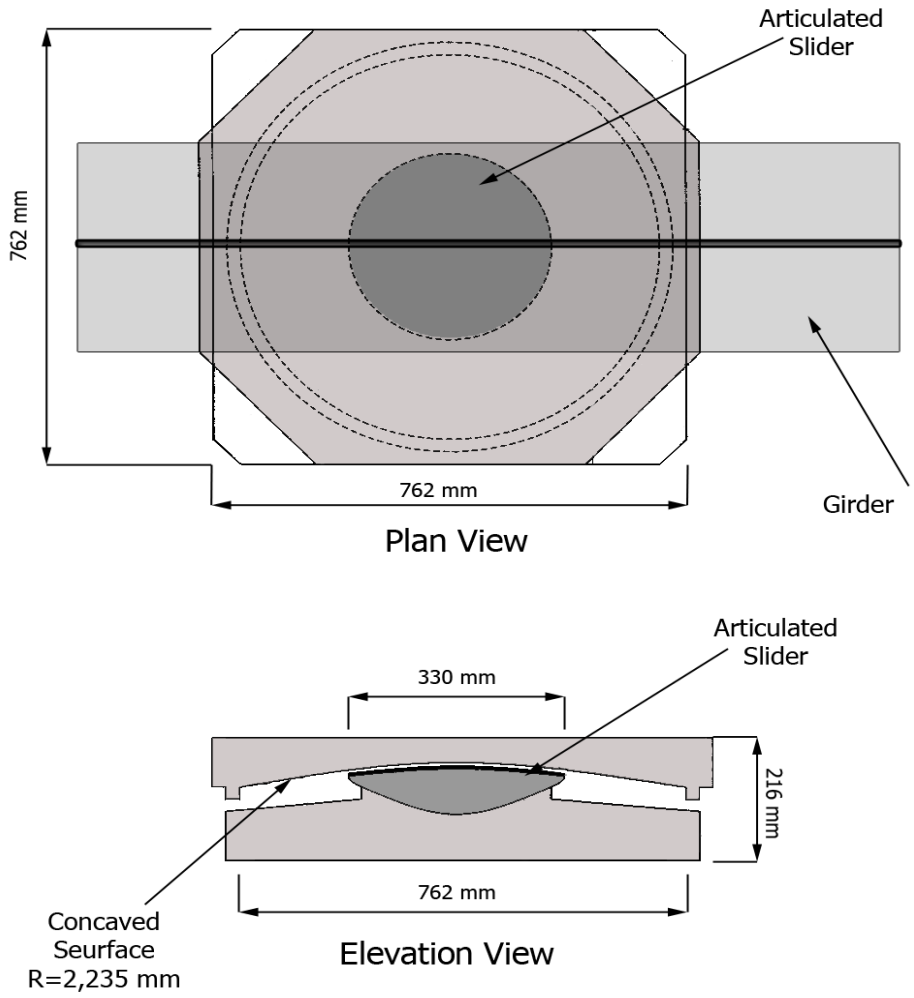

Figure 25. Mississippi River Bridge FP Bearing.

3.4.2 Linear Elastomeric Bearings

Elastomeric bearings are a very commonly used type of bearings. The stiffness of the bearing is defined by the following equation

$$K_{LE} = \frac{GA}{H} \qquad 3.32)$$

where K_{LE} is the LE bearing stiffness, G is the shear modulus of elasticity of the bearing material, A is the cross-sectional area of the bearing and H is the bearing height. Elastomeric bearings have a yielding force, however, herein the elastomeric bearings

were assumed to be linear. OpenSees LE bearing element also accounts for the moments resulting from the bearing deformation either in the x-direction or the z-direction.

The LE bearings used for the Mississippi River Bridge have a shear modulus G of 1.06 MPa, a square plan section of 785 mm by 785 mm and a height of 285 mm (see Figure 26). Accordingly, the stiffness of the LE bearings K_{LE} is 2292 KN/m.

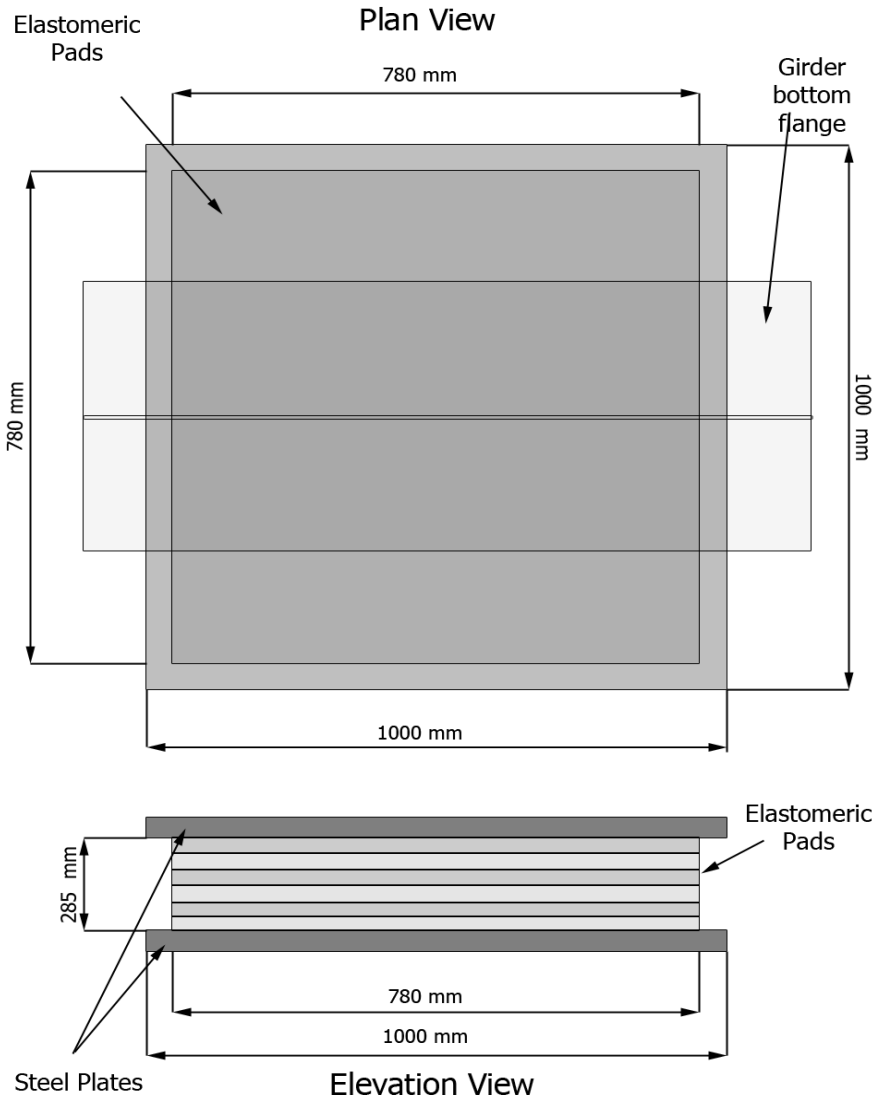

Figure 26. Mississippi River Bridge elastomeric bearings.

Chapter 4
Analysis Procedures

After describing the models for various bridge components used for simulations, the numerical simulation procedures are described. The seismic loads used to analyze the bridge will be described first, followed by a description of various bridge models used for comparison, and the performance variables used to evaluate the results from various retrofit strategies.

4.1 Seismic Loads

Seismic events can vary significantly between geographic locations. Some areas are seismically active, while others are not. Both the intensity and the characteristics of a seismic event can vary between different locations. Hence, choosing the appropriate seismic event for analysis is of paramount importance for the validity of the analysis results.

Seismic records from previous events can be useful for a seismic analysis; however, such historic records are not always available (for regions with low or medium seismicity) and do not necessarily meet the design provisions required by the design codes. To overcome such difficulties, researchers have employed stochastic simulation models to generate synthetic accelerograms (Atkinson, 2009). Such accelerograms are compatible with the design spectra applicable to a particular site, and hence satisfy code criteria. These seismic events (accelerograms) are calibrated based on historic seismic records that have previously occurred at the same geographical zones of interest.

Atkinson (2009) has provided different seismic events that are compatible with different site locations and different site classes, throughout regions of Canada. The selection of the appropriate seismic event from a database is undertaken through a matching process between the design response spectra (RS) of the bridge and the seismic events RS.

The seismic events are selected by measuring the standard deviation of the ratio between the bridge RS and the seismic event RS (RS_B / RS_E) for the return periods range in interest. In other words, only a specific range of return periods is used to compare the RS's. This range of return periods is selected to encompass the fundamental periods of interest for the bridge structure, in this case 1 to 3 seconds. The events with lower standard deviations are selected, however, the mean of the ratio should not exceed 2 or be lower than 0.5 (Atkinson, 2009).

The RS of the Mississippi river bridge was calculated from the Canadian Highway Bridge Design Code (CHBDC) (CAN/CSA, S6-06). The Mississippi River Bridge is located in the outskirts of Ottawa city, which falls in a zone with a peak ground acceleration of 0.16g, g being the acceleration due to gravity. The bridge was considered an emergency route bridge with an importance factor of 1.5. Bridge site soil profile is very stiff clay which falls under the (CHBDC) (CAN/CSA, S6-06) soil profile type II. Figure 27 shows the Mississippi River Bridge response spectra in accordance to (CHBDC) (CAN/CSA, S6-06) using the aforementioned parameters (Canadian Standard Association, 2006).

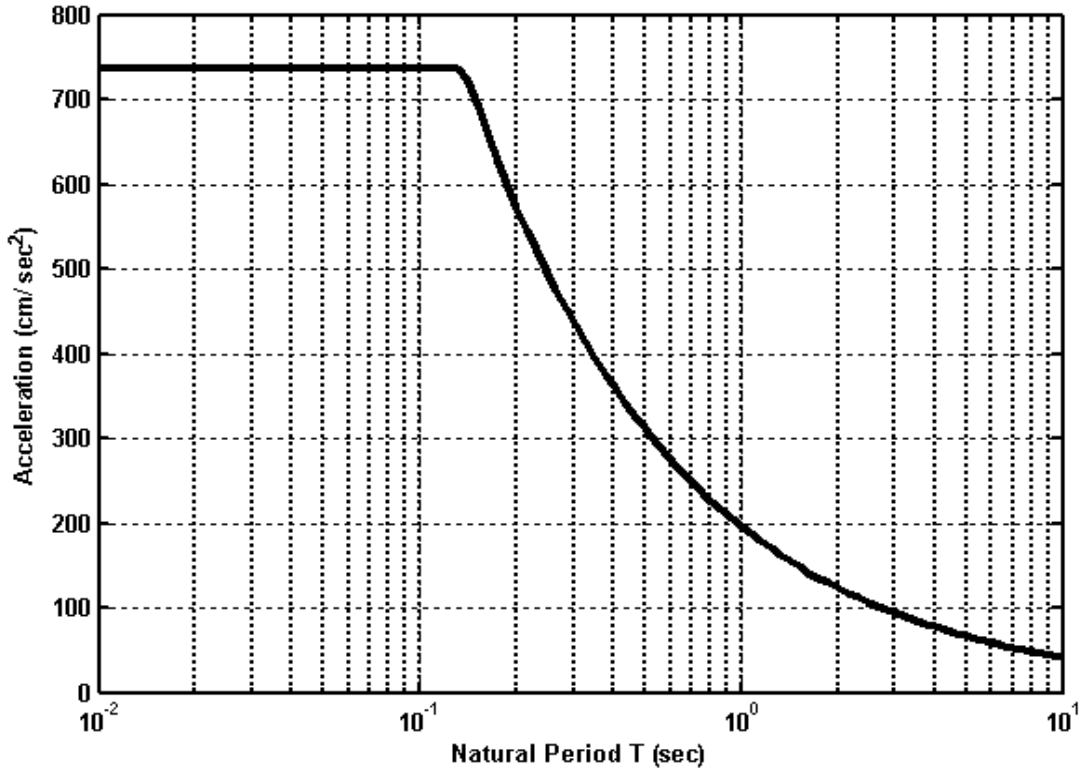

Figure 27. Mississippi River Bridge response spectra based on (CHBDC) (CAN/CSA, S6-06).

Figure 28 shows the response spectra for the selected earthquakes (from Atkinson (2009)), compared to the bridge RS. The plots show that the RS are in good agreement for the time periods in the range of interest for the bridge. However, outside this range, the frequency content of the earthquakes have a wide variability, some below the bridge RS, some at the bridge RS, while others exceed it.

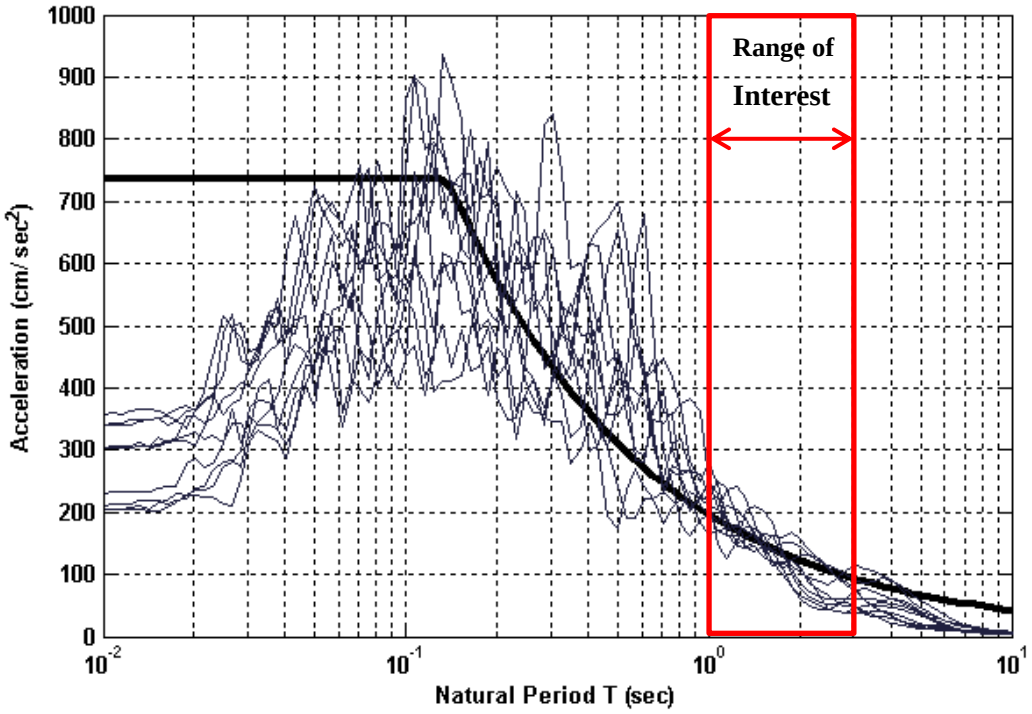

Figure 28. Selected seismic events response spectra compared to the bridge response spectra.

Table 2 shows the properties of the selected seismic records. The table shows the earthquake numbers based on the numbering procedure provided by Atkinson (2009) for the earthquake category *"east7d2"*. The mean of the ratio RS_B/RS_E is used to modify the earthquake records and RS to be in agreement with the target RS of the bridge. The lowest standard deviations of the ratio RS_B/RS_E were used to select 10 earthquake records from a total of 46 records in the database appropriate for this location. The peak ground accelerations for the selected earthquakes range between a minimum of 0.205 g to a maximum of 0.363 g.

Table 2. Statistics for the selected earthquakes.

EQ. #	Mean RS_B/RS_E	STD RS_B/RS_E	Peak Ground Acceleration (g)
1	0.96	0.25	0.30
3	1.08	0.27	0.34
5	1.68	0.16	0.36
9	0.82	0.24	0.20
15	1.64	0.22	0.30
27	1.86	0.18	0.23
29	1.75	0.23	0.34
36	1.76	0.24	0.21
41	1.50	0.25	0.21
44	1.51	0.23	0.31

Atkinson (2009) suggests a minimum of five time history analyses, using five different spectrum compatible seismic records. For the current analysis, ten spectrum compatible earthquake records were grouped into five earthquake combinations (one in each direction). Each earthquake combination consisting of two earthquake records was applied to the bridge at different directions; both of the seismic excitations were applied at the piers and abutment footings. The earthquakes were grouped based on the peak ground accelerations (see Table 3); note that, higher peak ground acceleration does not necessarily produce larger bridge responses.

Table 3. Selected earthquake records combinations.

Combination #	Longitudinal Direction (x)	Lateral Direction (z)	Combination Description
1	5	3	Both directions with highest PGA
2	41	9	Both directions with lowest PGA
3	29	36	A high PGA in the longitudinal direction and a low PGA in the lateral direction
4	27	44	A high PGA in the lateral direction and a low PGA in the longitudinal direction
5	1	15	Both directions have medium PGA's

The five earthquake combinations were used to perform five time history analyses for each simulation case. Various simulation cases will be discussed in the next section. Figure 29 shows the earthquakes acceleration records, where the units are in cm/sec^2. The duration of the earthquake records vary from 12 seconds to 18 seconds.

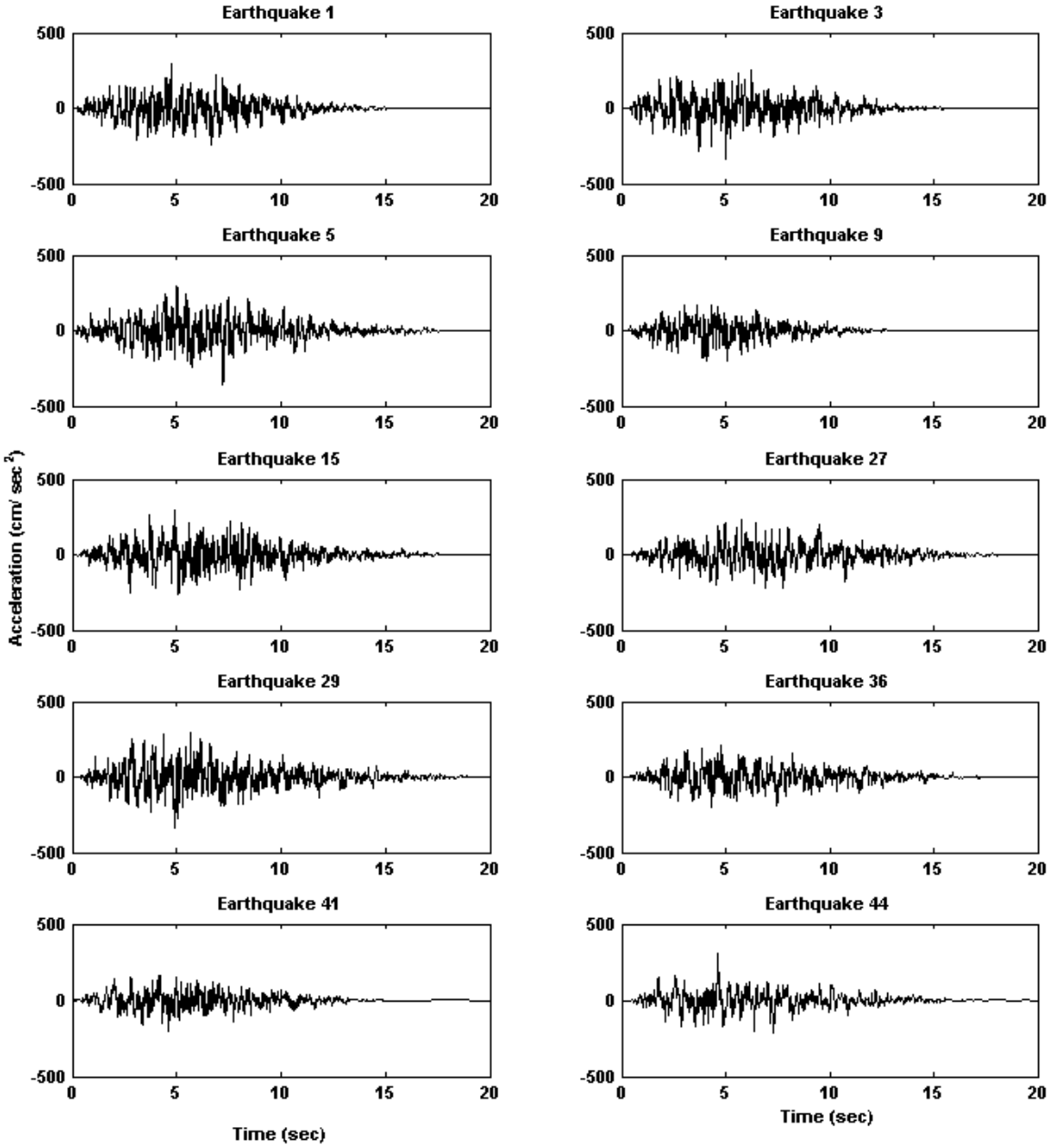

Figure 29. Accelerograms for selected earthquakes.

4.2 Test Cases

To be able to validate and test the efficiency of retrofitting bridges using viscous dampers, the performance of various hypothetical retrofit options will be studied and compared. Furthermore, using test cases that were previously used in other studies are included to provide additional comparisons and benchmarks for analysis.

Seven test cases were used for this analysis, each associated with a simulation model. These test cases differ in the type of isolation bearings used, bearing distribution, the presence of viscous dampers, and the capacity of the viscous dampers (damping coefficient).

4.2.1 Unisolated Case: Pinned Case

In this case, the bridge deck was pinned to the piers and abutments (see Figure 30), without any isolation bearings. This case is intended to provide a baseline performance of the bridge to other cases, and is not expected to be a viable retrofit option. Moreover, the effectiveness of using an isolation system can be measured by comparing the results to this unisolated system. The pin connections between the piers and the deck only restrain the three translational degrees of freedom, but do not restrain the rotational degrees of freedom. However, at the abutments the longitudinal degree of freedom was released between the super structure and the abutments. The longitudinal direction was released to account for the thermal expansion that may occur in the bridge.

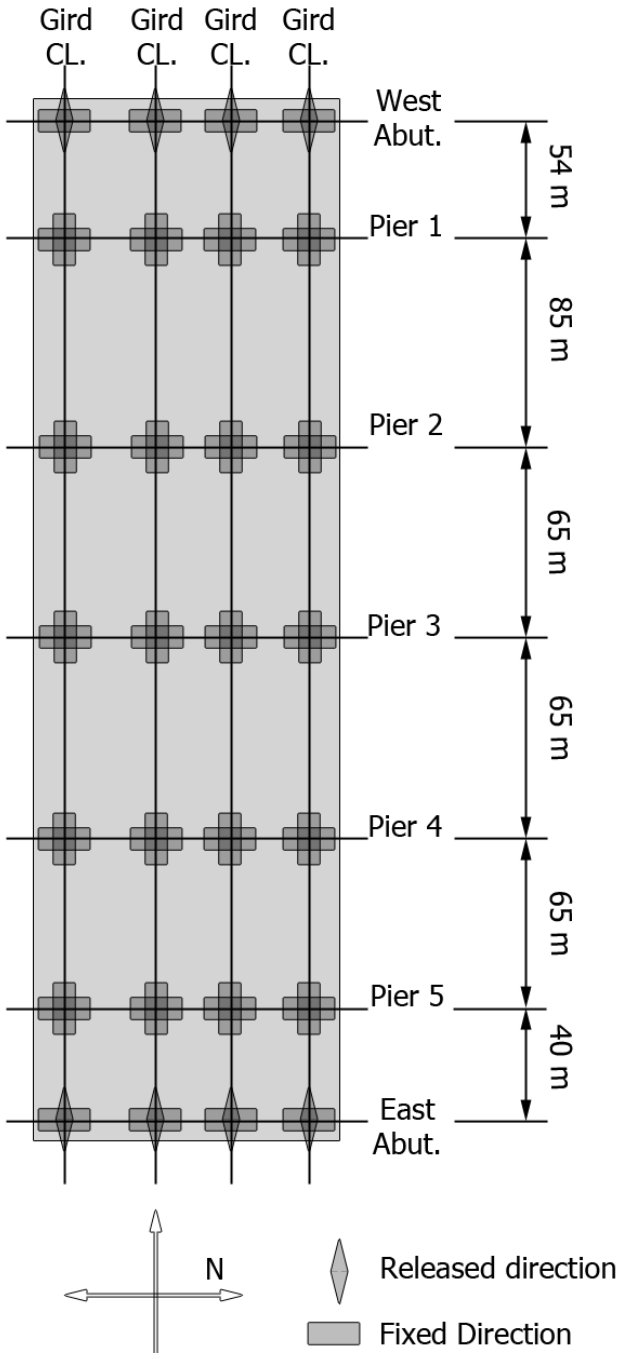

Figure 30. Baseline unisolated case.

4.2.2 Isolated Case: Hybrid Bearings

This case reflects the existing condition of the Mississippi River Bridge. Four FP bearings are located at the top of each pier, while the abutments contain four LE bearings (see Figure 31).

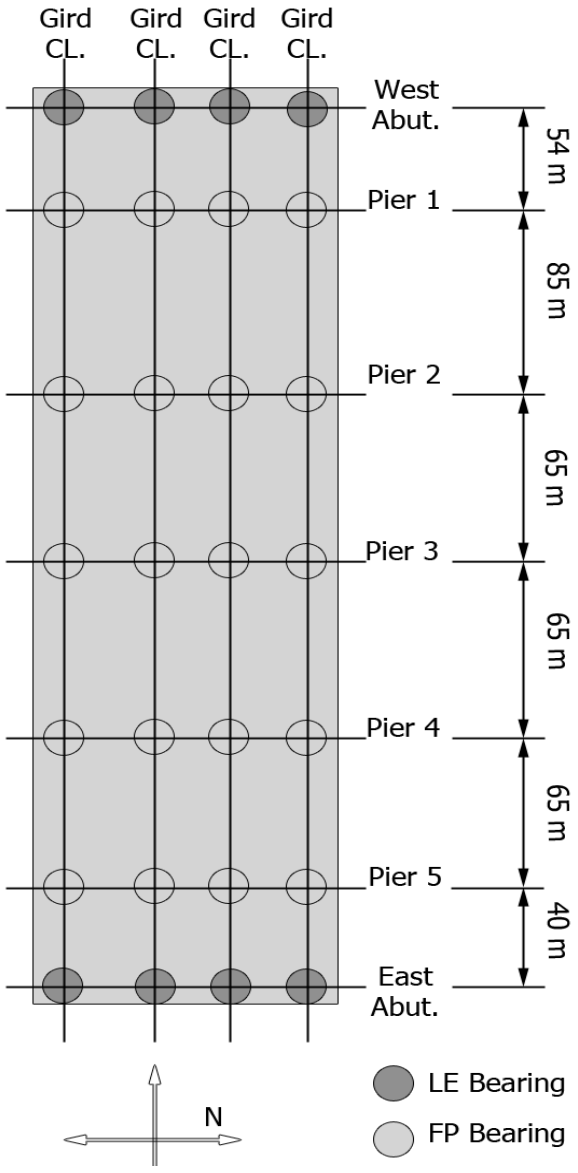

Figure 31. Isolated case: Hybrid bearings.

4.2.3 Isolated case: Friction Pendulum Bearings

The only difference between this and the hybrid case previously discussed is that the LE bearings at the abutments were replaced by FP bearings. This case was also analyzed by other researchers (Murat Dicleli, 2002), who also concluded that the hybrid case is a better option compared to this setup (see Figure 32)

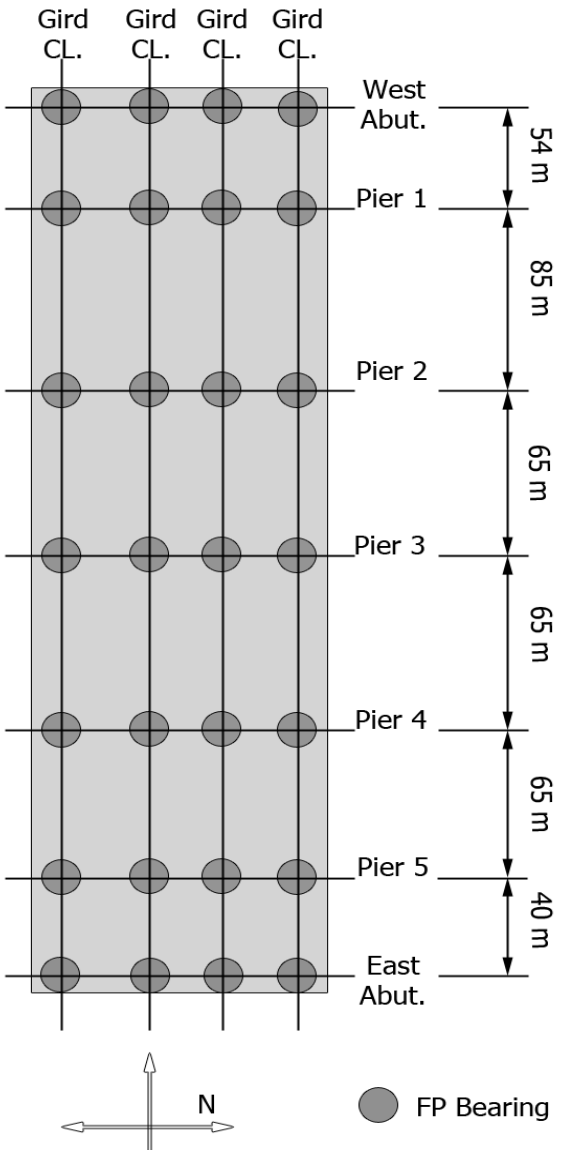

Figure 32.Friction pendulum bearings bridge setup.

4.2.4 Isolated case: Linear Elastomeric Bearings

In this setup all the bearings at the piers and the abutments are LE bearings. This setup shows the effect of having a perfectly linear isolation system, which for subsequent cases will be augmented with viscous dampers.

4.2.5 Isolated case: Linear Elastomeric Bearings with Viscous Dampers

In this case, viscous dampers (dashpot elements) are added in parallel to LE bearings. The viscous dampers are located at the bearings locations in the longitudinal and the lateral directions (see Figure 33).

Three sizes of viscous dampers (represented by their damping coefficients) were studied. Instead of randomly selecting the damper capacities, a simple procedure was used to calculate the damping coefficients based on the bridge super structure mass and the stiffness of the bearings. The method used to obtain the damping coefficients is as follows.

$$C = 2\xi\omega \qquad 4.1)$$

where C is the damping coefficient, ξ is an arbitrary damping ratio, ω is the overall frequency of the bridge assuming a single-degree-of-freedom representation, which is calculated using

$$\omega = \sqrt{\frac{K}{M}} \qquad 4.2)$$

where M is the total superstructure mass and $K = \sum_{i=1}^{n} k_i$ where k_i is the bearing i stiffness and n is the number of bearings supporting the bridge superstructure.

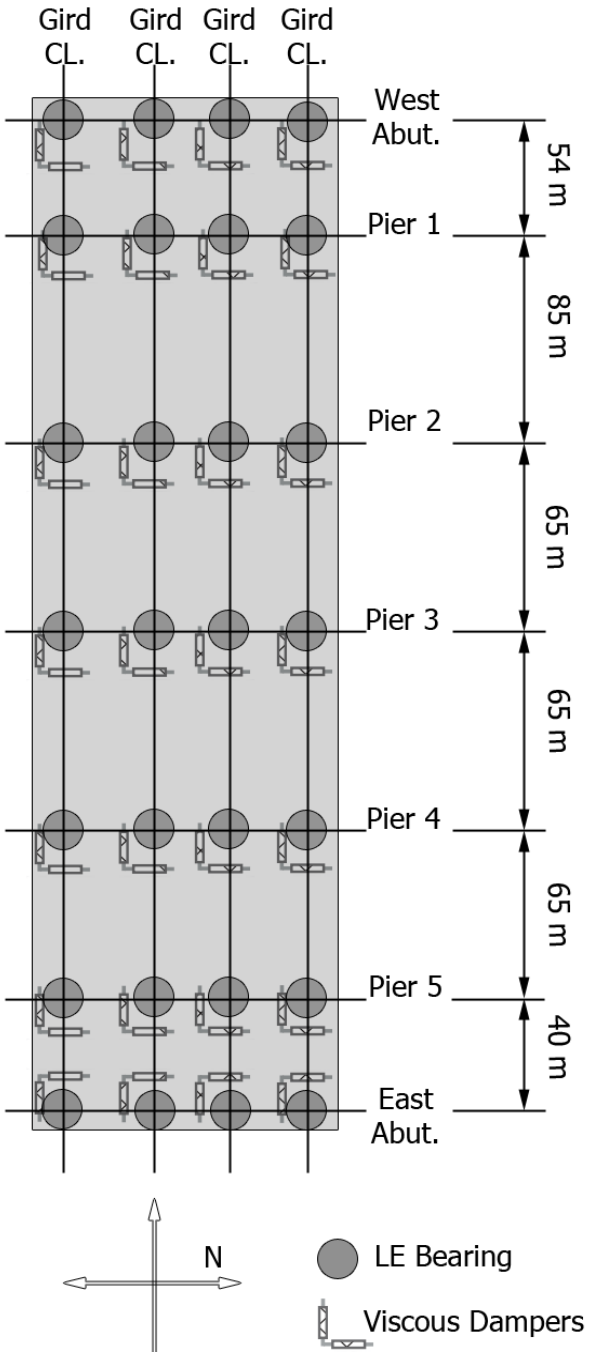

Figure 33. Linear elastomeric bearings with viscous dampers setup.

In this procedure the entire superstructure is assumed to be a single degree of freedom system with a mass equal to the mass of the entire deck including the girders and stiffness equal to the sum of the bearings stiffnesses. The damping ratio was fixed to 5%, 10% and 15% critical, and the resulting damping coefficients for the individual dampers as well as the entire system are tabulated in Table 4.

Table 4. Viscous Dampers Damping Coefficients and Damping Ratios

Damping ratio ξ	Structure Damping Coefficient $C \left(\text{kN.sec}/\text{m}\right)$	Damper Damping Coefficient $c_i \left(\text{kN.sec}/\text{m}\right)$
5 %	52360	1870
10 %	104720	3750
15 %	157080	5620

Note: in Chapter 5 section 5.6 non-linear fluid viscous dampers were also used and discussed.

4.3 Performance Indices

Often, a single performance variable is not sufficient to evaluate the performance of the retrofit strategy. Multiple (competing) criteria need to be viewed together to judge their adequacy and relative advantages. In this thesis, five performance indices are used for evaluation purposes. These indices range from force quantities (shear and moment) to the isolation level responses (of the bearings). Such indices have been reported in earlier studies on bridge performance to seismic events (Agrawal, et al., 2009; Nagarajaiah, Narasimhan, Agrawal, & Tan, 2009). They are described below:

Table 5. Performance Indices.

Performance indices	Measuring locations
Peak Base Shear	At the bottom of the pile caps of the piers and the abutments (see Figure 34)
Peak Overturning Moment	At the bottom of the pile caps of the piers and the abutments (see Figure 34)
Peak Bearing Deformation	The horizontal displacement difference between the top and bottom of the bearings at the piers and the abutments (see Figure 34)
Peak Mid-span Displacement	At all bridge mid-spans (see Figure 34)
Peak Mid-span Acceleration	At all bridge mid-spans (see Figure 34)

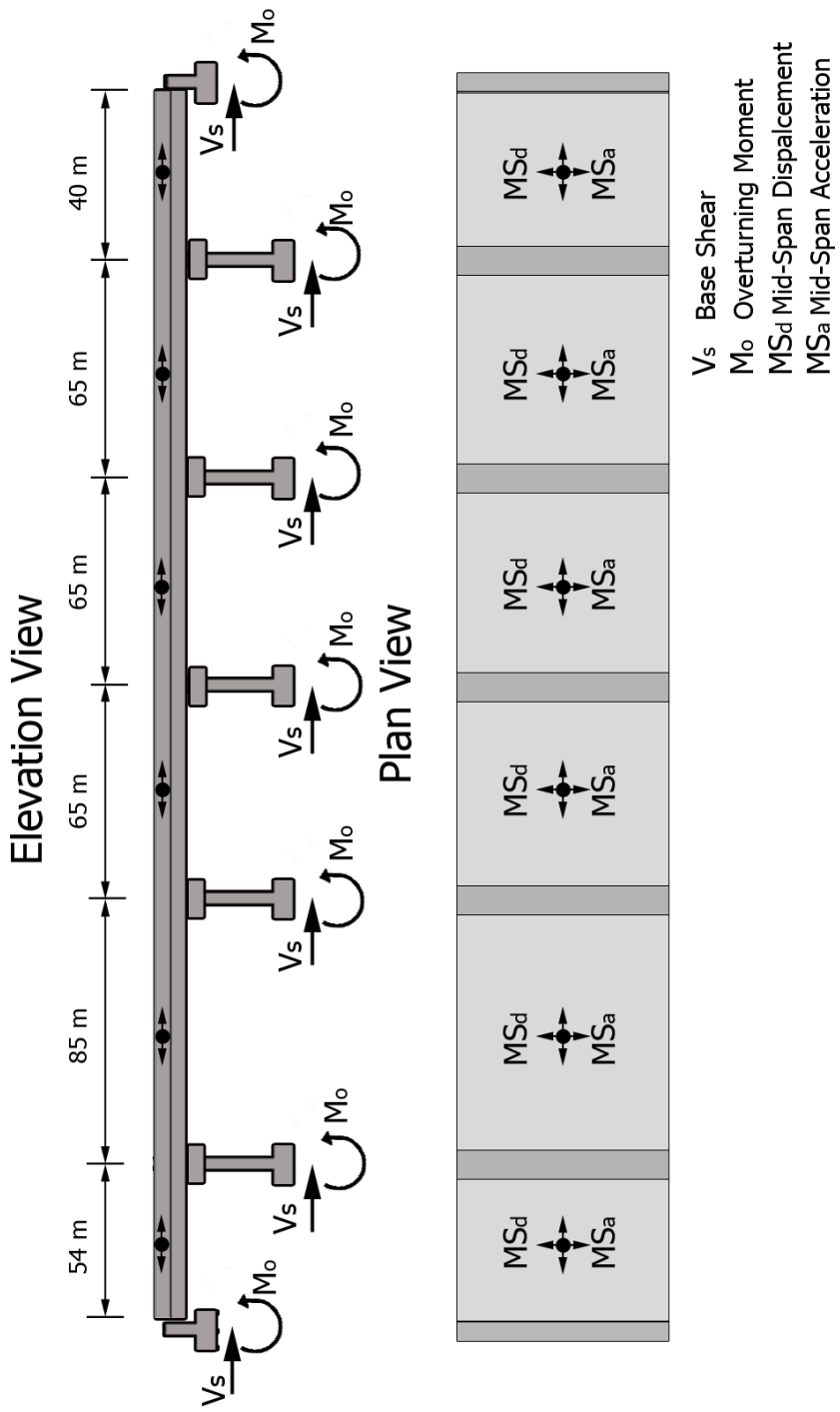

Figure 34. Performance indices measurement locations.

Chapter 5
Analysis Results

In this chapter, the results of the time history analysis are presented and discussed. Where applicable, the results are compared to the results available in the literature. The results are presented mainly in terms of performance indices previously described, for various cases. Figures are included to illustrate the main features.

5.1 Mode Shapes

In this section the mode shapes and natural periods for various simulation cases are presented. The OpenSees finite element model is shown in Figure 35.

Mode shape analysis helps understanding the vibration shape of structures under free vibration; they provide a linear expansion of the response in terms of orthogonal basis vectors. Physically, they provide insight into the response characteristics of a structure. Applicable to linear systems, they are often used with nonlinear systems as well through the process of linearization. In most cases, a few fundamental modes contribute to the majority of the structural response. This aspect is the basis for the response spectral approach in building codes. In the current study, a time-domain approach is undertaken.

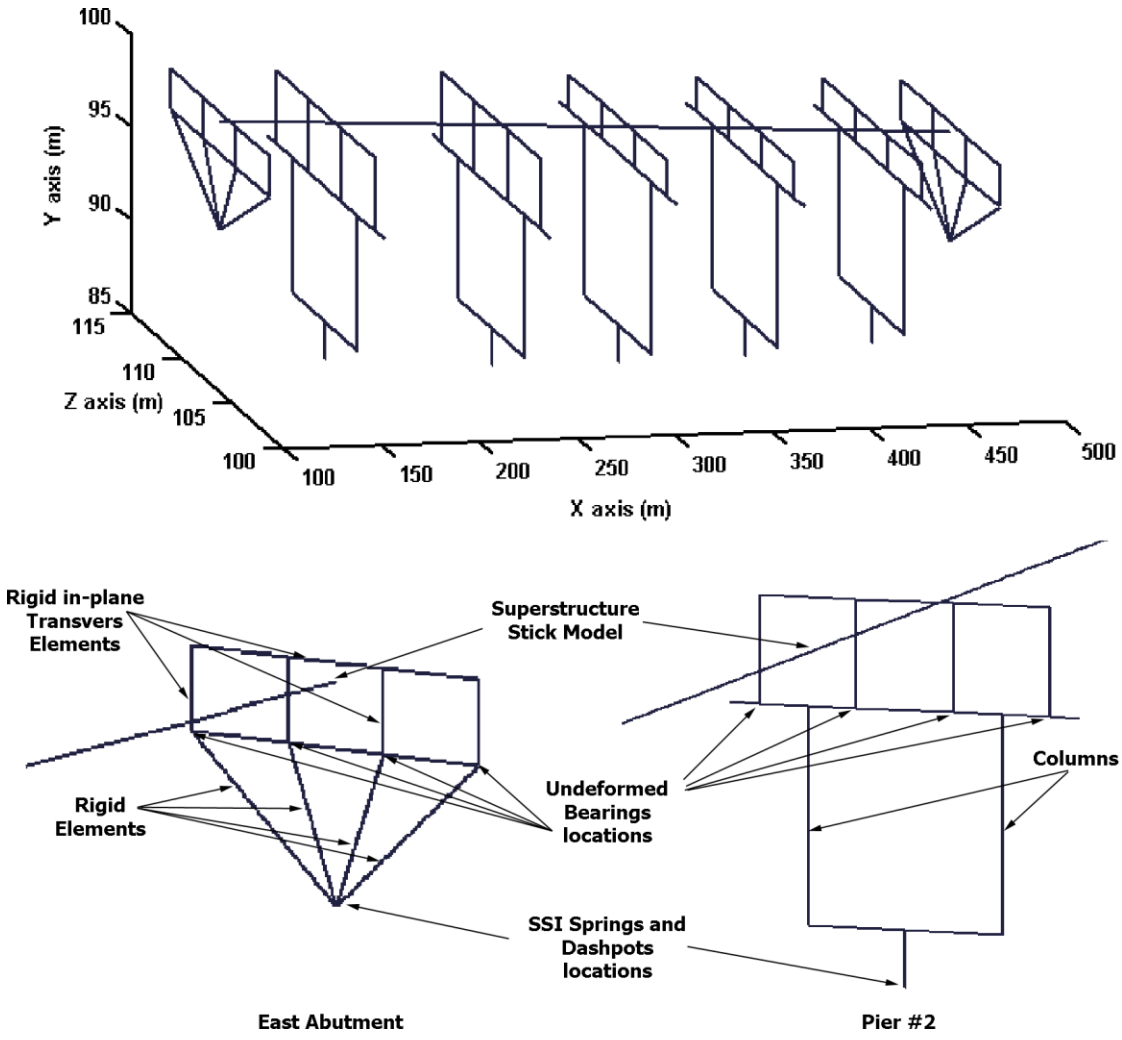

Figure 35. Mississippi River Bridge OpenSees finite element model.

Figure 35 shows the key characteristics of the finite-element model, and the idealizations used in constructing the OpenSees finite element model. The locations of the bearings in the un-deformed case are also shown. Please note that the bearing deformations are illustrated as a discontinuity between the girders and the pier cap. However, this is not physical, but merely an illustration. The locations of the soil-structure interaction springs and dashpots are also shown in Figure 35 , but are not visible

in their un-deformed state. However, when any deformation occurs in these elements, such deformations will appear as lines in the deformed plots.

For the sake of brevity, only the first three modes in each case will be presented; however, the next three modes are presented in Appendix A.

5.1.1 Unisolated Case

The first mode shape for the unisolated case (pinned supports) is the transverse bending of the whole structure with peak magnitude at the center section the bridge. It is evident from Figure 36 that the soil springs contribute to the first mode, and hence cannot be ignored. The first mode also shows rotation of piers with respect to the x-axis. This mode of vibration has a fundamental period of 1.07 sec.

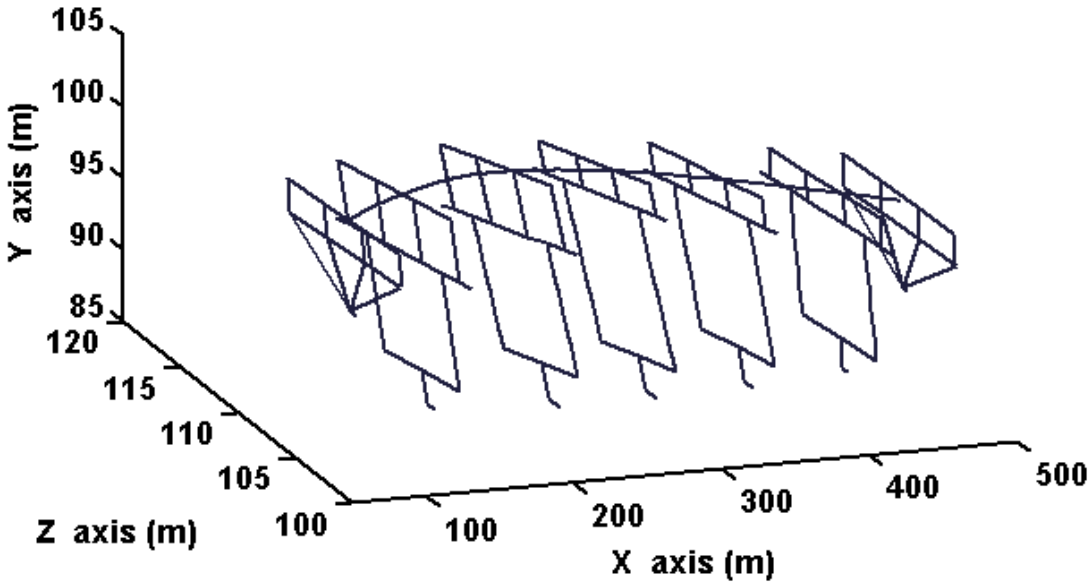

Figure 36. Pinned first mode, lateral bending deformation ***(T = 1.07 sec).***

The second mode for the unisolated case is shown in Figure 37. The second mode is a longitudinal mode, where the super structure deforms in the longitudinal (x-axis) direction. The discontinuity between the abutments and the in-plane elements is due to the released DOF

between the abutment and the deck. The SSI springs at the piers also contribute to this mode. The fundamental period of the second mode is very close to the first mode .

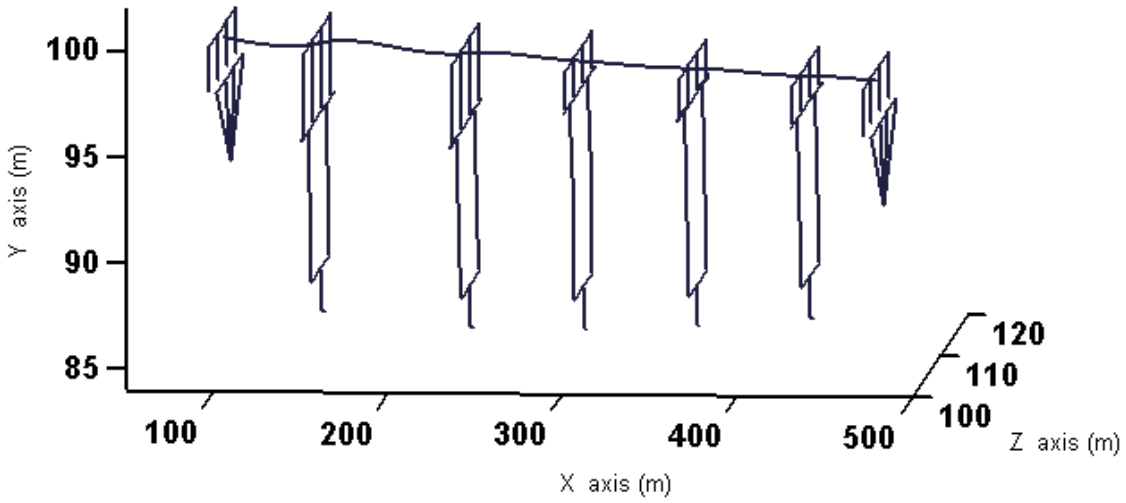

Figure 37. Second mode, longitudinal ***(T = 0.99 sec).***

The third mode of vibration this case has a fundamental period of 0.77 sec. The mode of vibration is a mix of torsional and transverse deformations. This mode of vibration includes the deformation of the SSI springs and the piers as well.

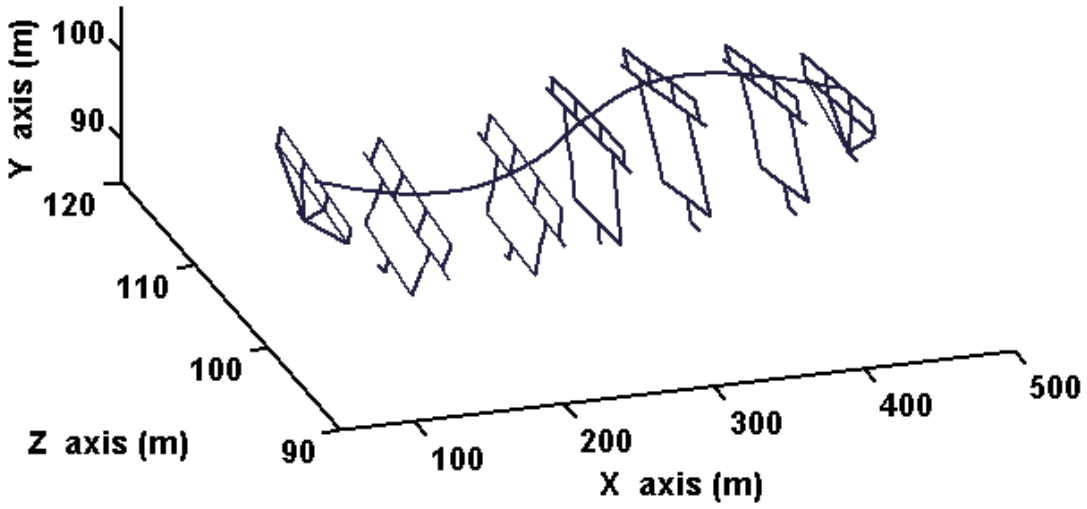

Figure 38. Third mode, lateral torsional bending ***(T = 0.77 sec).***

5.1.2 Isolated Case: Hybrid Bearings

The concept of modes is applicable only to linear systems. For nonlinear systems such as the hybrid isolated case, an approximate linearization method is employed by OpenSees. This involves linearizing the FP elements by taking the initial stiffness as the friction force divided by the yielding displacement $\mu N / u_y$. This yields an apparent stiffness higher than the actual stiffness of the bearing. Nevertheless, the results of the modal analysis still provides good approximation to the mode shapes, as the apparent stiffness of the FP bearings is relatively low compared to the rest of the structure.

Figure 39 shows the first mode of the hybrid case, which only involves the bearings and the superstructure, while the substructure remains un-deformed. The relatively low stiffness of the isolation bearings results in the superstructure moving independent of the substructure, as if the deck is a single degree of freedom system. It is expected that the

soil-structure interaction and the piers will play a less important role in this case, than for the unisolated case.

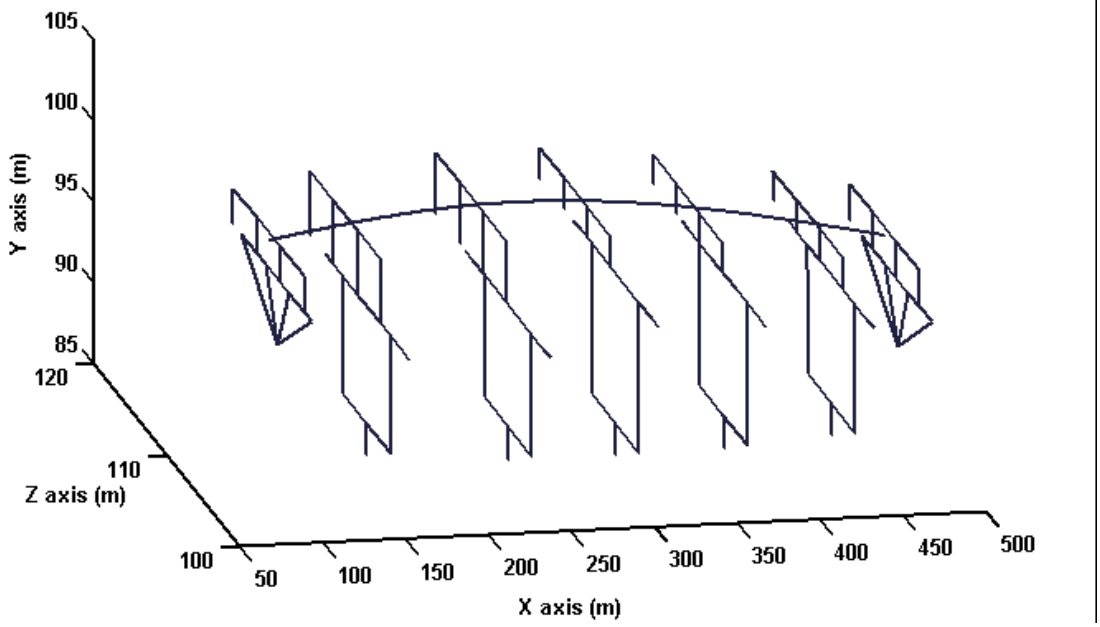

Figure 39. First lateral mode for the hybrid isolated case ***(T = 1.28 sec).***

The second mode of the hybrid setup is shown in Figure 40.This mode of vibration is in the longitudinal direction, and similar to the first mode, the isolation bearings deform and the super structure behaves as an isolated single degree of freedom system. The natural period of the lateral mode is lengthened (1.28 sec) compared to the unisolated case (1.08 sec), which is to be expected. However, the linearized structure is stiffer than the actual case, as only the initial stiffness is considered, whereas during a seismic event, the structure is in the yielding mode. The second mode is lengthened (1.11 sec) compared to its unisolated counterpart (0.99 sec).

The third mode of vibration is a transverse flexural mode. The natural period corresponding to this mode is 0.97 sec.

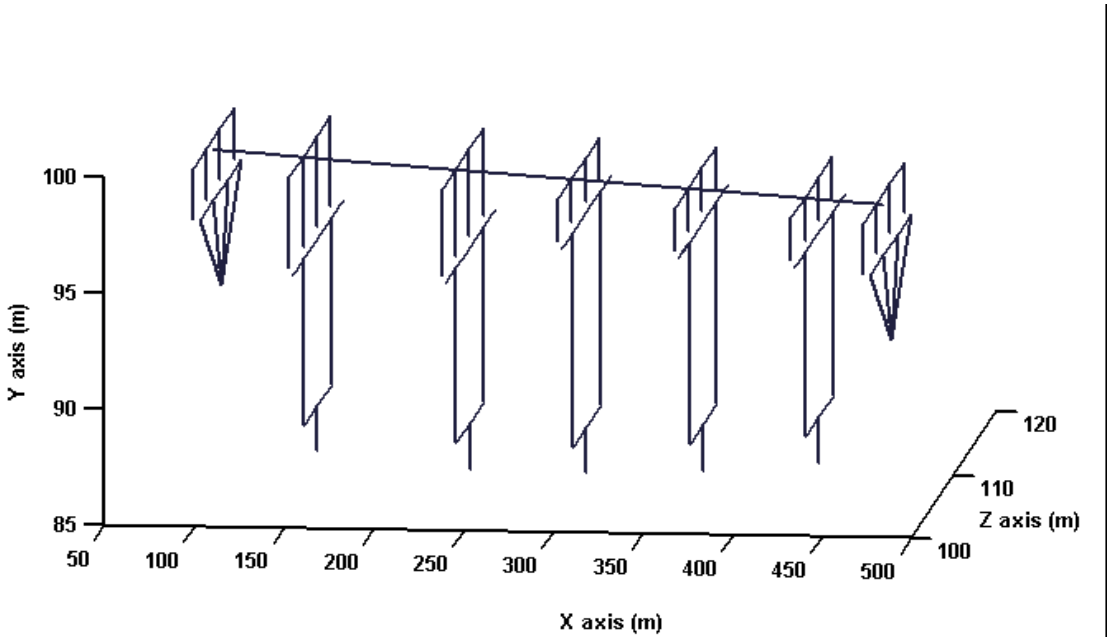

Figure 40. Second mode, longitudinal ***(T = 1.11 sec).***

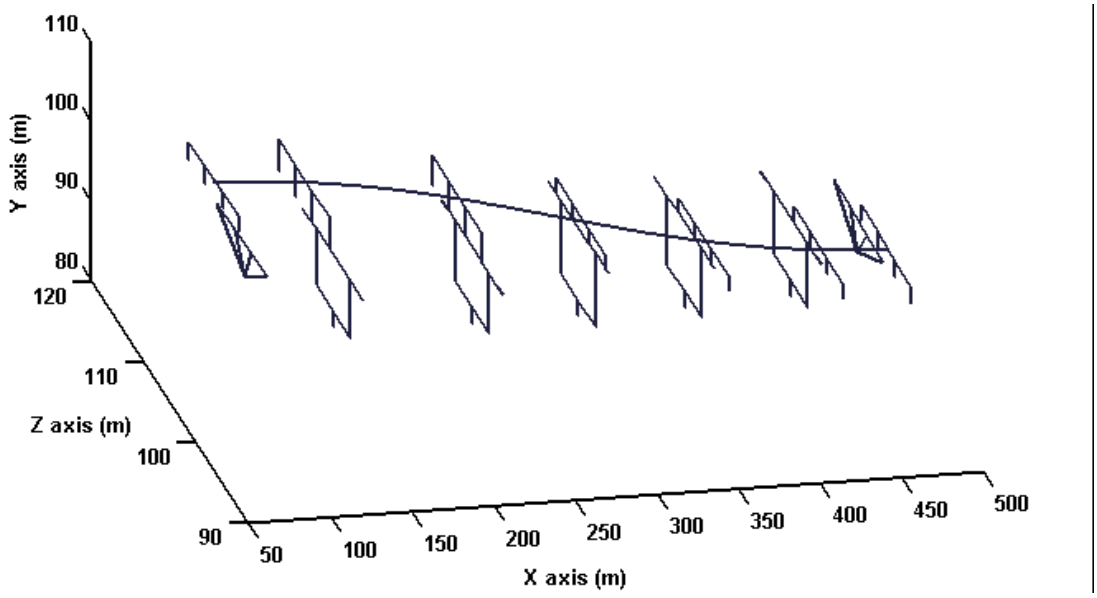

Figure 41. Third mode, which is flexural in the lateral direction ***(T = 0.97 sec).***

5.1.3 Isolated case: Friction Pendulum Bearings

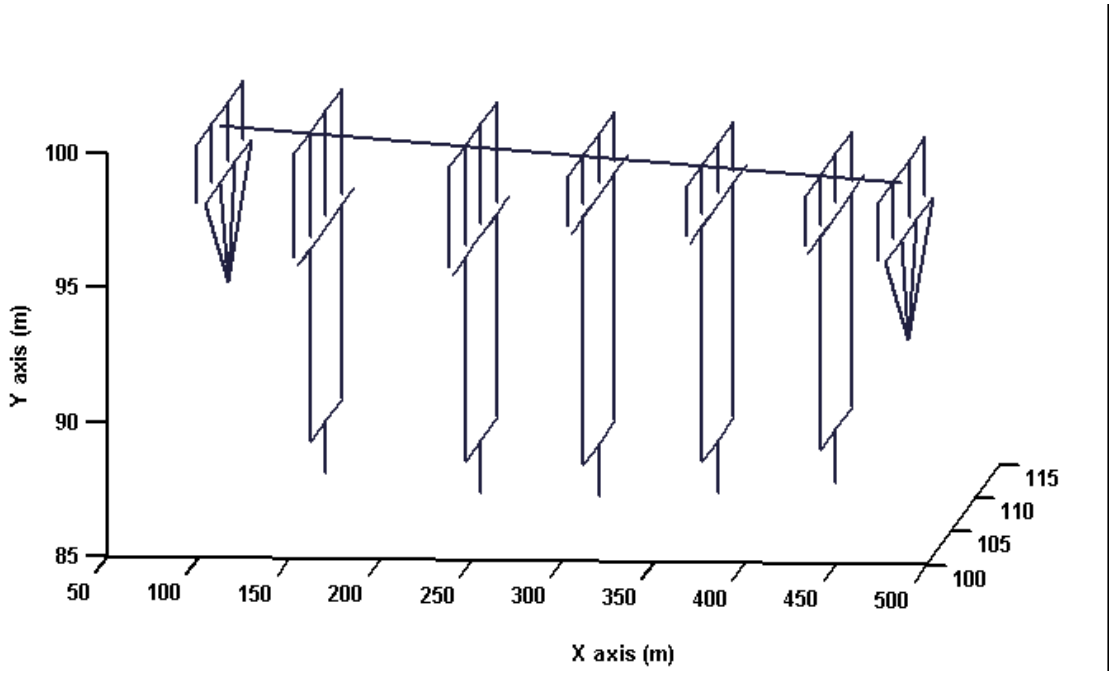

Figure 42. . First mode, longitudinal ***(T = 1.21 sec).***

The first mode for the FP isolation case is a longitudinal mode of vibration, where only the FP bearings are deformed (see Figure 42). The second mode is a transverse mode where the highest deformation occurs at the east abutment, and the bearings at the first pier remain relatively un-deformed (see Figure 43). The third mode is a twisting mode (about the y axis), where the FP bearings at each side of the bridge are deformed in the opposite directions (see Figure 44).

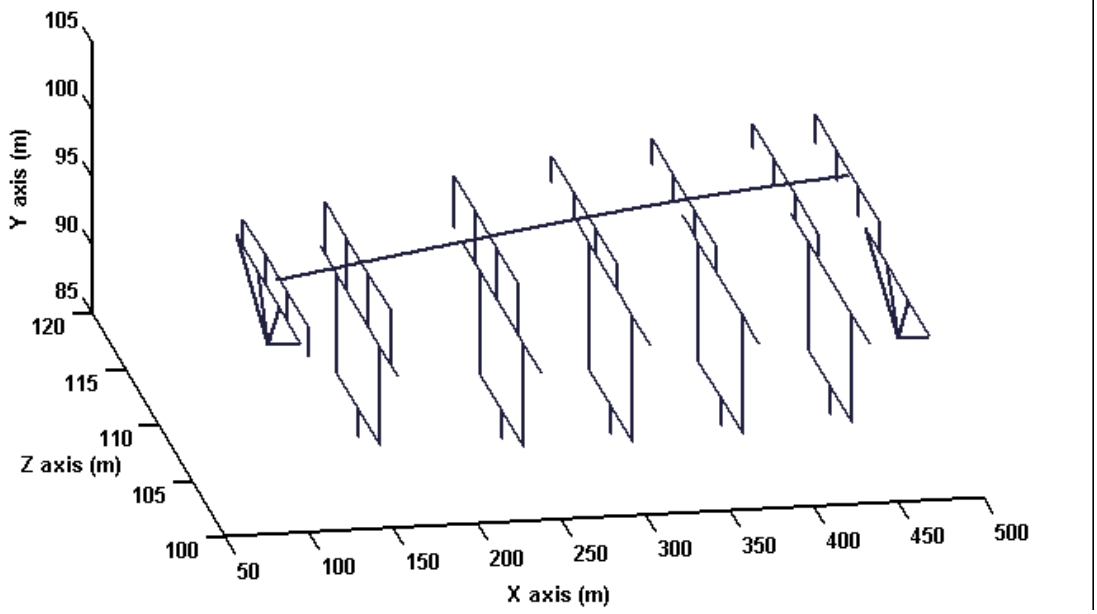

Figure 43. Second mode, lateral ***(T = 0.90 sec).***

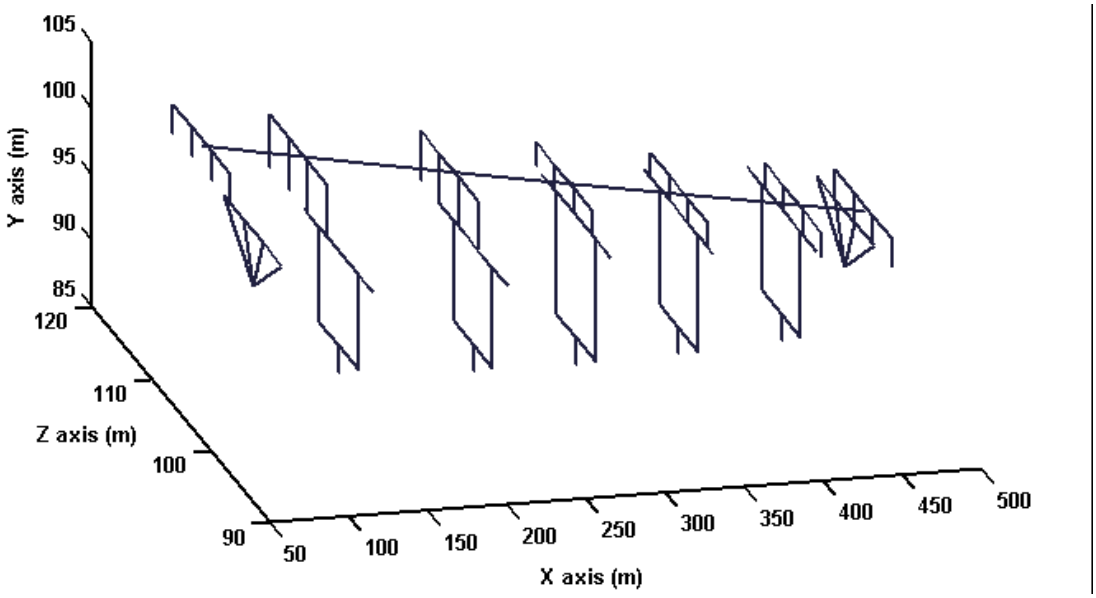

Figure 44. Third mode, twisting about the y axis ***T = 0.79 sec).***

5.1.4 Isolated case: Linear Elastomeric Bearings

The first mode is a lateral mode, second longitudinal and the third is a flexural lateral mode. However, unlike the hybrid and FP setups there is a slight contribution of the SSI interaction springs in the modes. This is due to the higher stiffness of the LE bearings compared to the FP bearings (see Figure 45 & Figure 46). The third mode of the LE setups is predominantly a flexural-transverse mode with a very low torsional deformation (see Figure 47).

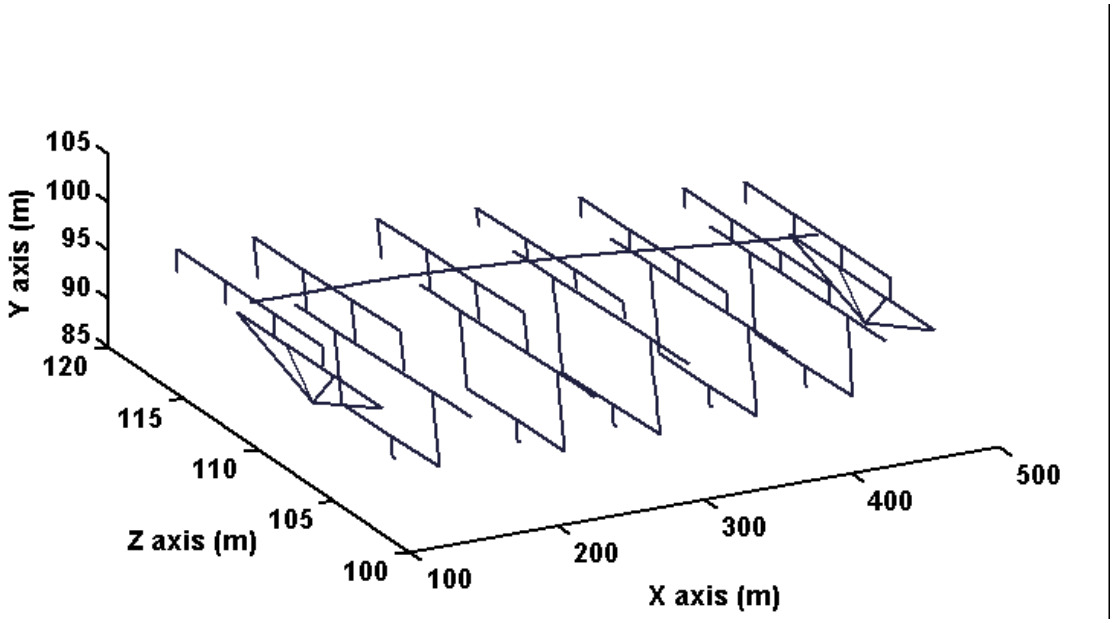

Figure 45. First mode, lateral ***(T = 2.25 sec).***

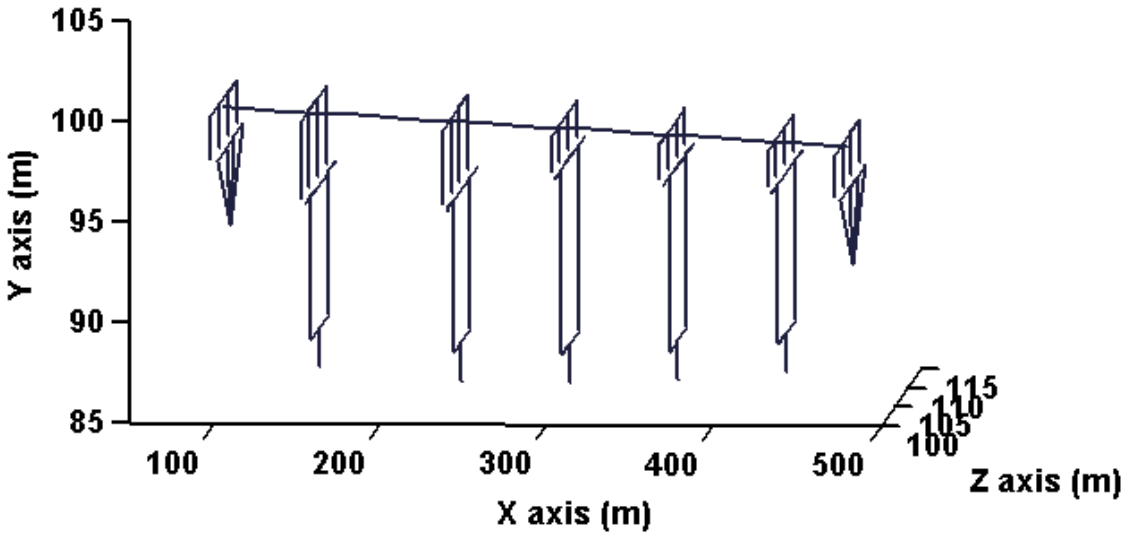

Figure 46. Second mode, longitudinal ***(T = 2.01 sec).***

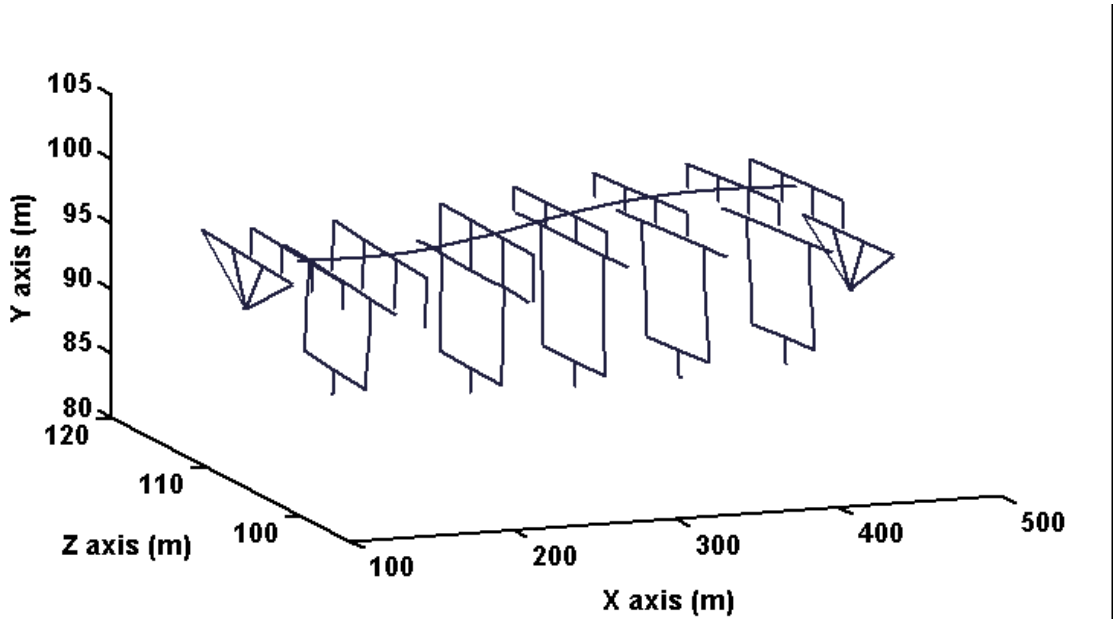

Figure 47. Third mode, lateral flexural ***(T = 1.47 sec)***

5.2 Evaluating the response for various cases

In this section, the results are presented in terms of performance indices (described in Chapter 4, Sec 4.3.). The results are shown graphically, while the numerical values are tabulated in Appendix B. The response indices are compared for all cases and for all the earthquake combinations.

First the response indices corresponding to the pier and abutment are presented, followed by the performance indices at the mid-span. The performance indices corresponding to the peak base shear, peak overturning moment, peak mid-span displacement, and peak mid-span acceleration for the different cases were normalized to the corresponding response indices of the unisolated (pinned) case.

Figure 48 shows the peak base shear (PBS) at the piers and abutments. Each plot represents the PBS of a pier or an abutment as titled. The x-axis of the plots is the earthquake combination number while the y-axis is the normalized response index. The plots show that the pinned case results in the highest base shear at the piers. The remaining cases results in values that range from 50% to 80% of base case. However, in most cases the presence of nonlinear FPS bearings result in higher PBS at the piers compared to the LE setups, with and without dampers. The LE case and the LE with 5% damping case results in the lowest PBS values at the piers, and their values are very close to each other.

Increasing the damping coefficient 5% for the LE case values increases the PBS where increasing the damping results in increasing shears. On the other hand, the PBS at the abutments show a different pattern compared to the piers.

The isolation case involving FP bearings result in PBS values lower than the unisolated case, while the case of LE bearings (with and without dampers)result in higher PBS at the abutments. The low PBS for the pinned case is mainly due to the released longitudinal degree of freedom. The FP cases result in lower PBS at the abutments due to the low normal force (weight) on the bearings at the ends of the bridge. However, this isn’t the

case for the hybrid case where the abutments are isolated using LE bearings. The high friction forces of the FP bearings at the piers attract higher forces to the piers, which result in a relatively low forces transferred to the abutments. The LE cases on the other hand, result in a better distribution of the loads between the piers and the abutments.

Figure 49 shows the peak overturning moment (POM) at the piers and the abutments. The results show similar patterns to the distribution of PBS. The POM is also normalized to the pinned case.

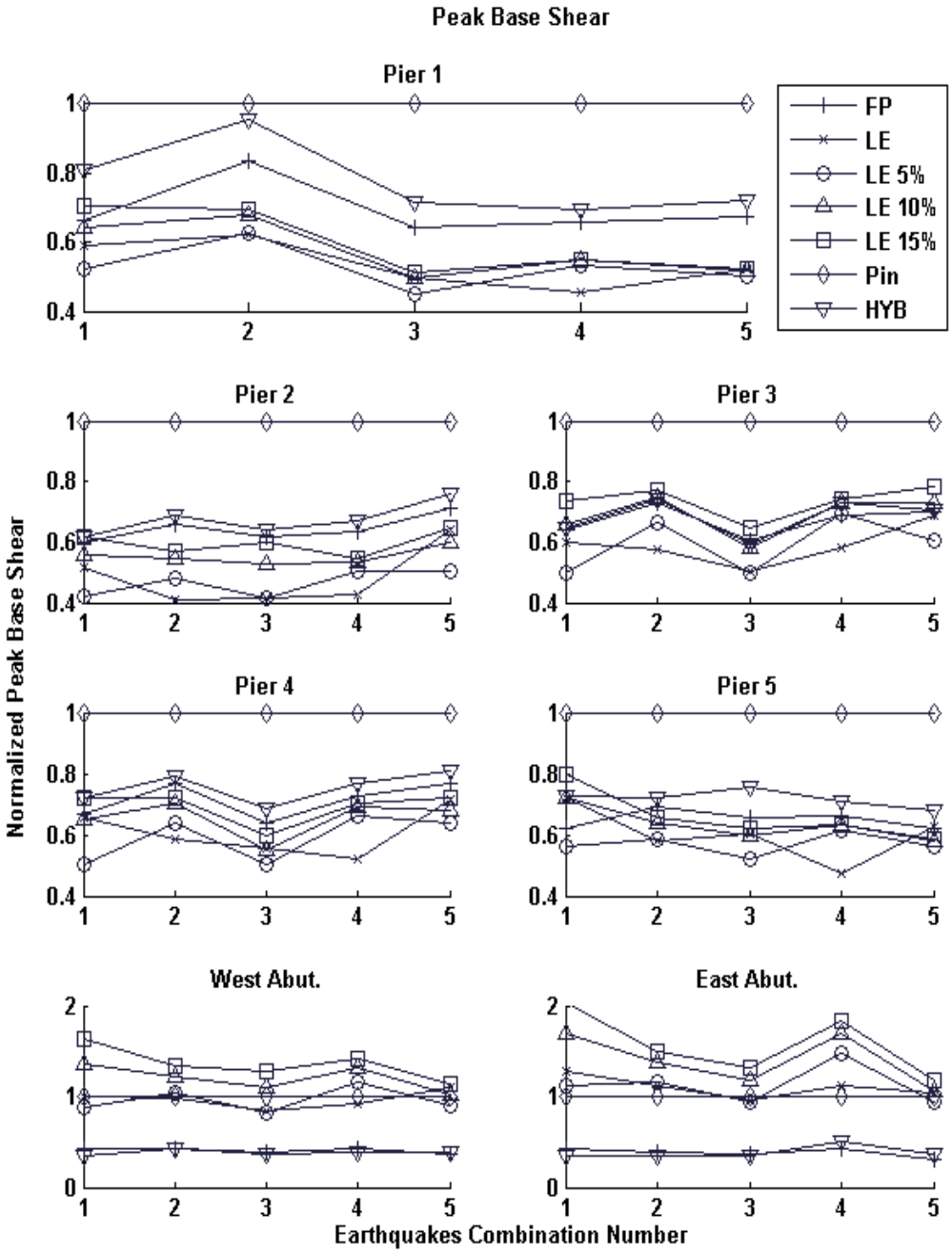

Figure 48. Piers and abutments peak base shear.

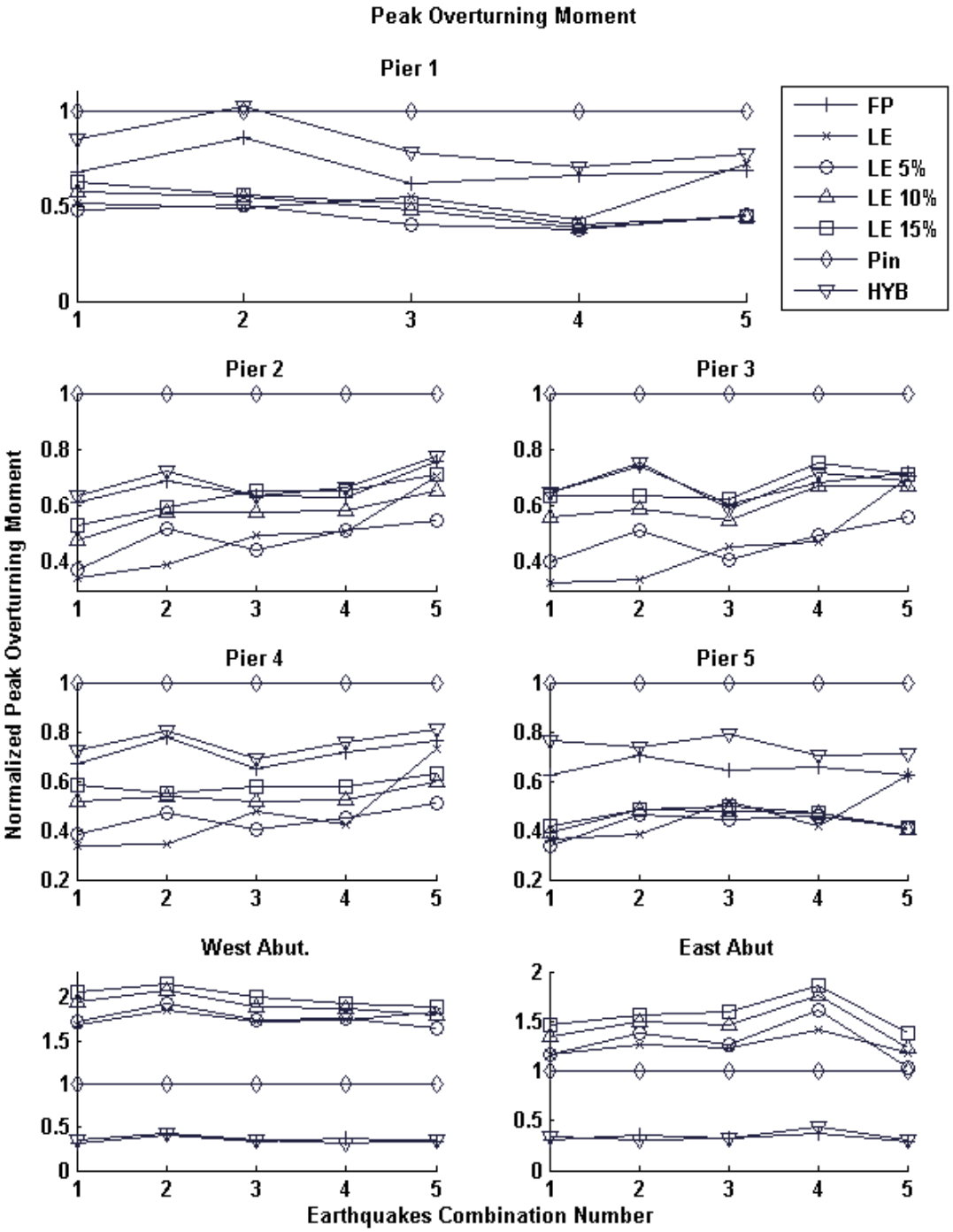

Figure 49. Piers and abutments peak overturning moment.

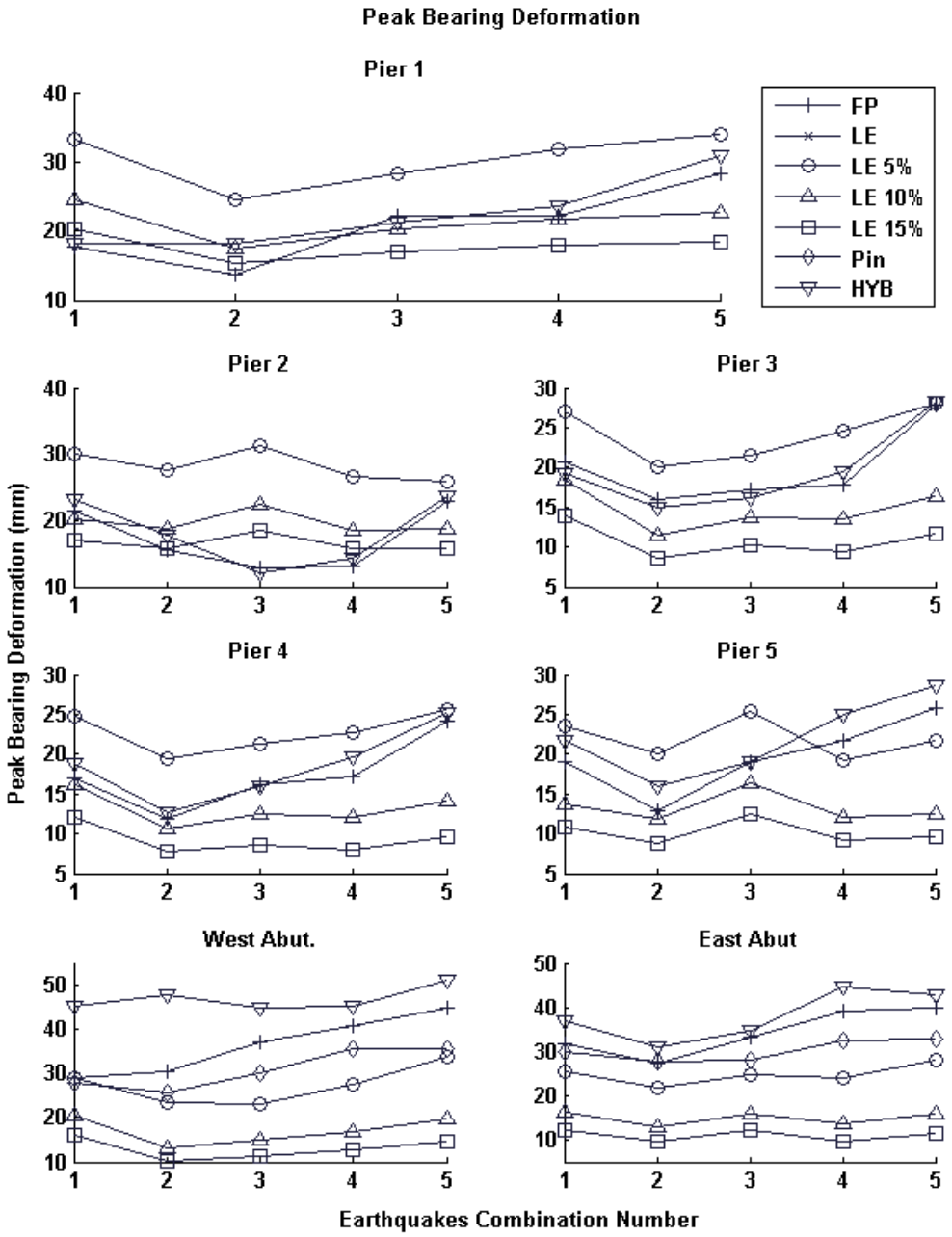

Figure 50. Peak bearing deformations at the piers and abutments.

The peak bearing deformations (PBD) for various cases are shown in Figure 50. The values of the PBD of the LE setup were omitted from the plots due to very high values

(around 130 mm). This is not surprising as for the case with LE bearings, no damping is assumed, which results in very high (unrealistic) values of PBD. In practice, the LE bearings contain small amount of material damping from rubber, but this was not included in this study.

The addition of viscous dampers to the LE isolation system dramatically reduces the PBD for the isolated case. Moreover, at 5% critical, the dampers reduced the PBD from 130 mm to 25 mm, while at 10% and 15% the PBD is reduced to approximately 17 mm and 10 mm, respectively.

The hybrid and FP cases show considerably high PBD amplitudes at the abutments. As mentioned earlier, the low stiffness of the bearings at the abutments allows for high deformations, but limits the shear forces transferred to the substructure abutments. On the contrary, the LE case with viscous dampers maintained a relatively uniform PBD at the piers and abutments. The pinned case had a uniform PBD, which is only present at the abutments due to the longitudinal release, which is about 30 mm.

Please note that the bridge in its current condition allows for a peak displacement of 110 mm, which is much higher than the values calculated in all the cases investigated.

The normalized peak mid-span displacements (PMD) (Figure 51) show that the LE system with viscous dampers result in the lowest PMD. Increasing the damping coefficient reduces the mid-span displacement; however, the reduction in PMD is marginal beyond the 10% damping value. The LE case with no viscous dampers was also omitted from the PMD plots, as it resulted in relatively high displacements. The lack of added damping for the pinned setup combined with the large structure flexibility resulted in high PMDs, which is similar in magnitude to the hybrid and FP cases.

Figure 52 show the normalized peak mid-span accelerations (PMA) for the bridge. The general conclusion from the results is that the cases with isolation bearings reduce the PMAs; however, in some cases the FP, LE and hybrid cases do exceed the pinned case.

Conversely, the LE case combined with viscous dampers managed to limit the PMA to lower levels.

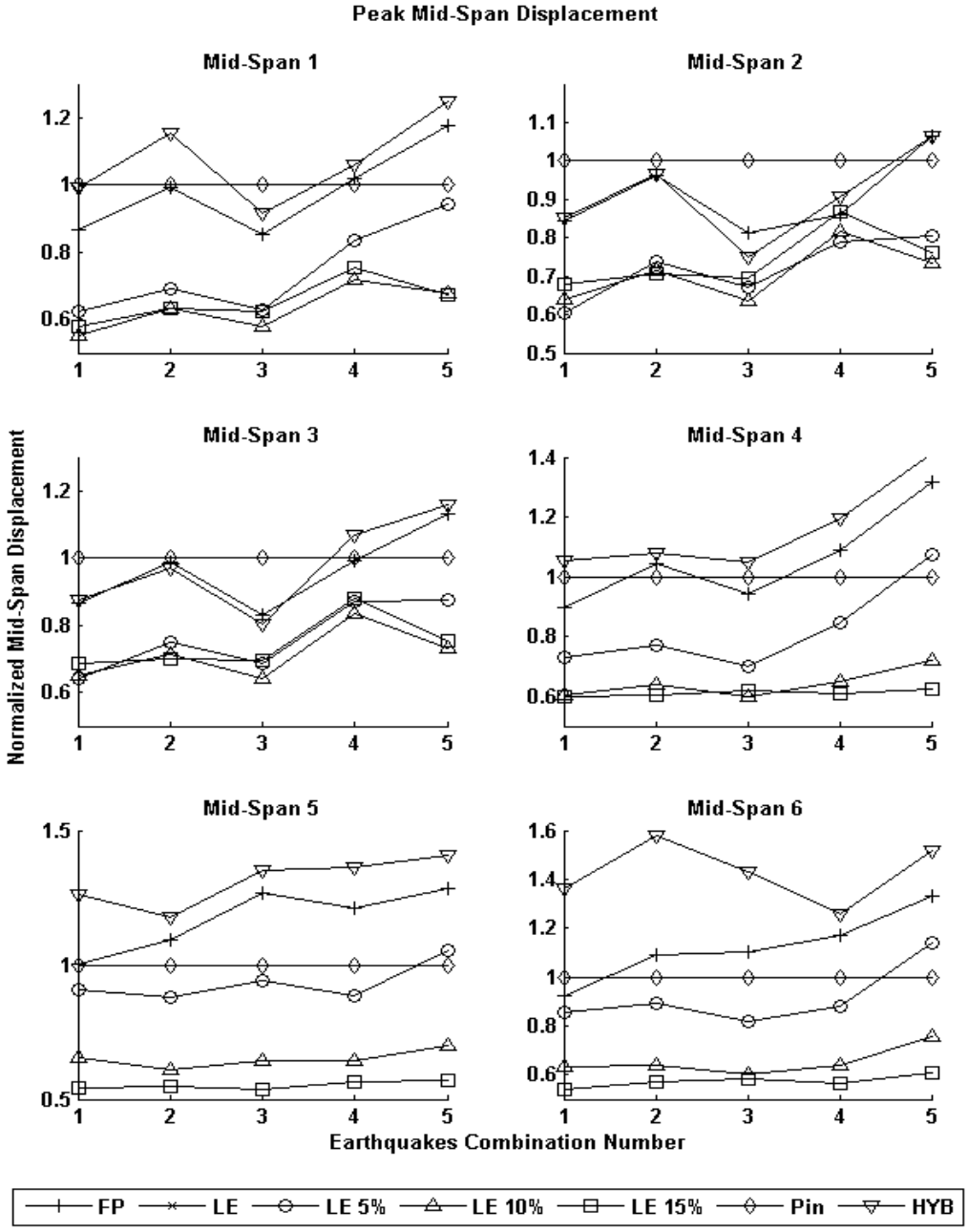

Figure 51. Peak mid-spans displacement.

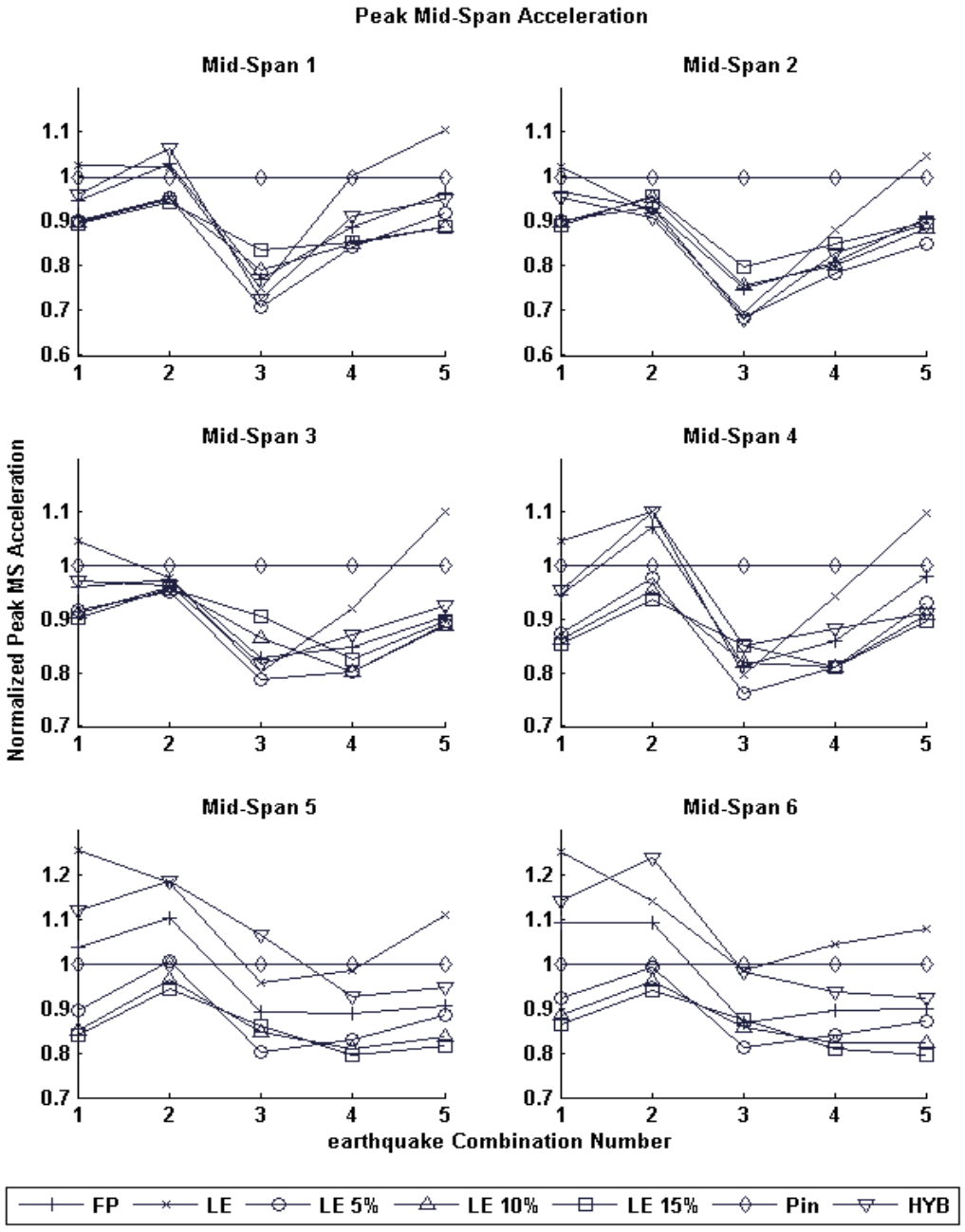

Figure 52. Peak mid-spans acceleration.

The next sets of figures show the performance indices for the entire structure. The values shown correspond to the maximum for all piers (peak base shear, peak overturning moment and peak bearing deformation) (see Figure 53 and Figure 54). Likewise, the peak

mid-span displacement and peak mid-span acceleration are the maximum obtained from all the bridge spans (see Figure 55). Those figures are meant to give a global overview of the seismic performance for different bridge cases considered in this thesis.

Figure 53 shows the piers peak base shear and the peak overturning moment. Both plots in the figure show a similar pattern. The unisolated case transfer much higher loads to the piers compared to the isolated cases. The hybrid and FP cases reduce about 30% of the loads of the unisolated case; however, the LE with and without viscous dampers cases managed to reduce the loads transferred to the piers more efficiently and reducing about 60% of the unisolated case loads.

The peak bearings deformation shown in Figure 54, as mentioned earlier, only show the PBDs of the piers bearings. The LE case gives very high bearings deformation compared to other cases due to the lack of energy dissipation at the bearings level in this setup. Implementing damping through fluid viscous dampers to the LE case strongly decreases the PBD. The cases with FP bearings (hybrid and FP cases) give slightly higher PBDs compared to the LE with viscous dampers cases.

Figure 55 shows the bridge peak mid-span displacements and peak mid-span accelerations. The LE case is omitted from the PMD plot due to the relatively large displacements. The PMD of the unisolated case show that high deformations can still occur in the structure. This could be due to the SSI and the flexibility of the bridge structure. In general, the LE with viscous dampers cases show lower PMDs than cases with FP bearings; in the same time, all isolated cases give lower mid-span displacements. However, the PMDs is not effected by the increase in damping at the bearings level. This is also the case for the PMA were different damping value give close results.

In summary, the absence of the vibration isolation system results in large forces transferred from the superstructure to the substructure. This results in large mid-span displacements and accelerations compared to the isolated cases.

The current configuration of the Mississippi River Bridge with hybrid isolation system and the FP case reduce the forces transferred to the substructure, while maintaining low displacement and accelerations at the mid-spans; nevertheless, these two configurations fail to evenly distribute the forces between the substructure elements. This observation is contrary to what was noted by Murat Dicleli, (2002).This could be due to the overestimated displacements resulting from the response spectrum analysis method. These displacements were used, in an iteration fashion, to obtain an effective stiffness for the linearized FP bearings by dividing the bearing force by the max bearing displacement. Consequently, the larger displacements gave very low linear stiffness to the FP bearings which in turn reduces the forces transferred to the piers and increases the forces on the abutments.

The LE isolation case presented herein results in a more uniform distribution of forces between the substructure elements. As a result, the forces transferred to the piers are much lower compared to the forces of the FP and hybrid isolation cases; yet, the bearings deformation and the mid-spans displacement are very high compared to any other setup, and exceed the allowable value of 110 mm.

The LE bearings equipped with viscous dampers setups show a better seismic performance in terms of the performance indices when compared to all other configurations analysed in this thesis. Moreover, the peak base shear and peak overturning moments were much lower at the piers compared to the existing configuration of the Mississippi River Bridge; similarly, the displacements of the bearings and mid-spans was also lower than the hybrid case. Specifically, the LE with% dampers results in the lowest base shear and overturning moment, while increasing the damping to levels of LE 10% and 15% increases the forces transferred to the piers. However, increasing the damping coefficients reduced the deformation of the bearings, where this reduction was marginal between the 10% and the 15% damping cases. The increase in damping did not however reduce the mid-span displacement or the mid-span acceleration in most cases.

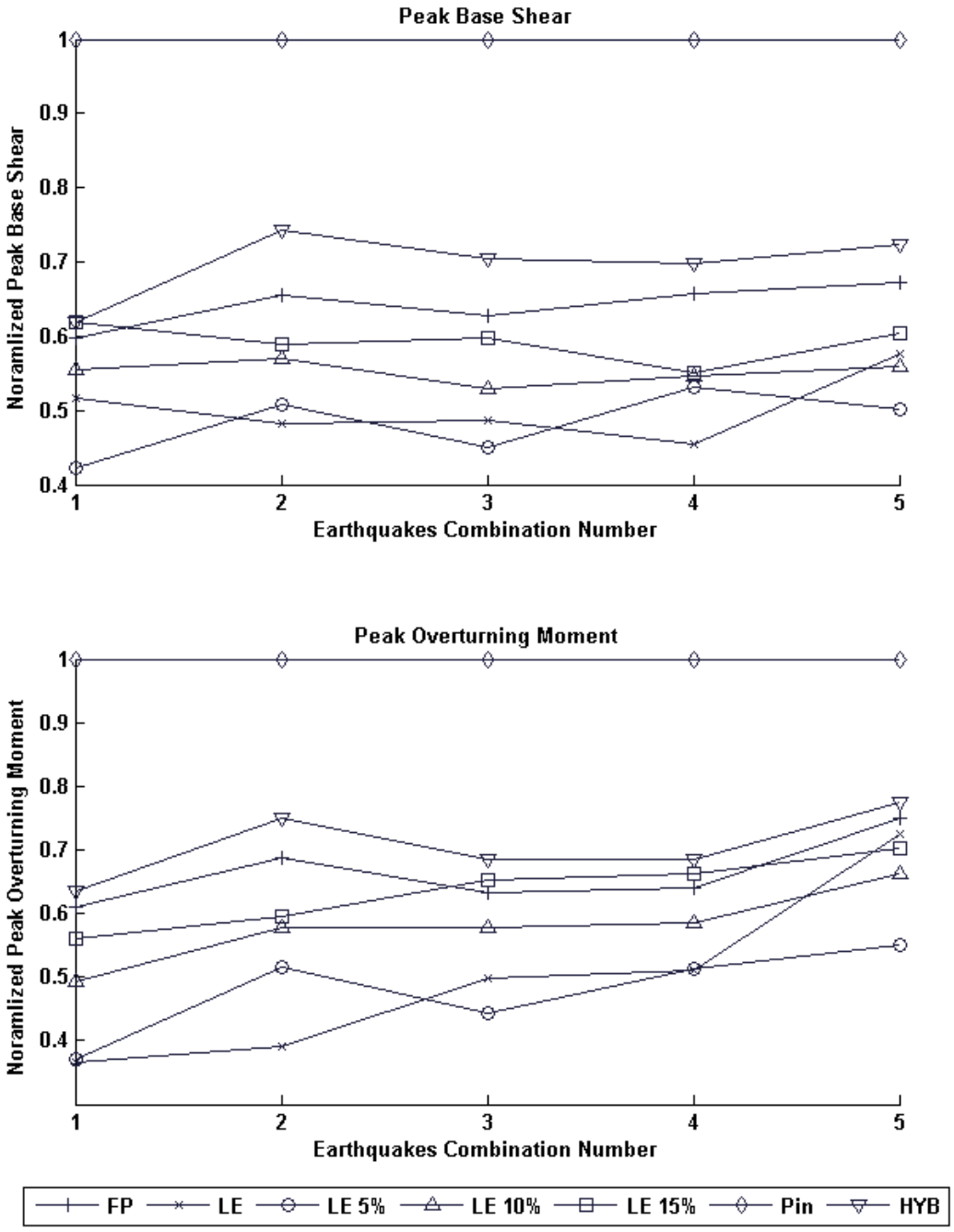

Figure 53. Piers peak base shear and peak overturning moments.

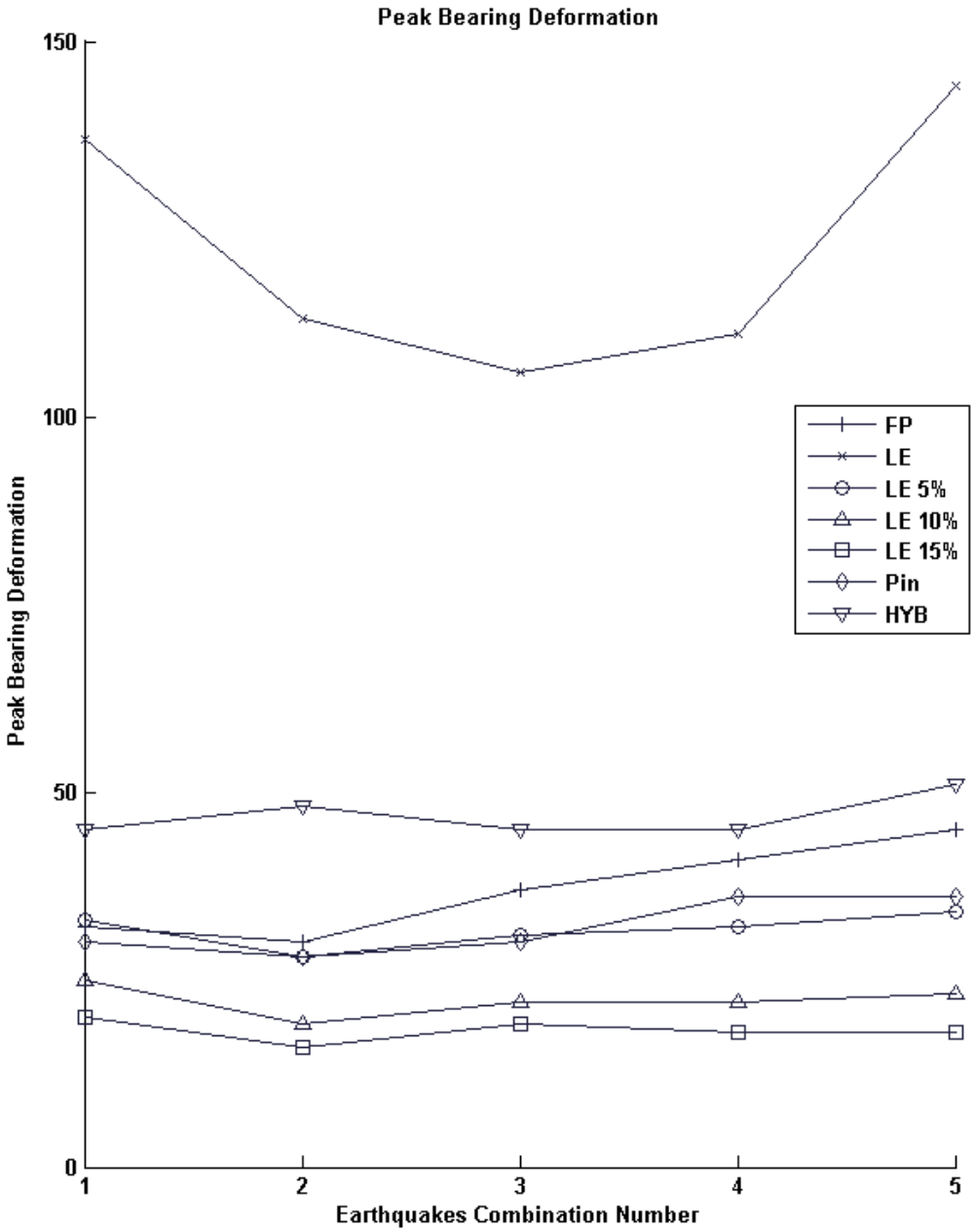

Figure 54. Piers peak bearings deformation.

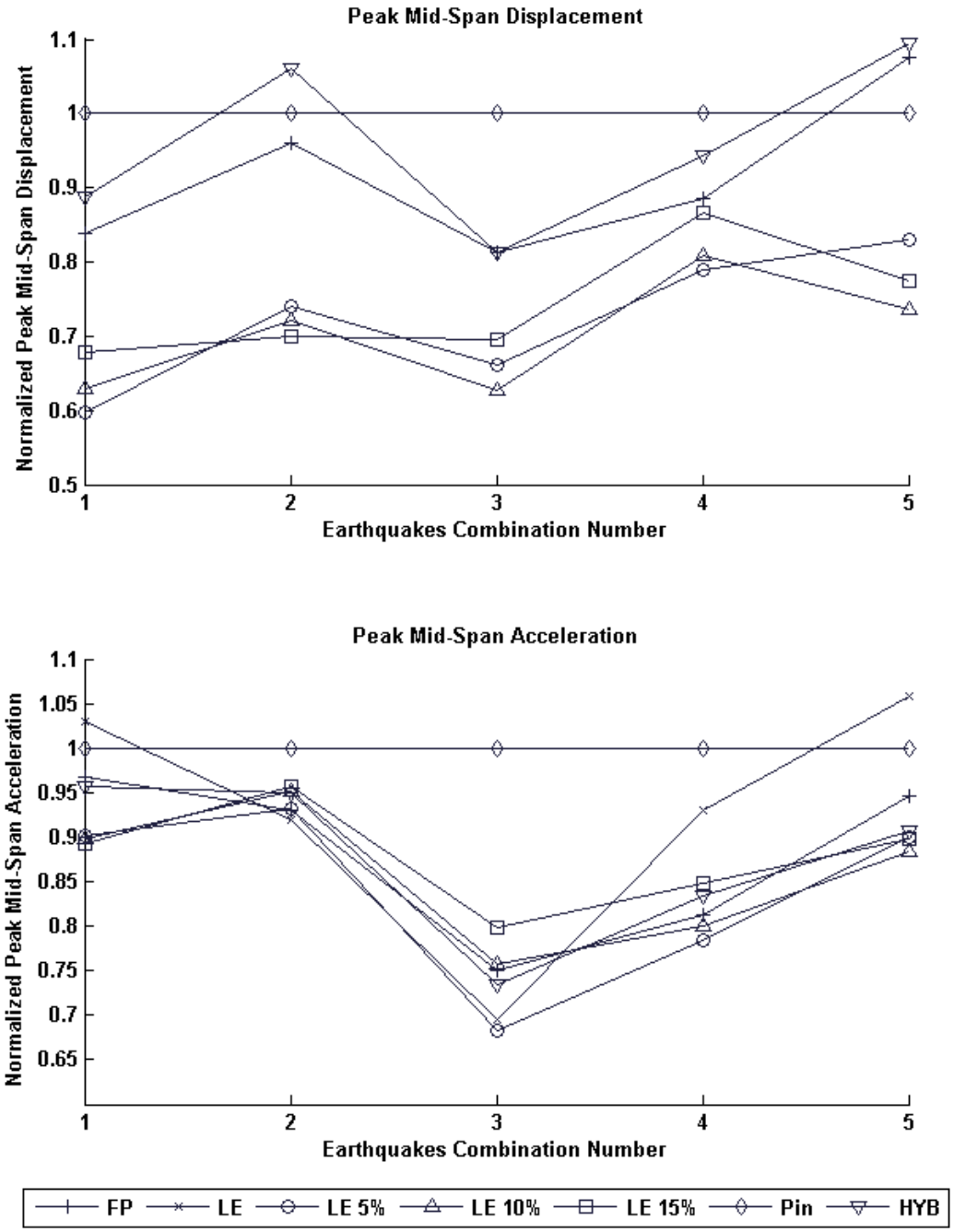

Figure 55.Bridge peak mid-span displacement and acceleration.

5.3 Time History Responses

In this section the time-history response of the mid-span displacement due to earthquake combination 5 is presented. The selection of combination 5 is only representative, and other plots are not included for the sake of brevity.

The figures show the longitudinal and lateral displacements for various test cases. Each figure has six plots, representing all the spans of the bridge.

In the unisolated case the lateral response amplitudes are larger than the longitudinal amplitudes at the intermediate spans (spans 2, 3, 4 and 5) while the longitudinal displacements are larger at the end spans (span 1 and span 6) (see Figure 56). The isolated FP and hybrid cases show similar responses at the intermediate spans; however, at the side spans, the hybrid case lateral response has higher displacement amplitudes compared to the FP case. This due to the presence of the LE bearings in the hybrid case near the side spans of the bridge. The FP and hybrid cases also show a small permanent displacement due to the displaced FP bearings (see Figure 57 and Figure 58).

The isolated LE case show high consistent mid-span displacements at all spans (see Figure 59). The low dissipation of energy in the LE bearings allows the bridge to sway freely reaching an amplitude of 150 mm. Adding damping (viscous dampers) to the LE bearings affected the free vibration of the superstructure and highly reduced the displacement amplitudes (see Figure 60, Figure 61 and Figure 62).

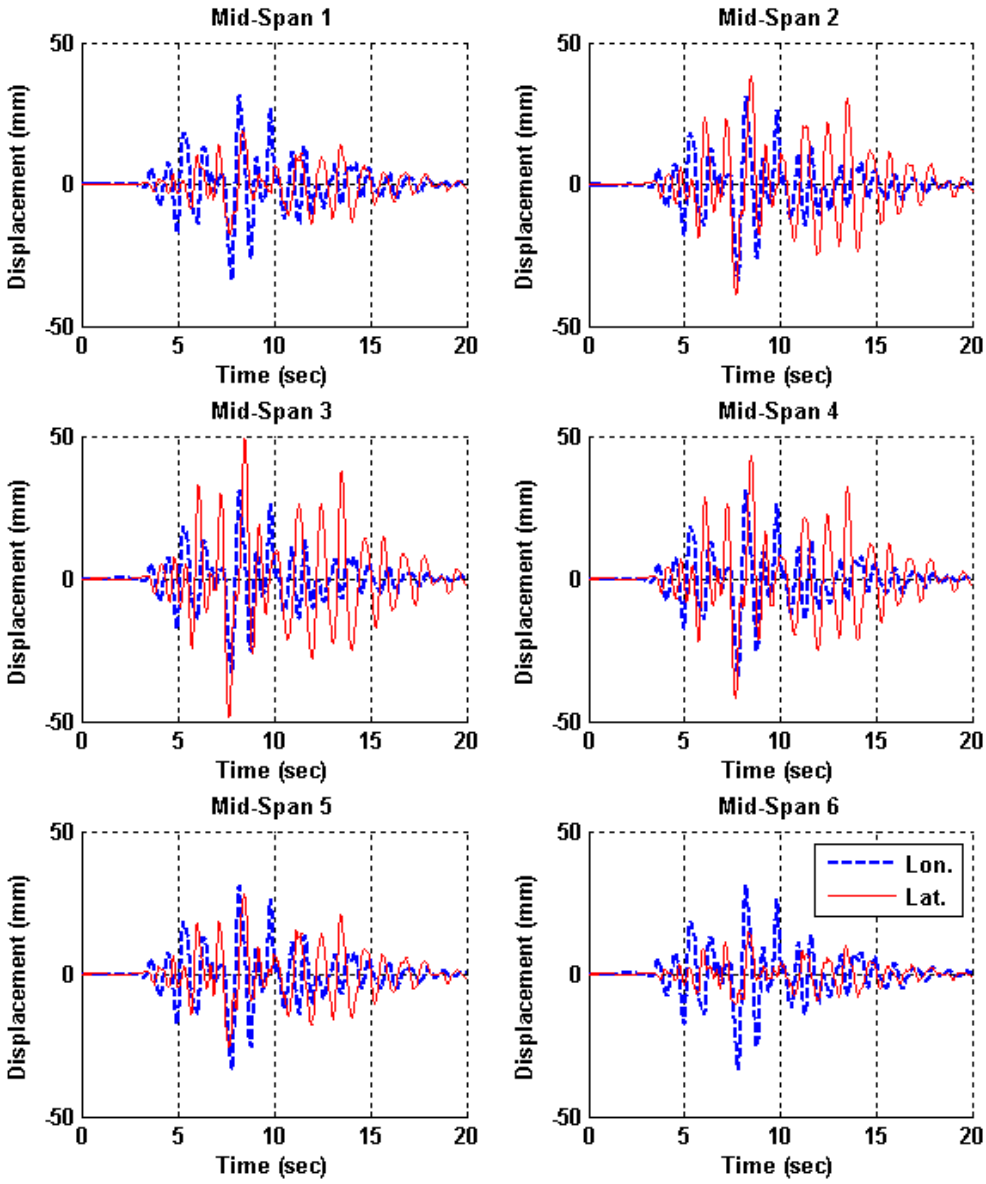

Figure 56. Mid-spans displacement time histories for the base case.

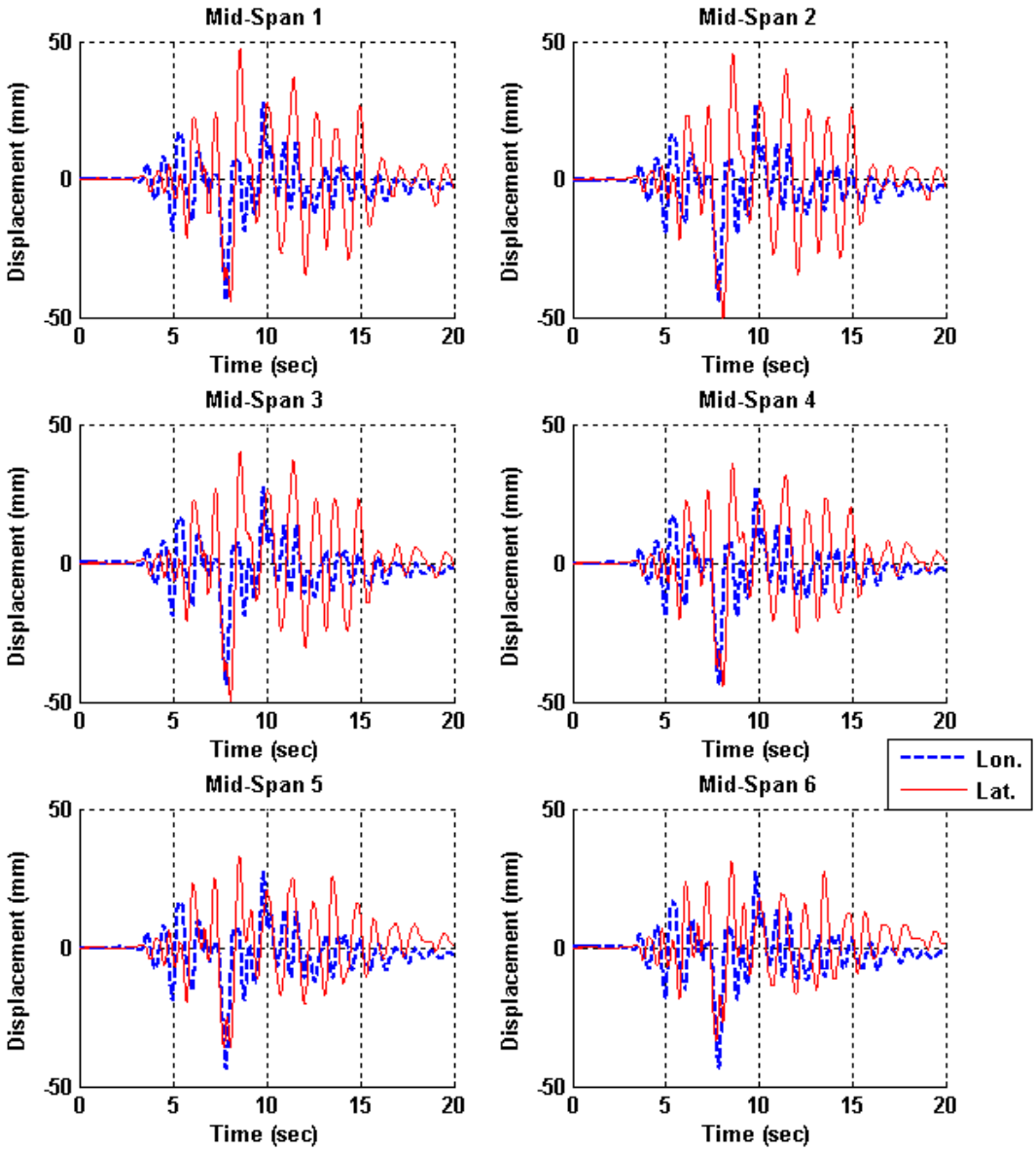

Figure 57. Mid-spans displacement time history for the hybrid case.

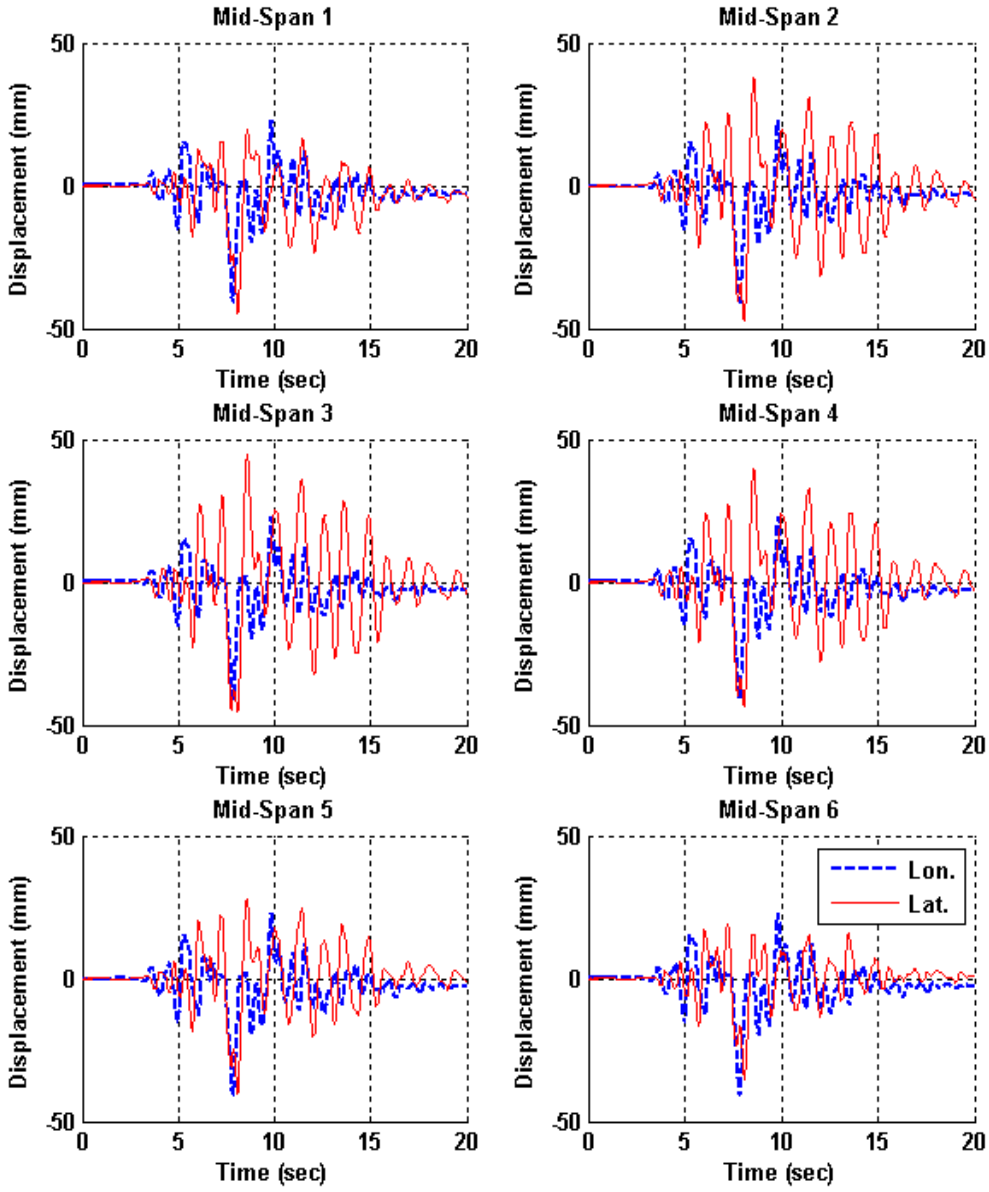

Figure 58. Mid-span displacement time history for the FP case.

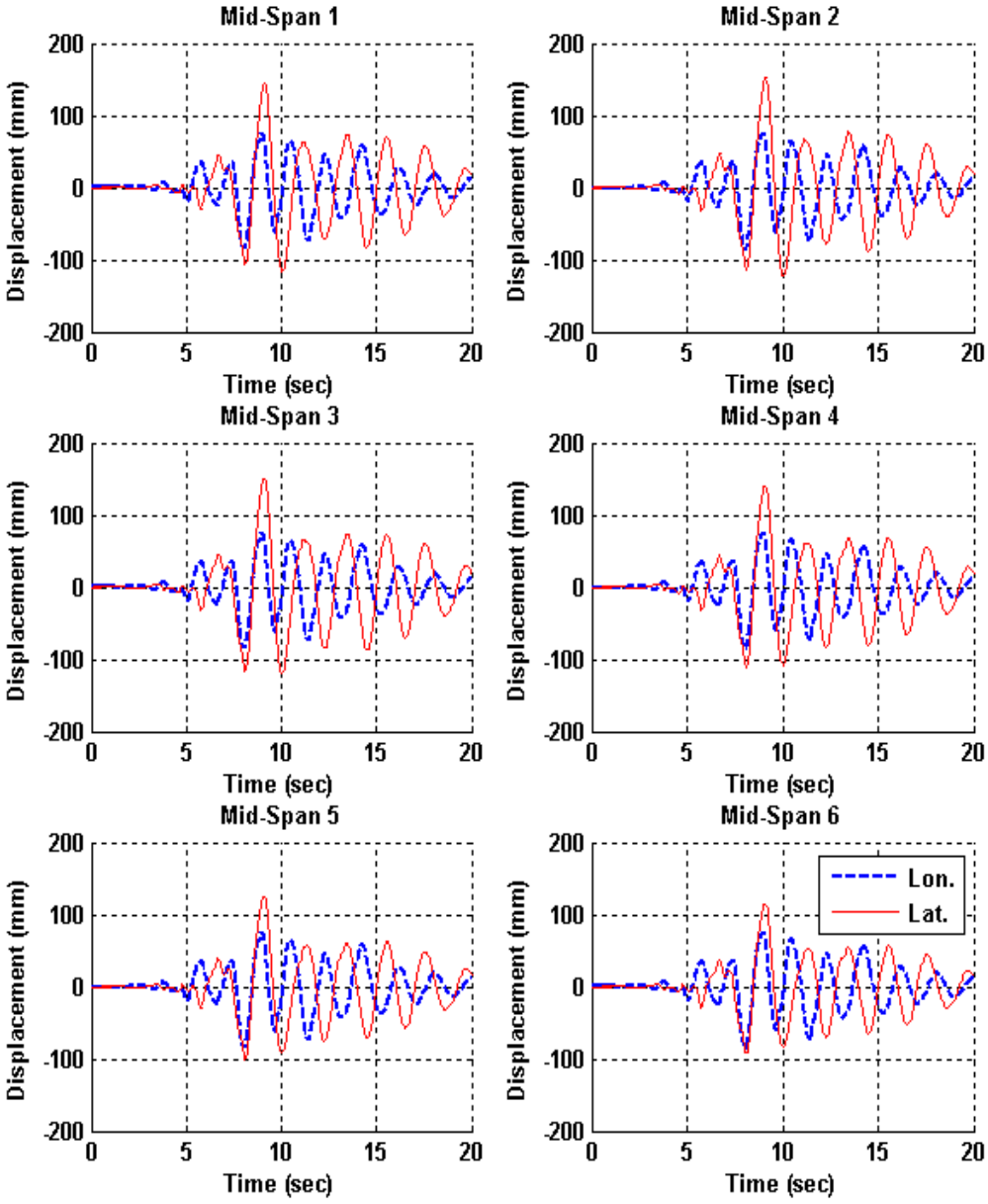

Figure 59. Mid-spans displacement time history for the LE case.

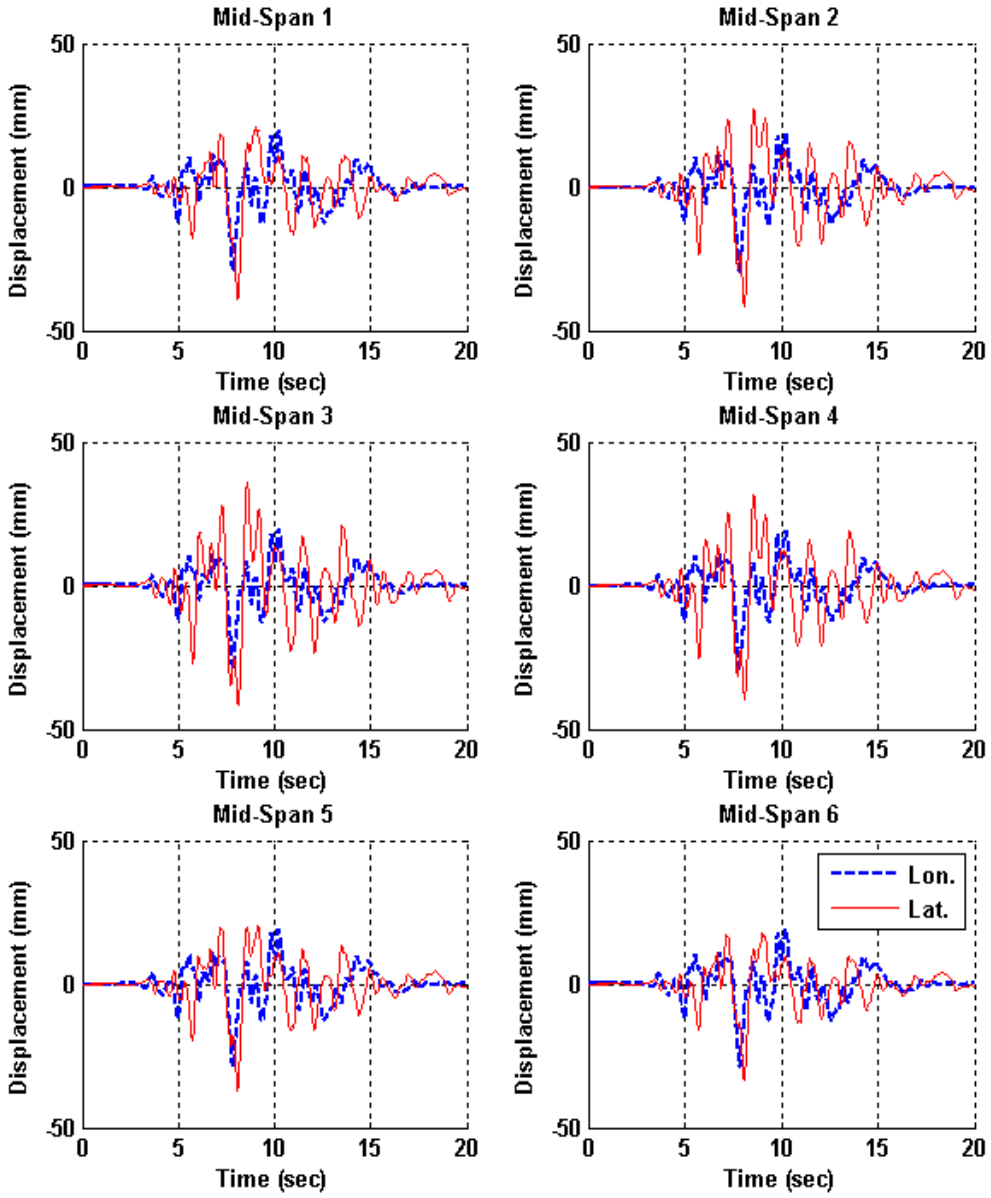

Figure 60. Mid-spans displacement time history for the LE 5% case.

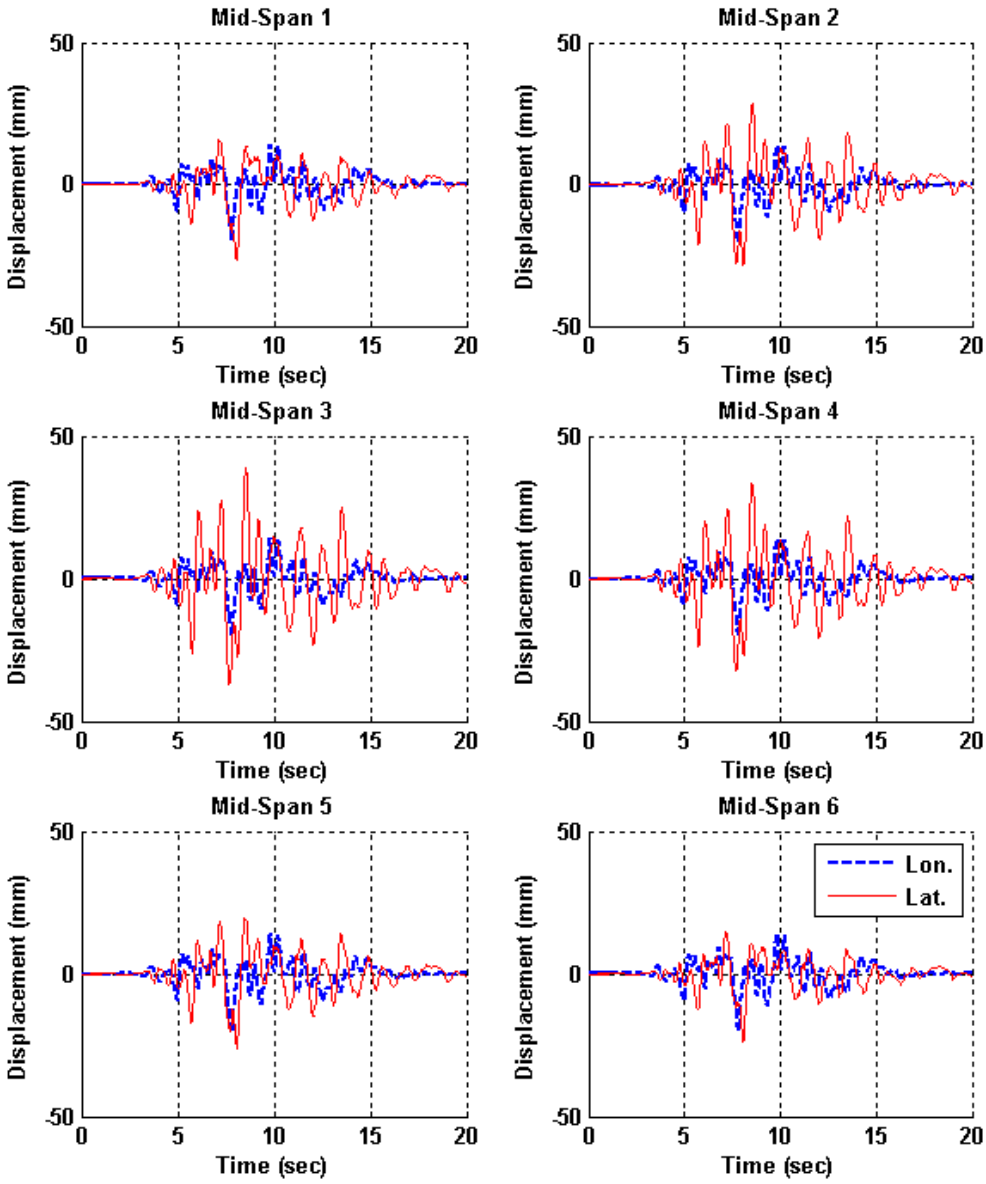

Figure 61. Mid-spans displacement time history for the LE 10% case.

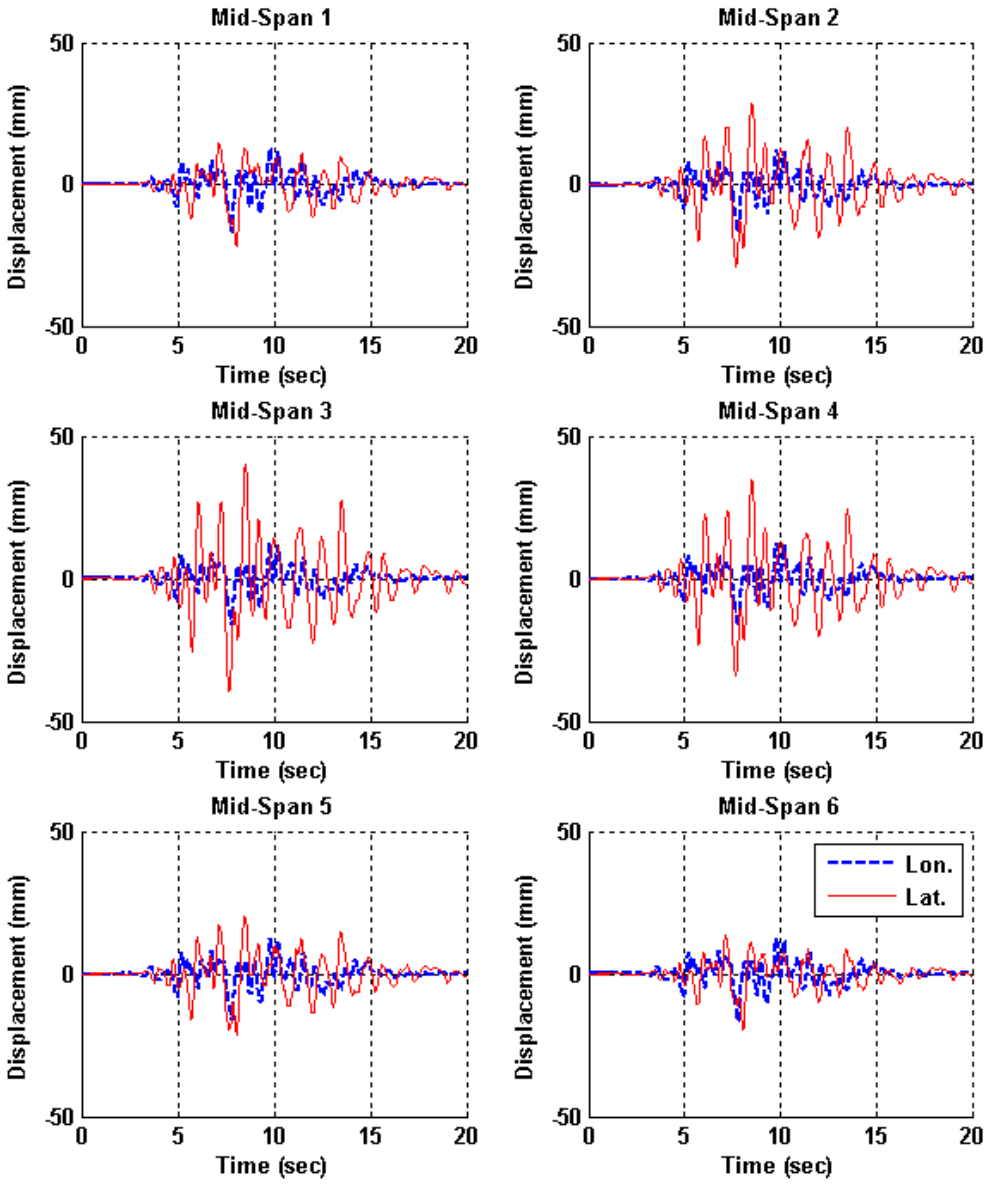

Figure 62. Mid-spans displacement time history for the LE 15% case.

5.4 The effect of Soil-Structure Interaction on the Bridge Response

The tables below (Table 6 through Table 15) show the effect of the soil-structure interaction on the response of the bridge. The columns labeled (1) show the peak values of the performance indices of the model with soil-structure interaction, while the columns labeled (2) are for the model without soil-structure interaction elements. The tables also show the ratio between the peak responses of the SSI model and the model without SSI which are plotted in Figure 63 through Figure 67.

The tables (Table 6 through Table 15) show that the effect of soil-structure interaction is different for different performance variables. For the peak base shear and peak overturning moment generally including the effect of SSI reduces the forces on the substructure of the bridge; however, the reductions in forces strongly vary from one bridge case to another. The pinned case with SSI has PBS and POM at 50% of the values compared to the model without SSI. This means the effect of SSI is significant for the unisolated case. The SSI effect on the PBS and POM of the cases with FP bearings is small and ranges between the ratios 0.86 to 1.2 (see Figure 63 and Figure 64).

The PBS of the LE setups with low damping (LE and LE 5%) is marginally affected by the SSI. On the other hand, the effect of the SSI on the LE setups with higher damping (LE 10% and LE 15%) is higher and reduces both the PBS and the POM of the piers. In other words, the increased capacity (damping coefficient) of the viscous dampers increases the dynamic stiffness of the bridge which in turns causes more soil straining and soil damping.

Surprisingly, the FP and hybrid cases, which relatively had higher piers PBS and POM (see section 5.2), compared to the LE isolated cases, have lower SSI effect. This could be due to the lower loads transferred to the abutments which have higher SSI damping due to the embankments.

The SSI effect on the PBD of the bridge cases with LE bearings is almost negligible especially for the cases with viscous dampers (see Figure 65). However, for the hybrid

case the PBD is magnified by an average of 1.4 in most cases due to the SSI. On the other hand, the PBD of the FP bearings was reduced by 40% due to the SSI when excited by earthquake combination 1; however, for the other earthquake combinations the PBDs were magnified by an average of 30%. The unisolated case, where only longitudinal displacement is allowed at the abutments, shows variable effects due to SSI. At earthquake combination 1 the SSI model had lower PBD, while due to Eq. combination 2 the PBD of the SSI model was almost twice the PBD of the no SSI model. In the same time, for the remaining 3 Eq. combinations the SSI almost had no effect on the PBD

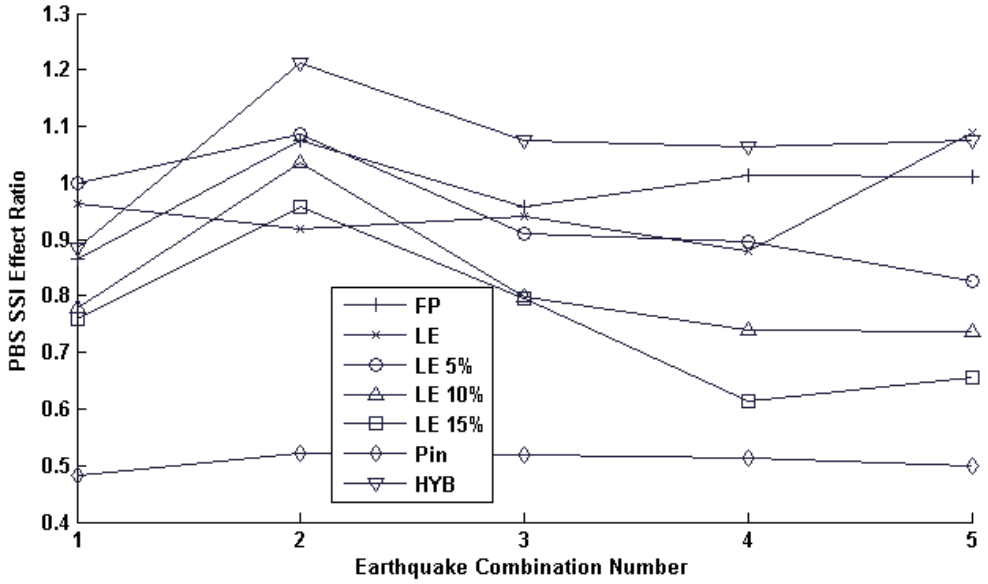

Figure 63. Soil-structure interaction effect on peak base shear

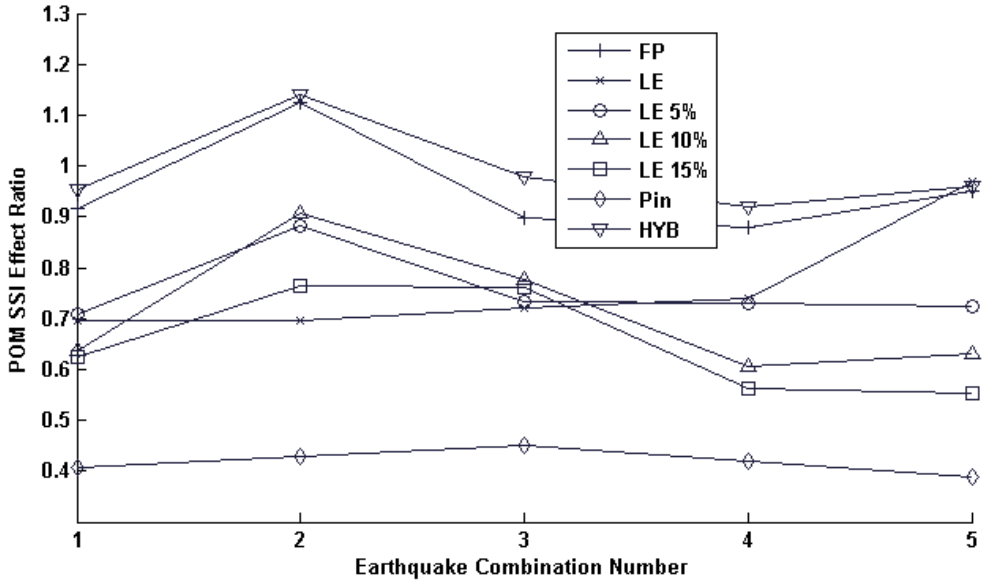

Figure 64. Soil-structure interaction effect on peak overturning moment

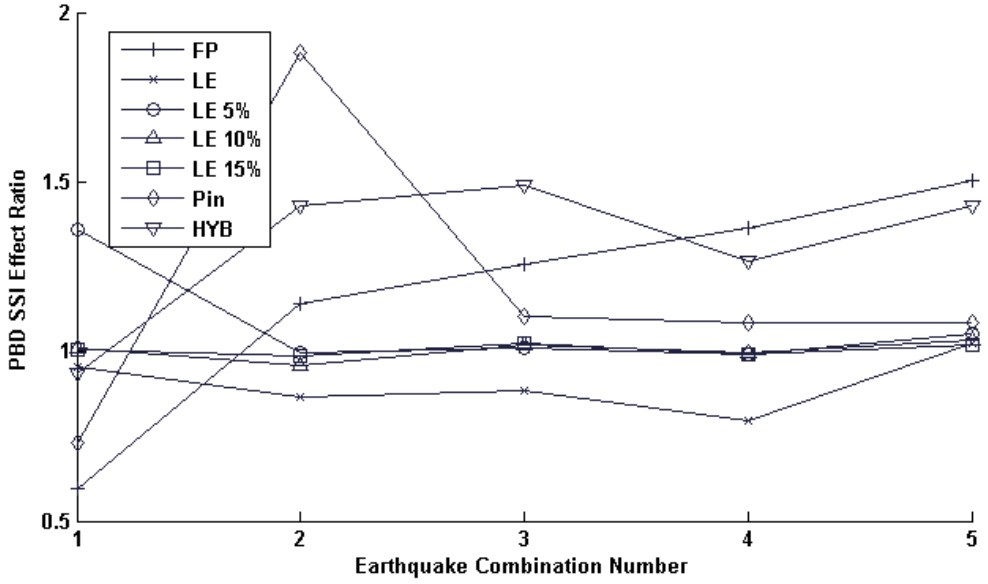

Figure 65. Soil-structure interaction effect on peak bearing deformation

The SSI effect on the PMD is shown in Figure 66. The figure shows that the PMD is much higher in the SSI model compared to the no SSI model. The abundance of considering SSI during seismic analysis of bridges can lead to unpredicted pounding of the bridge deck with the abutments or adjacent structures. The LE case with n viscous dampers was not affected by the soil-structure interaction; however, the implementation of viscous dampers increased the effect of SSI on the PMD. In the LE 15% and LE 10% cases the high PMD ratios is due to the small PMD these cases produce. The slightest increase in PMD due to SSI produces high ratios compared to no SSI case. The LE 5%, FP and hybrid isolated cases show an average SSI ratio effect of 1.6 on the PMD. The unisolated case, again, shows highly variable SSI effect for different earthquakes combinations; nevertheless, the PMD is increased at all earthquake combinations due to the SSI.

The SSI increases the PMA for all isolated cases except for the LE case without viscous dampers (see Figure 67); however, the effect of SSI on the PMA is higher on the LE with viscous dampers compared to the FP and hybrid cases. On the other hand, the PMA of the unisolated case had a reduction of 20% due to the SSI.

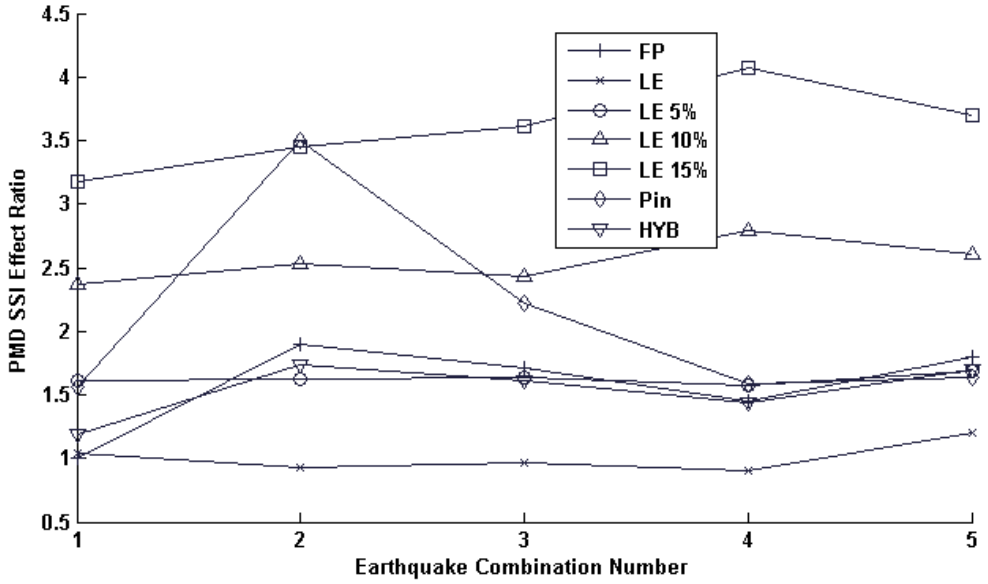

Figure 66. Soil-structure interaction effect on peak mid-span displacement

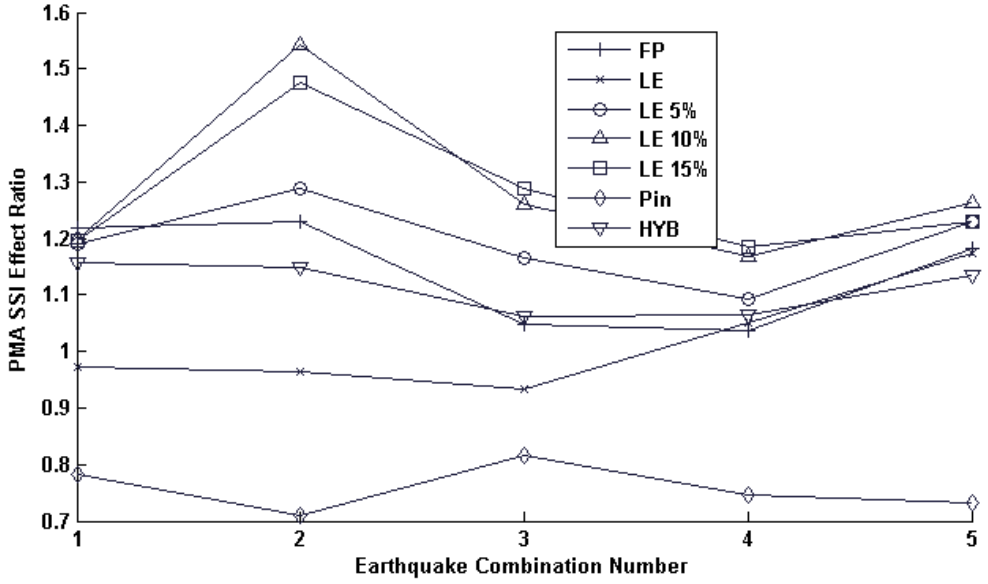

Figure 67. Soil-structure interaction effect on peak mid-span acceleration

Table 6. Comparison between SSI and no-SSI models (PBS, POM, PBD) earthquake combination 1

Performance Indices	Bridge Setup	SSI (1)	w/o SSI (2)	Ratio (1)/(2)
Peak Base Shear(N)	FP Setup	1603174	1852122	0.87
	LE Setup	1383683	1437841	0.96
	LE (5%) Setup	1136700	1138523	1.00
	LE (10%) Setup	1490571	1911886	0.78
	LE (15%) Setup	1663965	2188619	0.76
	Pinned Setup	2685166	5553306	0.48
	Hybrid Setup	1660352	1874954	0.89
Peak Overturning Moment(N.m)	FP Setup	17244500	18811053	0.92
	LE Setup	10320570	14848466	0.70
	LE (5%) Setup	10493295	14837846	0.71
	LE (10%) Setup	13910839	21828811	0.64
	LE (15%) Setup	15871740	25430165	0.62
	Pinned Setup	28279087	69470744	0.41
	Hybrid Setup	17928261	18769261	0.96
Peak Bearing Deformation(m)	FP Setup	0.032	0.053	0.60
	LE Setup	0.137	0.143	0.96
	LE (5%) Setup	0.033	0.024	1.36
	LE (10%) Setup	0.025	0.024	1.01
	LE (15%) Setup	0.020	0.020	1.01
	Pinned Setup	0.030	0.041	0.73
	Hybrid Setup	0.045	0.048	0.94

Table 7. Comparison between SSI and no-SSI models (PMD, PMA) earthquake combination 1

Performance Indices	Bridge Setup	SSI (1)	w/o SSI (2)	Ratio (1)/(2)
Peak Mid-Span Displacement (m)	FP Setup	0.052	0.052	1.00
	LE Setup	0.142	0.137	1.04
	LE (5%) Setup	0.037	0.023	1.61
	LE (10%) Setup	0.039	0.017	2.37
	LE (15%) Setup	0.042	0.013	3.18
	Pinned Setup	0.062	0.040	1.56
	Hybrid Setup	0.055	0.046	1.19
Peak Mid-Span Acceleration (m/sec^2)	FP Setup	4.61	3.78	1.22
	LE Setup	4.91	5.05	0.97
	LE (5%) Setup	4.30	3.61	1.19
	LE (10%) Setup	4.29	3.57	1.20
	LE (15%) Setup	4.26	3.56	1.20
	Pinned Setup	4.77	6.10	0.78
	Hybrid Setup	4.57	3.95	1.16

Table 8. Comparison between SSI and no-SSI models (PBS, POM, PBD) earthquake combination 2

Performance Indices	Bridge Setup	SSI (1)	w/o SSI (2)	Ratio (1)/(2)
Peak Base Shear(N)	FP Setup	1508313	1401960	1.08
	LE Setup	1110626	1210720	0.92
	LE (5%) Setup	1167611	1073789	1.09
	LE (10%) Setup	1308326	1264716	1.03
	LE (15%) Setup	1354564	1413998	0.96
	Pinned Setup	2300347	4403007	0.52
	Hybrid Setup	1706941	1407705	1.21
Peak Overturning Moment(N.m)	FP Setup	16463931	14649231	1.12
	LE Setup	9396441	13492617	0.70
	LE (5%) Setup	12384362	14027931	0.88
	LE (10%) Setup	13824983	15240410	0.91
	LE (15%) Setup	14281453	18660892	0.77
	Pinned Setup	23961683	55760306	0.43
	Hybrid Setup	17992589	15778825	1.14
Peak Bearing Deformation(m)	FP Setup	0.030	0.027	1.14
	LE Setup	0.113	0.131	0.87
	LE (5%) Setup	0.028	0.028	1.00
	LE (10%) Setup	0.019	0.019	0.96
	LE (15%) Setup	0.016	0.016	0.99
	Pinned Setup	0.028	0.015	1.88
	Hybrid Setup	0.048	0.033	1.43

Table 9. Comparison between SSI and no-SSI models (PMD, PMA) earthquake combination 2

Performance Indices	Bridge Setup	SSI (1)	w/o SSI (2)	Ratio (1)/(2)
Peak Mid-Span Displacement (m)	FP Setup	0.048	0.025	1.90
	LE Setup	0.116	0.125	0.93
	LE (5%) Setup	0.037	0.023	1.63
	LE (10%) Setup	0.036	0.014	2.53
	LE (15%) Setup	0.035	0.010	3.45
	Pinned Setup	0.050	0.014	3.51
	Hybrid Setup	0.053	0.030	1.73
Peak Mid-Span Acceleration (m/sec^2)	FP Setup	3.41	2.77	1.23
	LE Setup	3.37	3.50	0.96
	LE (5%) Setup	3.42	2.65	1.29
	LE (10%) Setup	3.49	2.26	1.54
	LE (15%) Setup	3.51	2.38	1.47
	Pinned Setup	3.67	5.16	0.71
	Hybrid Setup	3.48	3.03	1.15

Table 10. Comparison between SSI and no-SSI models (PBS, POM, PBD) earthquake combination 3

Performance Indices	Bridge Setup	SSI (1)	w/o SSI (2)	Ratio (1)/(2)
Peak Base Shear(N)	FP Setup	1400634	1463568	0.96
	LE Setup	1084384	1154004	0.94
	LE (5%) Setup	1003778	1102687	0.91
	LE (10%) Setup	1181236	1480802	0.80
	LE (15%) Setup	1335493	1681384	0.79
	Pinned Setup	2230988	4305731	0.52
	Hybrid Setup	1571154	1462013	1.07
Peak Overturning Moment(N.m)	FP Setup	15419948	17195734	0.90
	LE Setup	12113858	16771264	0.72
	LE (5%) Setup	10810659	14735949	0.73
	LE (10%) Setup	14110568	18203307	0.78
	LE (15%) Setup	15923037	20918703	0.76
	Pinned Setup	24370575	54057745	0.45
	Hybrid Setup	16704283	17061964	0.98
Peak Bearing Deformation(m)	FP Setup	0.037	0.030	1.25
	LE Setup	0.106	0.120	0.88
	LE (5%) Setup	0.031	0.031	1.01
	LE (10%) Setup	0.022	0.022	1.02
	LE (15%) Setup	0.019	0.018	1.03
	Pinned Setup	0.030	0.027	1.10
	Hybrid Setup	0.045	0.030	1.49

Table 11. Comparison between SSI and no-SSI models (PMD, PMA) earthquake combination 3

Performance Indices	Bridge Setup	SSI (1)	w/o SSI (2)	Ratio (1)/(2)
Peak Mid-Span Displacement (m)	FP Setup	0.048	0.028	1.71
	LE Setup	0.116	0.120	0.96
	LE (5%) Setup	0.039	0.024	1.64
	LE (10%) Setup	0.037	0.015	2.43
	LE (15%) Setup	0.041	0.011	3.61
	Pinned Setup	0.059	0.026	2.22
	Hybrid Setup	0.048	0.029	1.62
Peak Mid-Span Acceleration (m/sec^2)	FP Setup	3.14	3.00	1.05
	LE Setup	2.91	3.11	0.93
	LE (5%) Setup	2.86	2.45	1.17
	LE (10%) Setup	3.17	2.52	1.26
	LE (15%) Setup	3.34	2.60	1.29
	Pinned Setup	4.18	5.13	0.82
	Hybrid Setup	3.07	2.90	1.06

Table 12. Comparison between SSI and no-SSI models (PBS, POM, PBD) earthquake combination 4

Performance Indices	Bridge Setup	SSI (1)	w/o SSI (2)	Ratio (1)/(2)
Peak Base Shear(N)	FP Setup	1612464	1591203	1.01
	LE Setup	1114082	1265731	0.88
	LE (5%) Setup	1303241	1452394	0.90
	LE (10%) Setup	1344121	1816679	0.74
	LE (15%) Setup	1351232	2204847	0.61
	Pinned Setup	2455547	4785585	0.51
	Hybrid Setup	1711932	1610146	1.06
Peak Overturning Moment(N.m)	FP Setup	15318064	17396643	0.88
	LE Setup	12199181	16493486	0.74
	LE (5%) Setup	12263910	16799889	0.73
	LE (10%) Setup	14026981	23161354	0.61
	LE (15%) Setup	15829507	28112640	0.56
	Pinned Setup	23928962	57051812	0.42
	Hybrid Setup	16358858	17811000	0.92
Peak Bearing Deformation(m)	FP Setup	0.041	0.030	1.36
	LE Setup	0.111	0.140	0.79
	LE (5%) Setup	0.032	0.032	0.99
	LE (10%) Setup	0.022	0.022	1.00
	LE (15%) Setup	0.018	0.018	0.99
	Pinned Setup	0.036	0.033	1.09
	Hybrid Setup	0.045	0.036	1.26

Table 13. Comparison between SSI and no-SSI models (PMD, PMA) earthquake combination 4

Performance Indices	Bridge Setup	SSI (1)	w/o SSI (2)	Ratio (1)/(2)
Peak Mid-Span Displacement (m)	FP Setup	0.046	0.031	1.45
	LE Setup	0.125	0.139	0.90
	LE (5%) Setup	0.041	0.026	1.58
	LE (10%) Setup	0.042	0.015	2.80
	LE (15%) Setup	0.045	0.011	4.07
	Pinned Setup	0.052	0.032	1.59
	Hybrid Setup	0.049	0.034	1.44
Peak Mid-Span Acceleration (m/sec^2)	FP Setup	3.24	3.12	1.04
	LE Setup	3.71	3.53	1.05
	LE (5%) Setup	3.12	2.86	1.09
	LE (10%) Setup	3.19	2.73	1.17
	LE (15%) Setup	3.38	2.85	1.19
	Pinned Setup	3.99	5.34	0.75
	Hybrid Setup	3.32	3.12	1.07

Table 14. Comparison between SSI and no-SSI models (PBS, POM, PBD) earthquake combination 5

Performance Indices	Bridge Setup	SSI (1)	w/o SSI (2)	Ratio (1)/(2)
Peak Base Shear(N)	FP Setup	1609216	1591203	1.01
	LE Setup	1377955	1265731	1.09
	LE (5%) Setup	1200781	1452394	0.83
	LE (10%) Setup	1340884	1816679	0.74
	LE (15%) Setup	1447088	2204847	0.66
	Pinned Setup	2395640	4785585	0.50
	Hybrid Setup	1731540	1610146	1.08
Peak Overturning Moment(N.m)	FP Setup	16548881	17396643	0.95
	LE Setup	16011208	16493486	0.97
	LE (5%) Setup	12164323	16799889	0.72
	LE (10%) Setup	14639827	23161354	0.63
	LE (15%) Setup	15513959	28112640	0.55
	Pinned Setup	22090006	57051812	0.39
	Hybrid Setup	17116392	17811000	0.96
Peak Bearing Deformation(m)	FP Setup	0.045	0.030	1.50
	LE Setup	0.144	0.140	1.03
	LE (5%) Setup	0.034	0.032	1.05
	LE (10%) Setup	0.023	0.022	1.03
	LE (15%) Setup	0.018	0.018	1.02
	Pinned Setup	0.036	0.033	1.08
	Hybrid Setup	0.051	0.036	1.43

Table 15. Comparison between SSI and no-SSI models (PMD, PMA) earthquake combination 5

Performance Indices	Bridge Setup	SSI (1)	w/o SSI (2)	Ratio (1)/(2)
Peak Mid-Span Displacement (m)	FP Setup	0.057	0.031	1.80
	LE Setup	0.167	0.139	1.20
	LE (5%) Setup	0.044	0.026	1.69
	LE (10%) Setup	0.039	0.015	2.60
	LE (15%) Setup	0.041	0.011	3.70
	Pinned Setup	0.053	0.032	1.64
	Hybrid Setup	0.058	0.034	1.69
Peak Mid-Span Acceleration (m/sec^2)	FP Setup	3.69	3.12	1.18
	LE Setup	4.14	3.53	1.17
	LE (5%) Setup	3.52	2.86	1.23
	LE (10%) Setup	3.45	2.73	1.26
	LE (15%) Setup	3.51	2.85	1.23
	Pinned Setup	3.91	5.34	0.73
	Hybrid Setup	3.54	3.12	1.14

5.5 Forces in the Viscous Dampers

Table 16 and Table 17 show the peak relative velocities of the viscous dampers in both directions, lateral and longitudinal, for each case and each earthquake combination. Additionally, the peak forces of the viscous dampers are also shown. Increasing the damping coefficients reduce the peak velocities of the bridge; however, this is accompanied by an increase in the peak forces of the dampers. By comparing the peak forces of the bridge viscous dampers to commercial viscous dampers tables (Taylor devices Inc.), the peak forces in the 5% dampers are closer to the smallest dampers available. It would be more economical to use larger dampers and reducing the number of dampers at each pier.

The longitudinal direction shows higher velocity components compared to the lateral direction; however, the tables show that the highest peak velocities mostly occur at the bridge abutments. Moreover, the peak velocities at the mid piers (pier 2, 3 and 4) had high lateral peck velocity components while the end piers (pier 1 and 5) had low later peak velocities. On the other hand, the longitudinal peak velocities had almost equal velocities at the abutments and also very close similar peak velocities at the piers.

The characteristics of the earthquakes combination strongly affect the peak velocities of the viscous dampers; however, for each earthquake combination the effect of increasing the dampers capacity (damping coefficient) always reduces the peak velocities. The reduction in peak velocities is large when increasing the critical damping ratio from 5% (LE 5% case) to 10 % (LE 10% case); furthermore, any further increase in the critical damping ratio only have marginal effect on the peak velocities. In other words, using viscous dampers with very high capacities could transfer undesirable large loads to the substructure.

Table 16. Viscous dampers peak velocities(m/sec) and peak forces(KN) for earthquake combinations 1, 2 and 3

Earthquake Combination	Bridge Setup	Direction	West Abutment	Pier 1	Pier 2	Pier 3	Pier 4	Pier 5	East Abutment	Peak Velocity	Peak Force (KN)
C1	LE 5%	Longitudinal	0.136	0.112	0.109	0.107	0.107	0.112	0.135	0.136	2.553E+02
		Lateral	0.092	0.069	0.092	0.092	0.076	0.057	0.080	0.092	1.732E+02
	LE 10%	Longitudinal	0.106	0.072	0.070	0.067	0.068	0.073	0.104	0.106	3.973E+02
		Lateral	0.069	0.041	0.064	0.062	0.052	0.035	0.057	0.069	2.569E+02
	LE 15%	Longitudinal	0.086	0.054	0.052	0.049	0.050	0.055	0.085	0.086	4.819E+02
		Lateral	0.054	0.031	0.049	0.048	0.039	0.025	0.044	0.054	3.054E+02
C2	LE 5%	Longitudinal	0.105	0.093	0.091	0.090	0.090	0.093	0.104	0.105	1.958E+02
		Lateral	0.101	0.074	0.098	0.096	0.084	0.066	0.088	0.101	1.887E+02
	LE 10%	Longitudinal	0.067	0.054	0.053	0.051	0.052	0.054	0.067	0.067	2.507E+02
		Lateral	0.064	0.039	0.057	0.056	0.048	0.034	0.056	0.064	2.413E+02
	LE 15%	Longitudinal	0.050	0.038	0.037	0.036	0.036	0.038	0.050	0.050	2.823E+02
		Lateral	0.050	0.027	0.042	0.041	0.034	0.023	0.043	0.050	2.821E+02
C3	LE 5%	Longitudinal	0.112	0.097	0.096	0.094	0.095	0.098	0.111	0.112	2.093E+02
		Lateral	0.104	0.075	0.092	0.091	0.077	0.064	0.087	0.104	1.952E+02
	LE 10%	Longitudinal	0.069	0.055	0.053	0.052	0.053	0.055	0.069	0.069	2.595E+02
		Lateral	0.068	0.042	0.063	0.062	0.051	0.035	0.059	0.068	2.545E+02
	LE 15%	Longitudinal	0.055	0.039	0.037	0.036	0.036	0.038	0.054	0.055	3.102E+02
		Lateral	0.052	0.029	0.049	0.048	0.038	0.024	0.045	0.052	2.900E+02

Table 17. Viscous dampers peak velocities(m/sec) and peak forces(KN) for earthquake combinations 4 and 5

Earthquake Combination	Bridge Setup	Direction	West Abutment	Pier 1	Pier 2	Pier 3	Pier 4	Pier 5	East Abutment	Peak Velocity	Peak Force (KN)
C4	LE 5%	Longitudinal	0.113	0.100	0.099	0.096	0.097	0.100	0.113	0.113	2.118E+02
		Lateral	0.104	0.074	0.091	0.091	0.079	0.068	0.093	0.104	1.942E+02
	LE 10%	Longitudinal	0.071	0.058	0.057	0.055	0.055	0.057	0.070	0.071	2.658E+02
		Lateral	0.062	0.038	0.064	0.064	0.051	0.034	0.057	0.064	2.403E+02
	LE 15%	Longitudinal	0.054	0.040	0.039	0.037	0.038	0.040	0.053	0.054	3.025E+02
		Lateral	0.047	0.028	0.049	0.049	0.038	0.023	0.042	0.049	2.765E+02
C5	LE 5%	Longitudinal	0.113	0.100	0.099	0.096	0.097	0.100	0.113	0.113	2.117E+02
		Lateral	0.112	0.086	0.121	0.119	0.100	0.075	0.104	0.121	2.259E+02
	LE 10%	Longitudinal	0.071	0.058	0.057	0.055	0.055	0.058	0.070	0.071	2.659E+02
		Lateral	0.073	0.044	0.071	0.070	0.057	0.038	0.067	0.073	2.728E+02
	LE 15%	Longitudinal	0.054	0.040	0.039	0.037	0.038	0.040	0.053	0.054	3.028E+02
		Lateral	0.054	0.029	0.050	0.049	0.040	0.024	0.050	0.054	3.024E+02

5.6 Non-Linear Fluid Viscous Dampers

This section discusses the effect of having non-linear fluid viscous dampers where

$$F = C \times sgn(V) \times |V|^{\alpha} \qquad \alpha \neq 1 \qquad 5.1)$$

where F is the damper force, C is the damper damping coefficient and V is the relative velocity of the two damper ends.

In the previous sections linear dampers were used. In many practical applications, it is desirable to have non-linear dampers. Dampers with values of $\alpha > 1$ reach the damper peak at lower velocities compared to the linear case (see Figure 68). This can prevent the bridge superstructure from falling off the piers (unseating) in extreme cases. In addition to this, non-linear dampers can also protect structures from pounding to adjacent structures. However, higher $\alpha's$ may result into transferring higher forces to the substructure during extreme seismic events. On the other hand, dampers with values of $\alpha < 1$ reach the damper peak force at higher velocities than those of the linear case and the $\alpha > 1$ case (see Figure 68). This allows for higher displacement amplitudes which, consequently, results in higher energy dissipation during extreme seismic events, and less force transferred to the substructure.

Figure 68 shows the force-velocity relationships of the three compared cases. The linear viscous damper ($\alpha = 1$) shown correspond to the isolated case LE 5%. The bridge performance indices of the three alpha cases are calculated and compared in figures 69 through 73. Figure 69 compares the peak base shear of the three aforementioned cases. In general, $\alpha < 1$ resulted into slightly lower forces transferred to the substructure compared to the $\alpha > 1$ case. However, for the peak overturning moment no clear relation can be found between the two non-linear damping cases (see Figure 70). Nevertheless, the non-linear cases had similar values compared to the linear case.

The $\alpha < 1$ gives lower peak bearing deformation compared to the $\alpha > 1$ case while the linear case had lower PBD compared to the $\alpha > 1$ case and higher PBD compared to the

$\alpha < 1$ case (see Figure 71). The $\alpha > 1$ case gave similar peak mid-span displacement pattern of the PBD where the PMD increased by 10% in most cases compared to the linear case (see Figure 72). However, the peak mid-span acceleration of the non-linear damping cases didn't have a clear pattern compared to the linear damping case (see Figure 73). The PMA of the non-linear damping cases varied between ±6% of the linear damping PMA case.

Figure 74 shows the peak velocities of the dampers for different α cases. $\alpha > 1$ case shows lower damper velocities compared to the other two cases. In the same time, $\alpha < 1$ case shows larger velocities due to the relatively smaller forces exerted at high velocities.

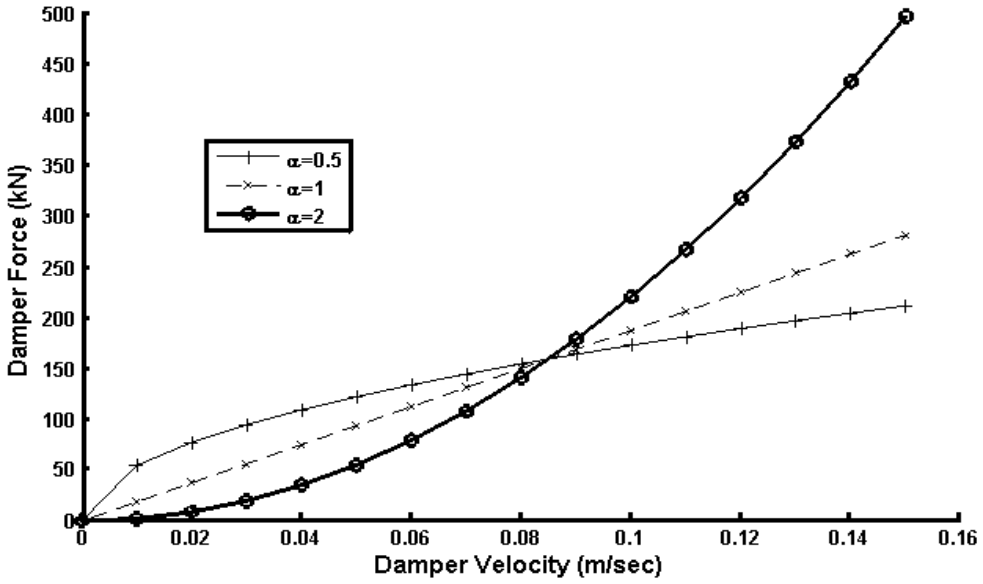

Figure 68. Fluid Viscous dampers force-velocity relationships.

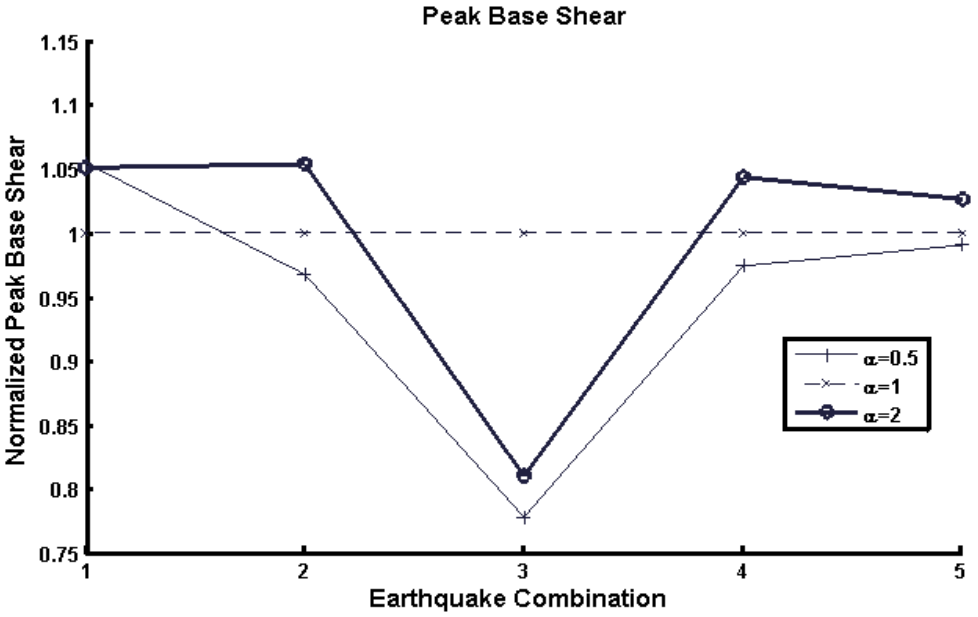

Figure 69. Comparison of the bridge peak base shear on the structure due to different values of α.

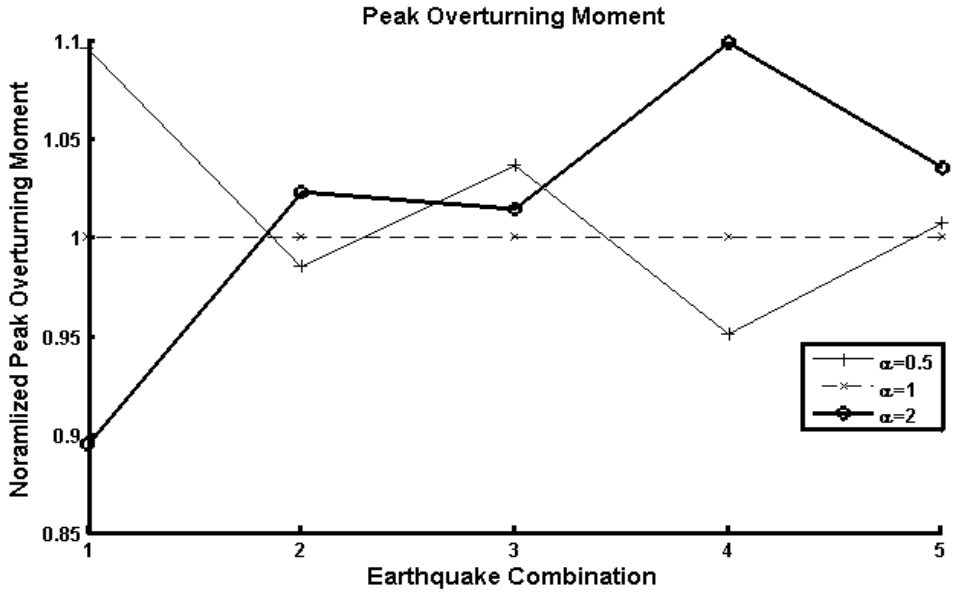

Figure 70. Comparison of the bridge peak overturning moment on the structure due to different values of α.

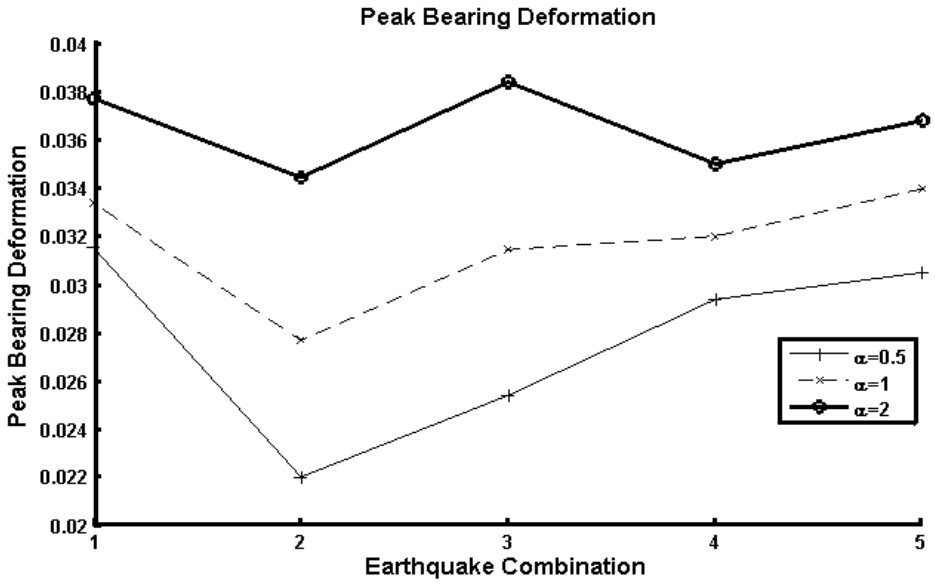

Figure 71. Comparison of the bridge peak bearing deformation on the structure due to different values of α.

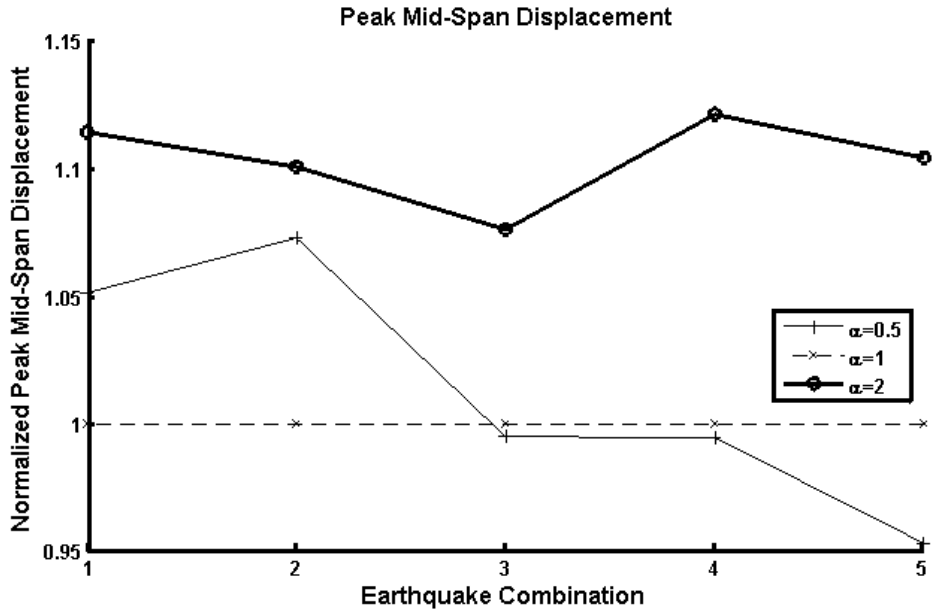

Figure 72. Comparison of the bridge peak mid-span displacement on the structure due to different values of α.

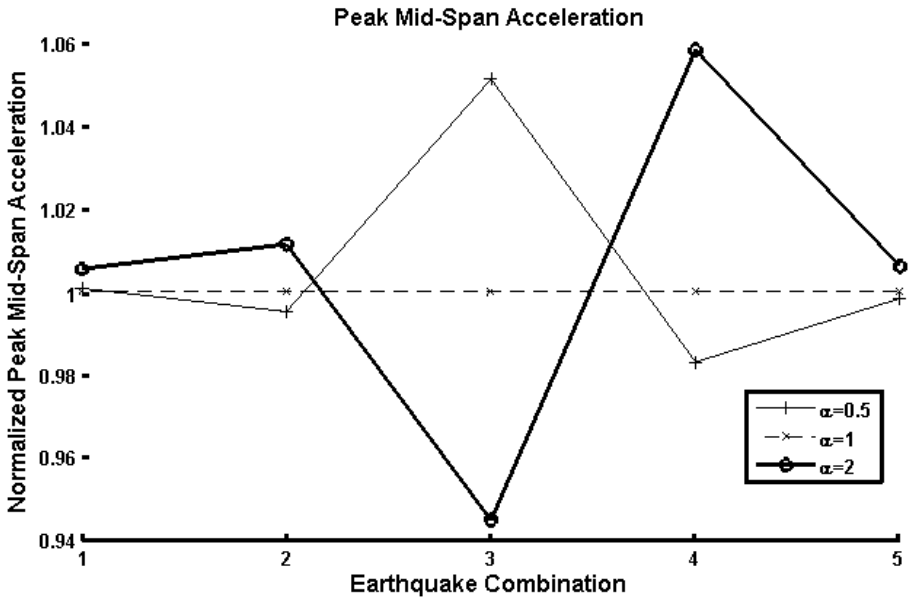

Figure 73. Comparison of the bridge peak mid-span acceleration on the structure due to different values of α.

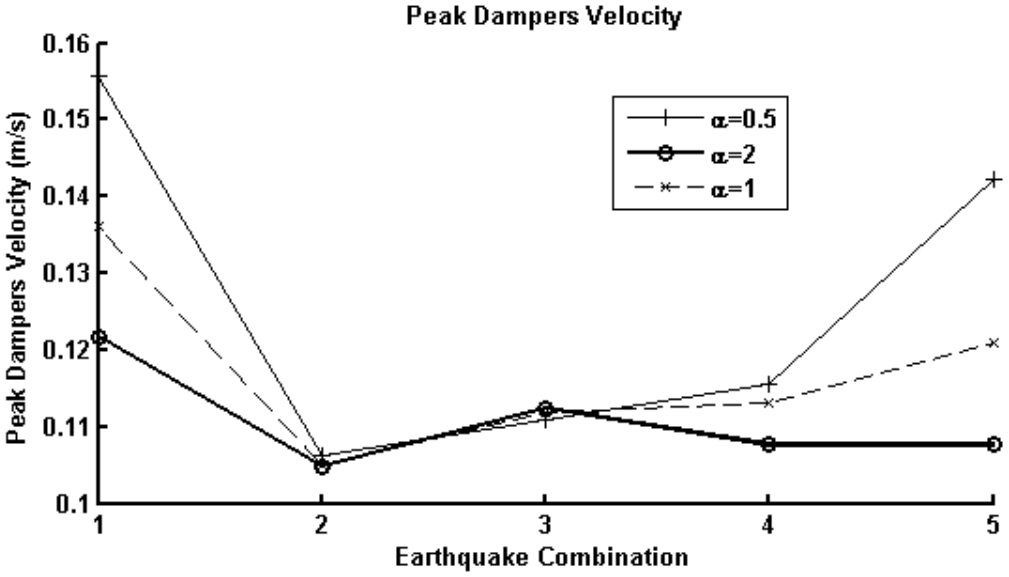

Figure 74. Comparison of the bridge peak dampers velocity due to different values of α.

5.7 Columns Stress-Strain Hysteresis Loops

In this section, stress-strain hysteric loops of the bridge column fibres are presented. Pier 2 was selected for this representation, where pier 2 supports the highest dead load (see Figure 8). The element selected is the top element of the right column (see Figure 11). Two perpendicular fibres in different directions are chosen. The first fibre is at the outer layer (extreme fibre) of the column in the longitudinal direction while the second fibre is the extreme fibre in the lateral direction (see Figure 12). Three bridge cases are compared: Unisolated case (pinned), hybrid isolated case and elastomeric bearings with 5% critical damping viscous dampers isolated case.

Figure 75 shows the stress-train relationship of the three bridge cases of the fibre in the longitudinal direction. The positive numbers in the figure are compressive stress (y-axis) and compressive strain (x-axis). The plots show higher strains occurring in the pinned case compared to the two hybrid case and the LE5% case. The pinned case also shows that cracking of the concrete occurs due to excessive tensile strains; however, this large tensile strain did not occur in the isolated cases. The LE 5% case shows much smaller strains at the column compared to the hybrid case. Nevertheless, both isolated cases remain in the elastic range for the columns.

Figure 76 shows the hysteric loops in the lateral direction. The fibre remains in compression throughout the seismic event for all three cases due to the dead loads on the columns. Moreover, in all three cases the column fibre remained in the elastic range. The pinned case had the highest strain compared to the isolated cases; however, the difference in strain magnitude is fairly small. The stresses on the fibre in lateral direction is much lower than those of the fibre in the longitudinal direction. This could be due to the shape of the pier frame.

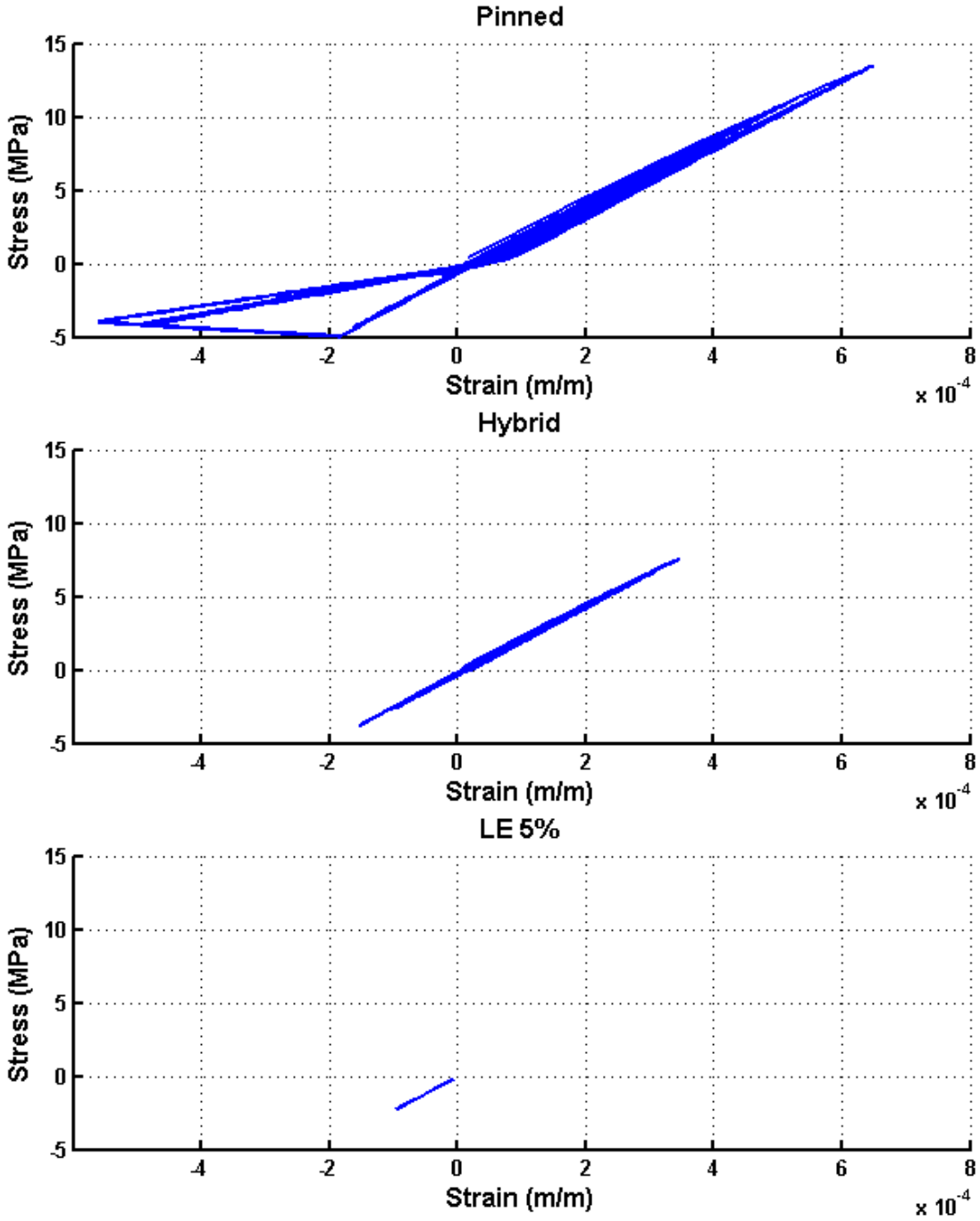

Figure 75. Pier 2 column extreme fibres hysteric loops in the longitudinal direction.

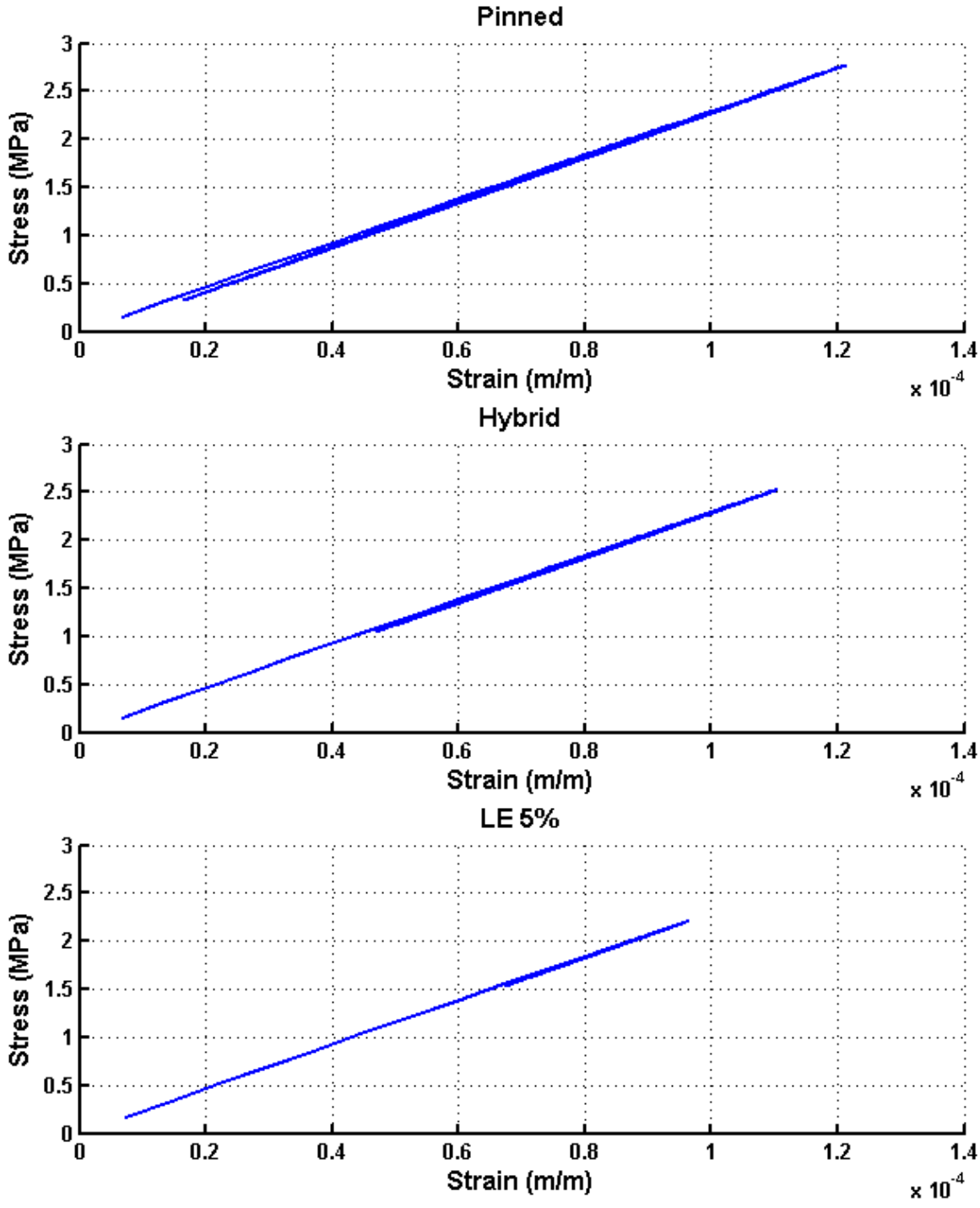

Figure 76. Pier 2 column extreme fibres hysteric loops in the lateral direction.

Chapter 6
Conclusion and Future Work

6.1 Conclusions

This thesis investigated the performance of various retrofit options employing control devices. Specifically, isolation systems in conjunction with fluid viscous dampers were investigated. The Mississippi river bridge near Ottawa was used as the test bed for this study. Hence, the results are specifically applicable to this case. However, some general conclusions can also be drawn for long-span bridges. The relative performance of seven cases of retrofits was assessed and key conclusions obtained. They are as follows:

- Comparing the performance indices for various bridges retrofits show that the vibration isolation bearings can significantly reduce the loads on the substructure of the bridge during a seismic event. This means that employing isolation systems in bridge retrofits can reduce the substructure strengthening needed to upgrade seismically deficient bridges, thereby reducing the overall cost of retrofits. This is a general conclusion, and is consistent with studies performed on other bridges in the literature.

- The isolation systems consisting of the friction pendulum and hybrid bearings (combination of friction pendulum and linear elastomeric bearings) reduced the loads on the piers. However, it failed to distribute the loads evenly between the substructure elements, namely piers and abutments. In these cases, the piers picked up a disproportionate amount of load.

- Using low stiffness linear elastomeric bearings resulted in a better distribution of loads on the substructure which, consequently, reduced the loads on the piers compared to the friction pendulum and hybrid cases.

- Augmenting the linear elastomeric isolation system with viscous dampers resulted in the best overall seismic performance. The loads on the substructure were considerably low, while limiting the displacement amplitudes to relatively low levels. This isolation system can easily be implemented in newly designed bridges as well as for retrofitting existing bridges with elastomeric pads. This could be a very practical, economical and a relatively easy option compared to traditional retrofit methods that are currently being used.
- Among the linear elastomeric cases with supplemental viscous dampers, the linear elastomeric system with 5% damping showed the optimum seismic performance. Increasing the magnitude of damping to 10% and 15% critical reduced the displacements and accelerations of the superstructure, but at the cost of additional loads to the substructure. Hence, the level of damping is an important aspect to be considered for evaluating retrofit design.
- The soil-structure interaction on the isolated bridge systems had only minor influence in the seismic loads of the bridge. However, for the unisolated system the soil-structure interaction reduced the forces dramatically, by 60% in some cases. At the same time, including the effect of soil-structure interaction resulted in high structural deformations, reaching in some cases four times the displacements of the models without soil-structure interaction. Thus, it can be hypothesized that the effect of SSI is not that significant for long-span bridges that are isolated for the soil parameters considered in this considered in this study. However, this effect can be pronounced for short-span, unisolated bridges. This statement needs to be investigated further through additional cases.

6.2 Recommended Areas of Future Work

The main conclusion of this study is that increasing the damping in a bridge at the vibration isolation bearings level reduced the seismic loads transferred to the substructure. However, this result is based on studying a single long highway bridge. A further study that investigates medium and short bridges and evaluates the retrofit effectiveness is necessary to give a general conclusion.

A parametric study that gives the optimum dampers capacities and distribution is also required. The parametric study should provide easy tools that can help designers estimate the dampers capacities to get the optimum load reduction without conducting a time-history analysis. This study should include long, medium and short bridges.

The effect of the SSI on bridges should also be further investigated. In this study, the SSI effect was minor where the bridge was located on stiff saturated clay soil bed. Investigating the effect of SSI due to different soil types can help designers know when to account for SSI and when it is negligible. The SSI study should also be expanded to medium and short bridges on different types of soil beds.

Appendix A

Mode Shapes

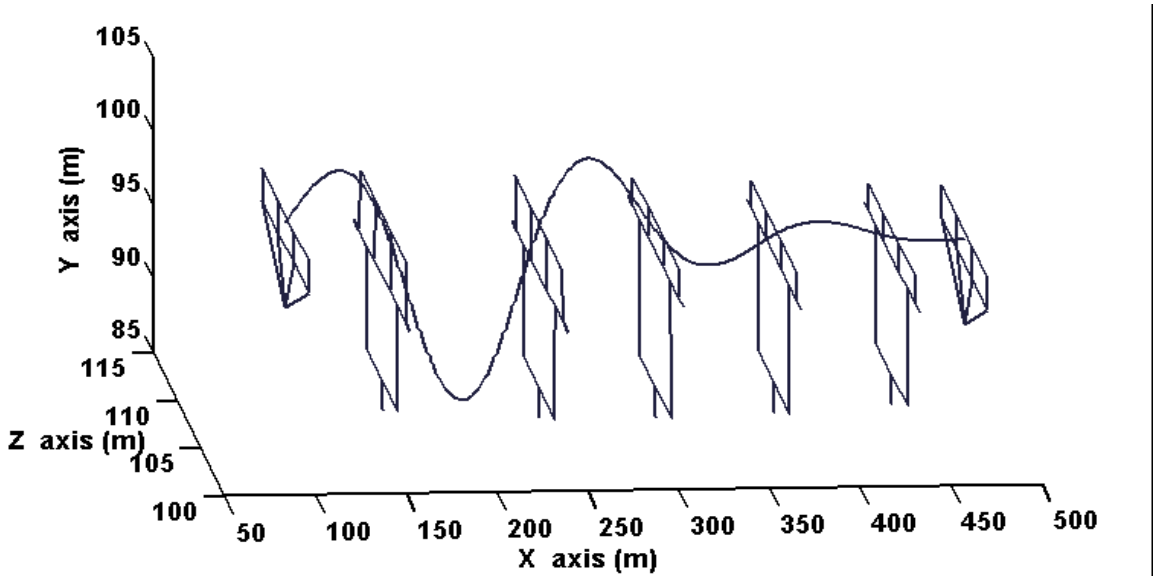

Pinned forth mode of vibration, vertical mode shape (T=0.67).

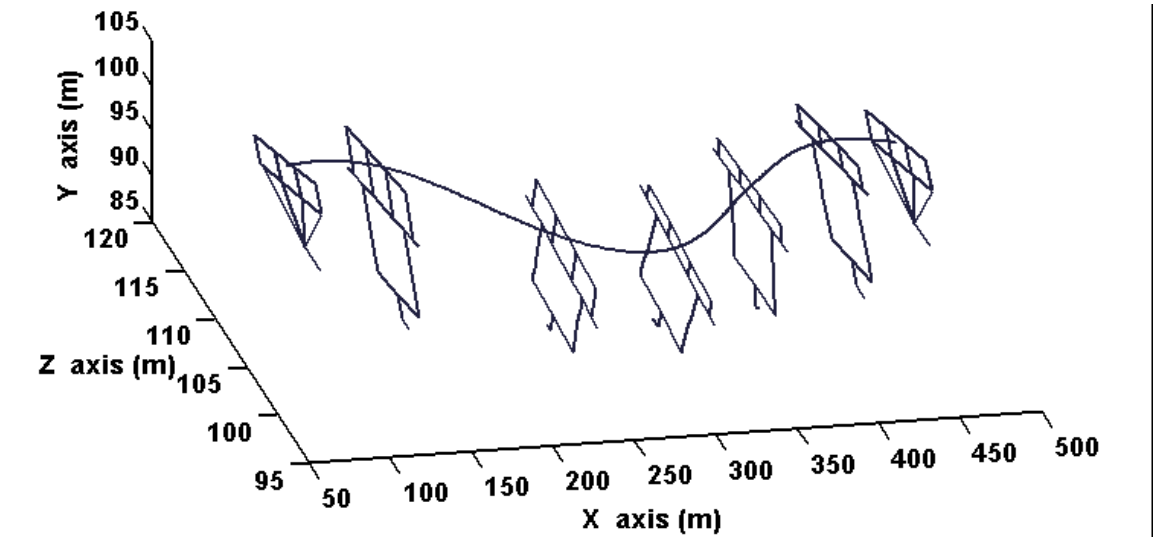

Pinned fifth mode of vibration, transverse torsional mode shape (T=0.52).

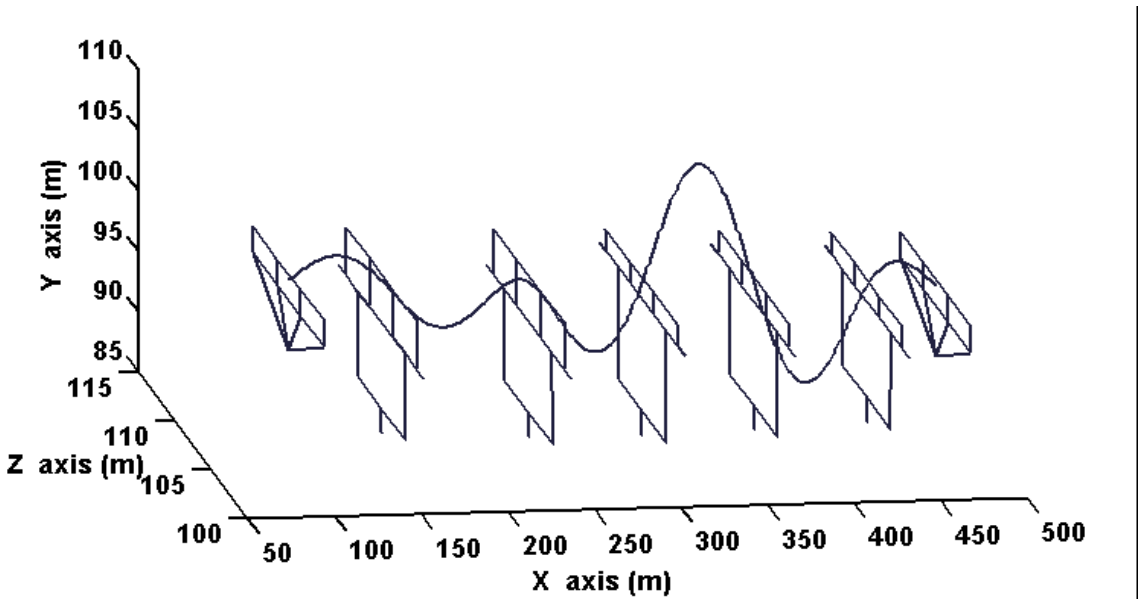

Pinned sixth mode of vibration, vertical mode shape (T=0.48).

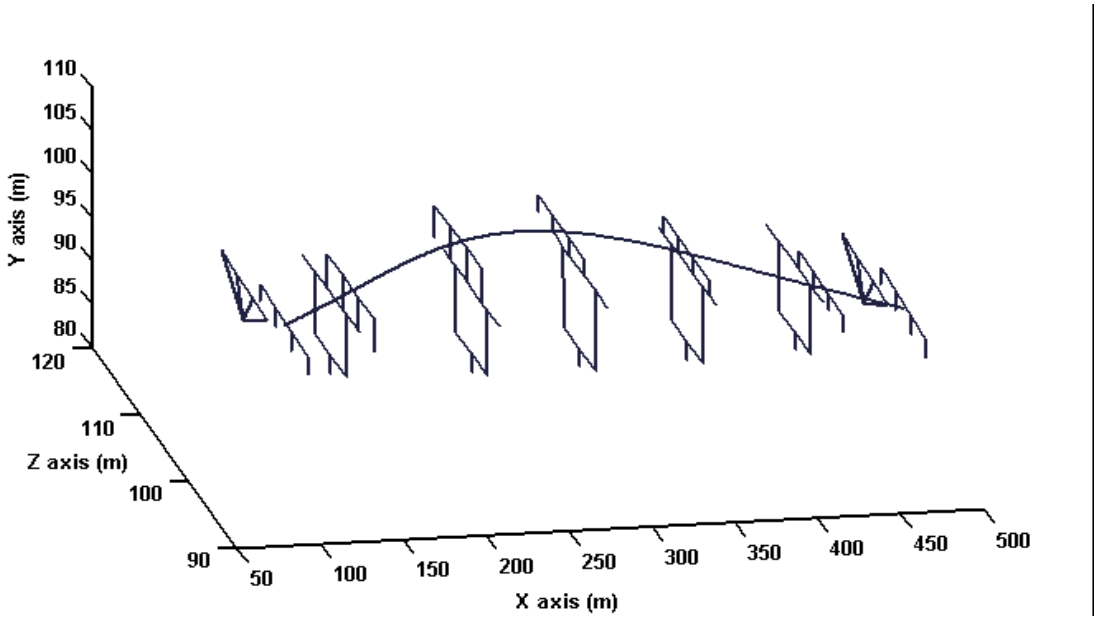

Hybrid forth mode of vibration, transvers bearings deformation (T=0.94).

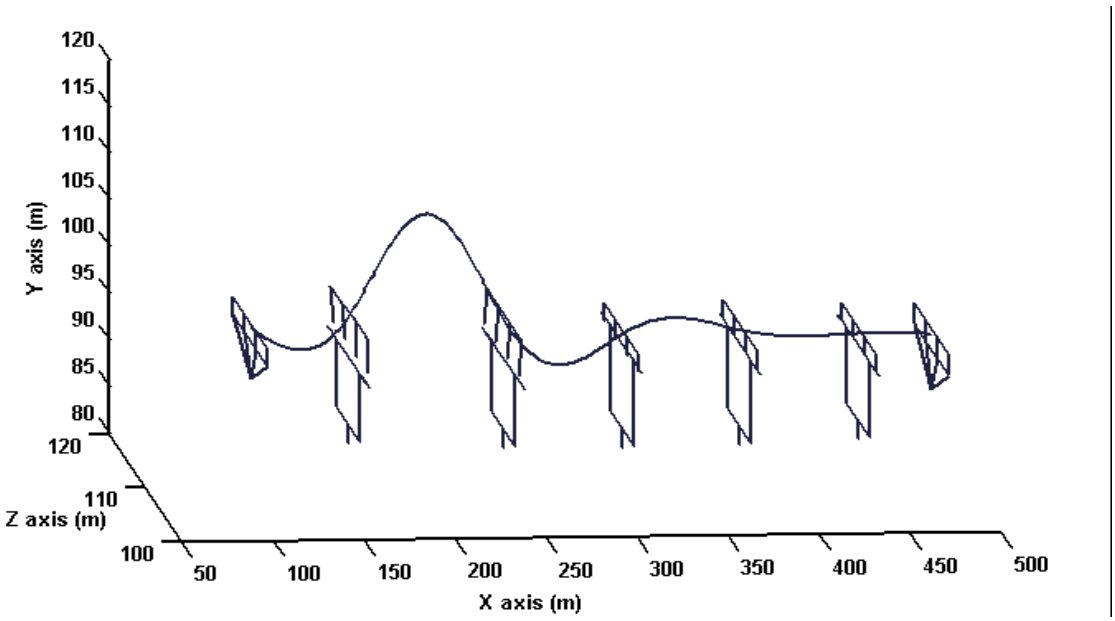

Hybrid fifth mode of vibration, vertical mode shape (T=0.71).

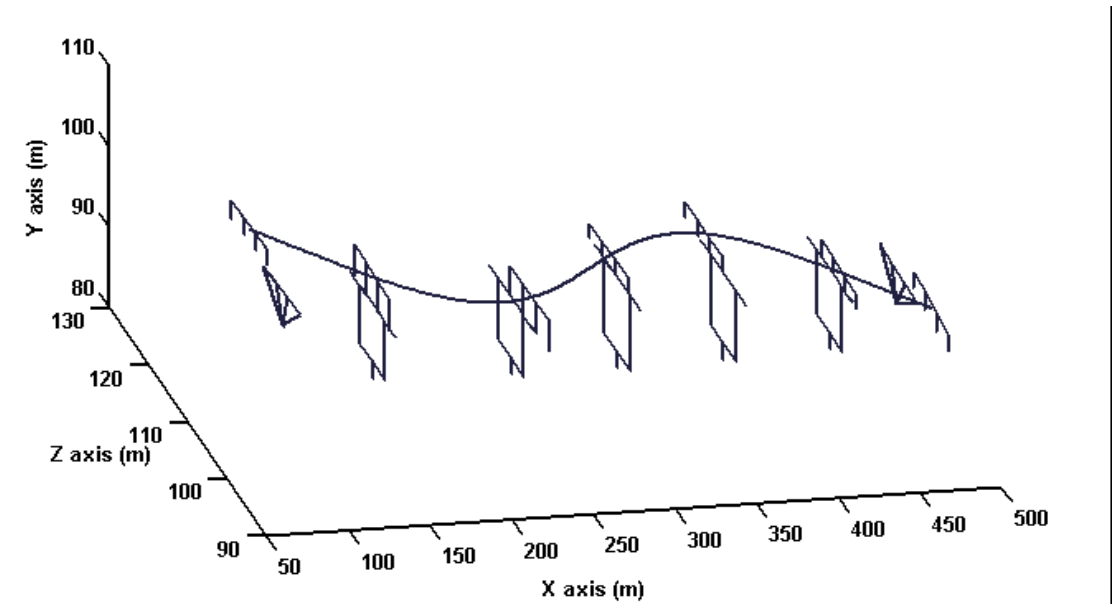

Hybrid sixth mode of vibration, transverse bearing deformation (T=0.61).

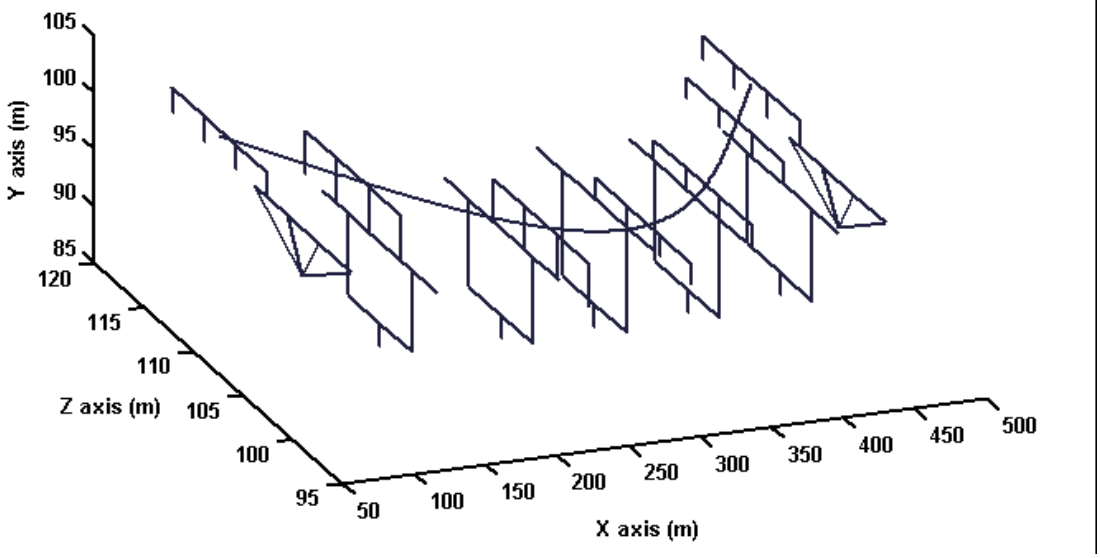

FP forth mode of vibration, transverse bearings deformation (T=0.71).

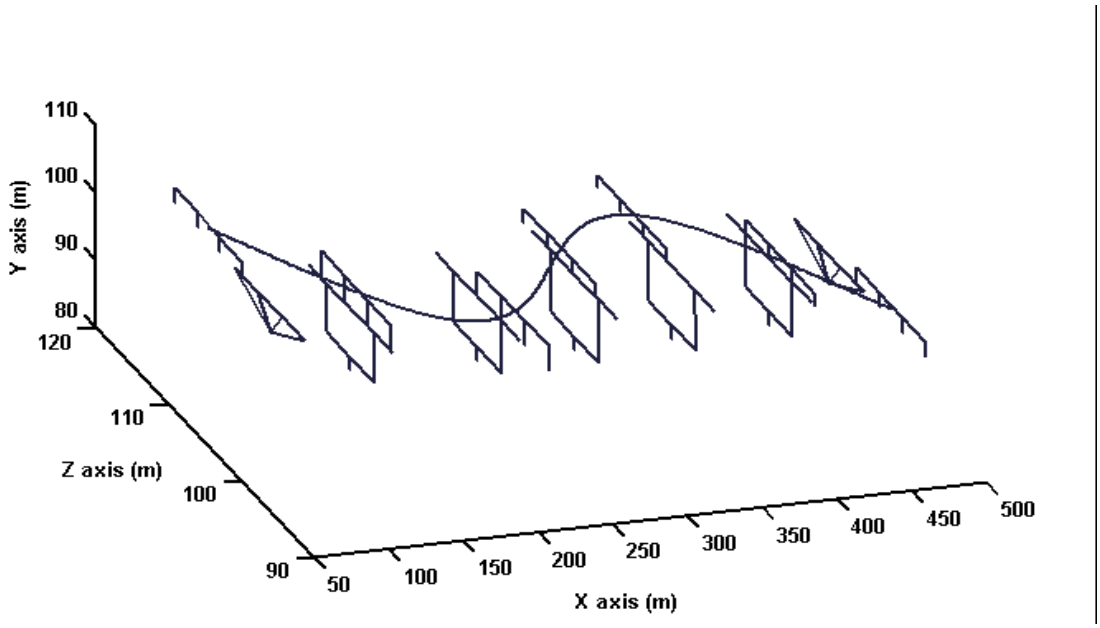

FP fifth mode of vibration, transverse bearings deformation (T=0.63).

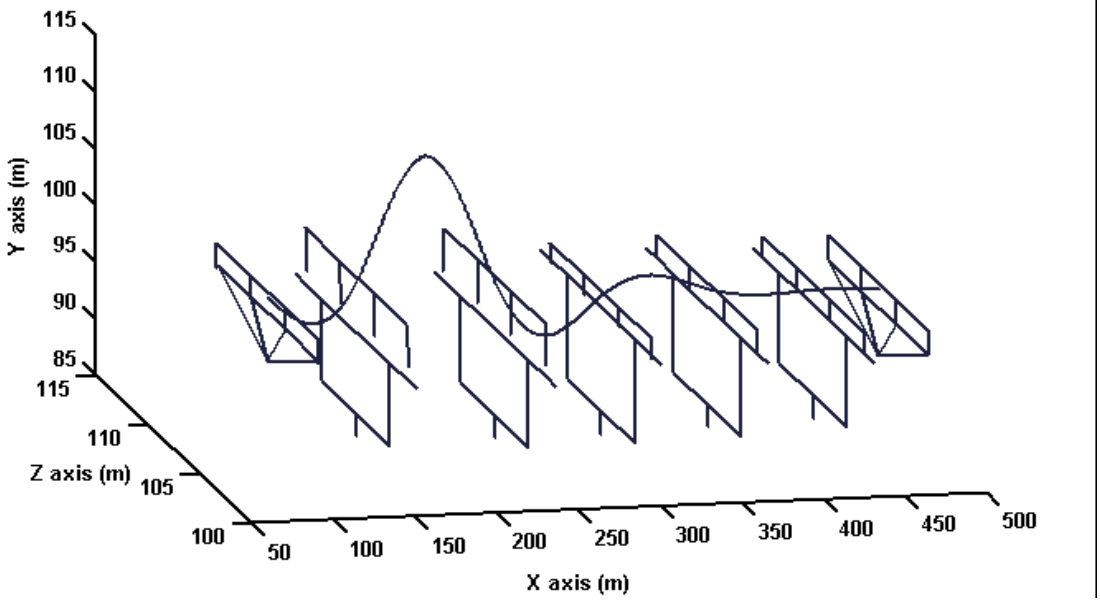

FP fifth mode of vibration, vertical mode shape (T=0.51).

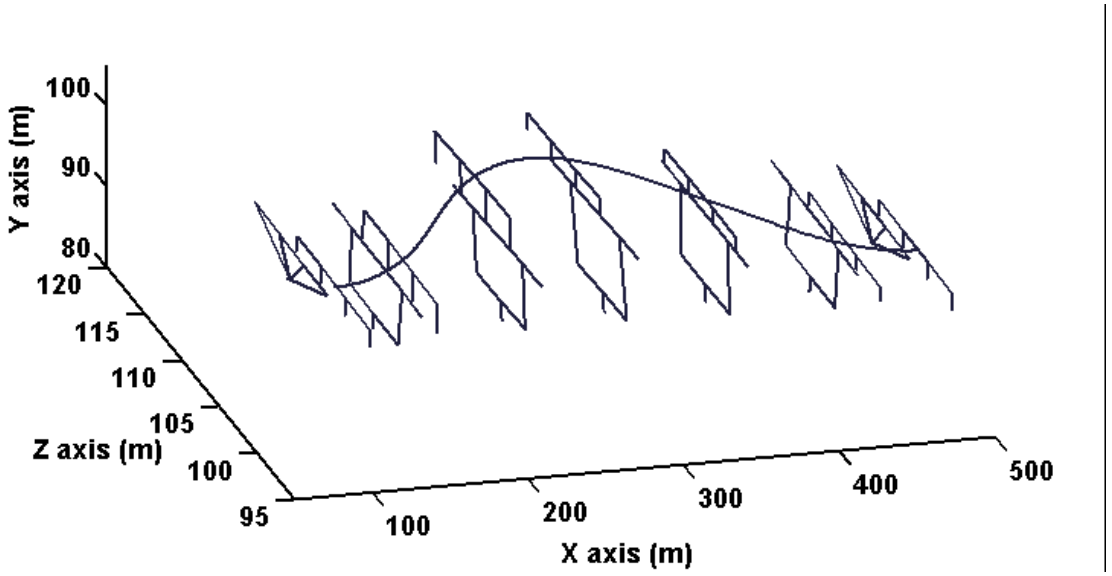

FP sixth mode of vibration, transverse bearings deformation (T=0.79).

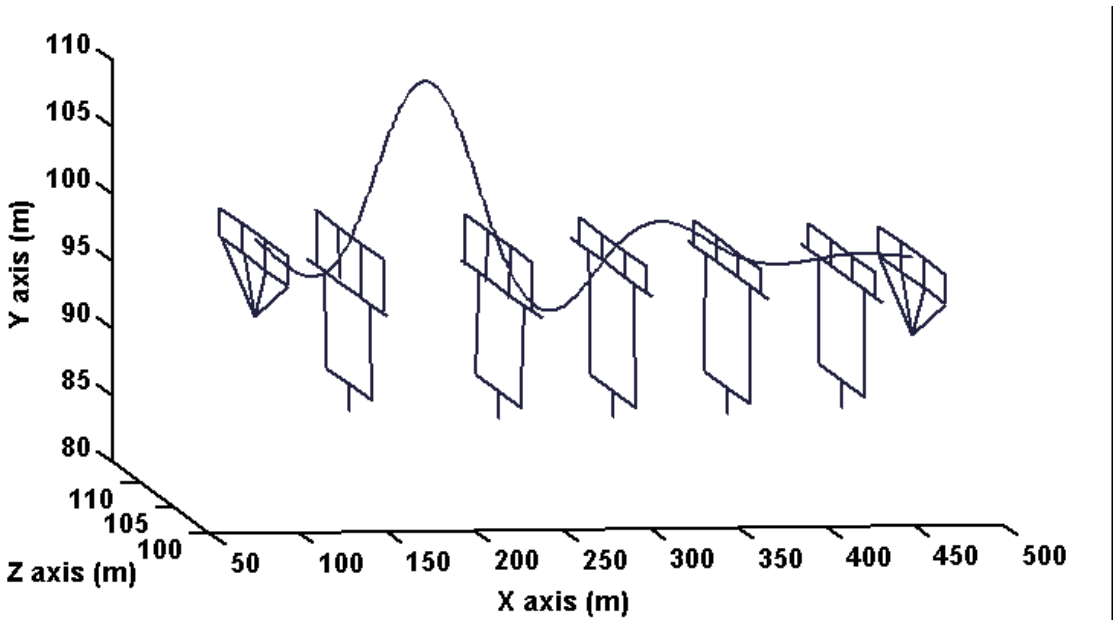

LE fifth mode of vibration, vertical mode shape (T=0.63).

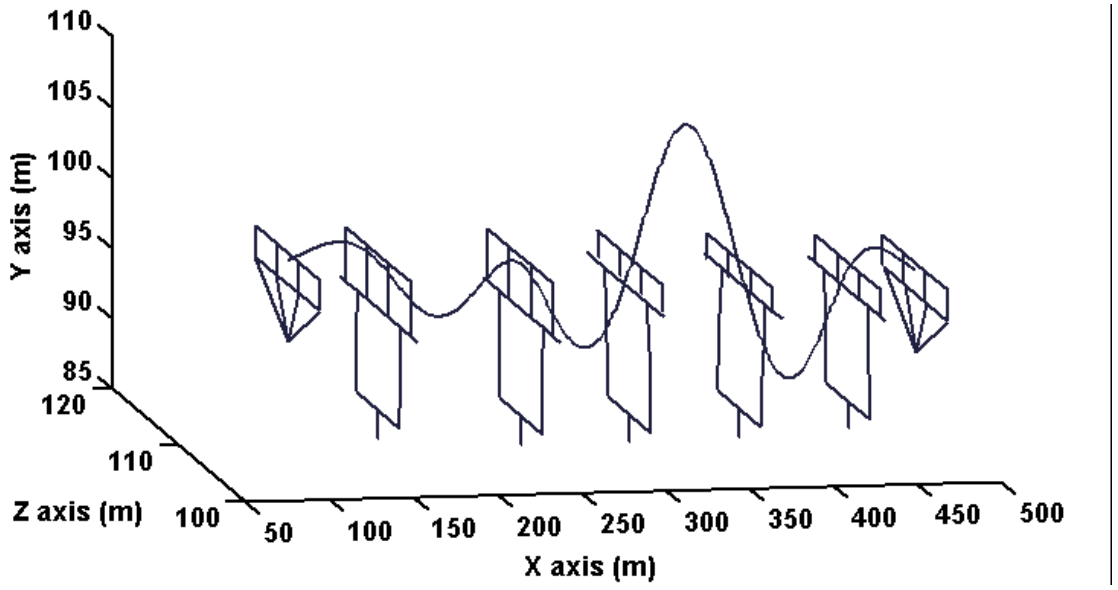

LE forth mode of vibration, vertical mode shape (T=0.45).

Appendix B

Response Indices Tables

Earthquake combination 1 response indices.

	Bridge Type	West Abutment	Pier 1	Pier 2	Pier 3	Pier 4	Pier 5	East Abutment
Peak Base Shear(N)	FP Setup	5.024E+05	1.351E+06	1.603E+06	1.367E+06	1.312E+06	1.154E+06	4.012E+05
	LE Setup	1.199E+06	1.209E+06	1.384E+06	1.278E+06	1.294E+06	1.334E+06	1.232E+06
	LE (5%) Setup	1.059E+06	1.065E+06	1.137E+06	1.055E+06	9.924E+05	1.039E+06	1.073E+06
	LE (10%) Setup	1.623E+06	1.315E+06	1.491E+06	1.402E+06	1.283E+06	1.340E+06	1.630E+06
	LE (15%) Setup	1.950E+06	1.435E+06	1.664E+06	1.569E+06	1.417E+06	1.480E+06	1.953E+06
	Pinned Setup	1.199E+06	2.041E+06	2.685E+06	2.125E+06	1.967E+06	1.858E+06	9.572E+05
	Hybrid Setup	4.143E+05	1.656E+06	1.660E+06	1.370E+06	1.422E+06	1.352E+06	3.388E+05
Peak Overturning Moment (N.m)	FP Setup	2.105E+06	1.377E+07	1.724E+07	1.608E+07	1.465E+07	1.160E+07	1.707E+06
	LE Setup	1.161E+07	1.032E+07	9.647E+06	8.063E+06	7.335E+06	6.763E+06	6.499E+06
	LE (5%) Setup	1.189E+07	9.687E+06	1.049E+07	1.008E+07	8.328E+06	6.246E+06	6.553E+06
	LE (10%) Setup	1.341E+07	1.169E+07	1.356E+07	1.391E+07	1.129E+07	7.288E+06	7.558E+06
	LE (15%) Setup	1.431E+07	1.263E+07	1.508E+07	1.587E+07	1.276E+07	7.783E+06	8.194E+06
	Pinned Setup	6.909E+06	2.014E+07	2.828E+07	2.491E+07	2.178E+07	1.861E+07	5.588E+06
	Hybrid Setup	2.405E+06	1.722E+07	1.793E+07	1.606E+07	1.578E+07	1.416E+07	1.885E+06
Peak Bearing Deformation (m)	FP Setup	0.029	0.018	0.021	0.021	0.017	0.019	0.032
	LE Setup	0.130	0.119	0.137	0.125	0.127	0.131	0.134
	LE (5%) Setup	0.029	0.033	0.030	0.027	0.025	0.024	0.025
	LE (10%) Setup	0.021	0.025	0.020	0.018	0.016	0.014	0.016
	LE (15%) Setup	0.016	0.020	0.017	0.014	0.012	0.011	0.012
	Pinned Setup	0.028	0.000	0.000	0.000	0.000	0.000	0.030
	Hybrid Setup	0.045	0.018	0.023	0.019	0.019	0.022	0.037

Earthquake combination 1 response indices.

Performance Indices	Bridge Setup	Mid-Span 1	Mid-Span 2	Mid-Span 3	Mid-Span 4	Mid-Span 5	Mid-Span 6
Peak Mid-Span Displacement (m)	FP Setup	0.035	0.048	0.052	0.047	0.038	0.032
	LE Setup	0.141	0.141	0.142	0.142	0.142	0.142
	LE (5%) Setup	0.033	0.035	0.037	0.035	0.031	0.029
	LE (10%) Setup	0.024	0.031	0.039	0.035	0.025	0.021
	LE (15%) Setup	0.021	0.032	0.042	0.037	0.025	0.017
	Pinned Setup	0.038	0.056	0.062	0.055	0.042	0.032
	Hybrid Setup	0.052	0.055	0.053	0.048	0.044	0.041
Peak Mid-Span Acceleration (m/s2)	FP Setup	4.289	4.505	4.613	4.475	4.423	4.046
	LE Setup	4.913	4.892	4.873	4.875	4.889	4.896
	LE (5%) Setup	3.629	4.294	4.302	4.268	4.075	3.491
	LE (10%) Setup	3.476	4.282	4.287	4.242	4.022	3.314
	LE (15%) Setup	3.395	4.257	4.250	4.206	3.985	3.273
	Pinned Setup	3.929	4.760	4.771	4.657	4.671	3.904
	Hybrid Setup	4.481	4.566	4.551	4.523	4.452	4.374

Earthquake combination 2 response indices.

	Bridge Type	West Abutment	Pier 1	Pier 2	Pier 3	Pier 4	Pier 5	East Abutment
Peak Base Shear(N)	FP Setup	4.312E+05	1.487E+06	1.508E+06	1.285E+06	1.295E+06	1.142E+06	3.241E+05
	LE Setup	1.010E+06	1.111E+06	9.464E+05	1.011E+06	9.895E+05	9.594E+05	9.402E+05
	LE (5%) Setup	1.059E+06	1.116E+06	1.105E+06	1.168E+06	1.078E+06	9.689E+05	9.643E+05
	LE (10%) Setup	1.254E+06	1.210E+06	1.255E+06	1.308E+06	1.187E+06	1.053E+06	1.147E+06
	LE (15%) Setup	1.361E+06	1.239E+06	1.305E+06	1.355E+06	1.221E+06	1.079E+06	1.255E+06
	Pinned Setup	1.025E+06	1.782E+06	2.300E+06	1.756E+06	1.692E+06	1.651E+06	8.392E+05
	Hybrid Setup	4.384E+05	1.707E+06	1.585E+06	1.303E+06	1.339E+06	1.194E+06	2.840E+05
Peak Overturning Moment (N.m)	FP Setup	2.396E+06	1.513E+07	1.646E+07	1.519E+07	1.462E+07	1.167E+07	1.739E+06
	LE Setup	1.093E+07	8.649E+06	9.396E+06	6.934E+06	6.394E+06	6.383E+06	6.224E+06
	LE (5%) Setup	1.141E+07	8.889E+06	1.238E+07	1.047E+07	8.898E+06	7.671E+06	6.743E+06
	LE (10%) Setup	1.224E+07	9.643E+06	1.382E+07	1.211E+07	1.005E+07	8.026E+06	7.301E+06
	LE (15%) Setup	1.268E+07	9.858E+06	1.428E+07	1.304E+07	1.037E+07	8.008E+06	7.608E+06
	Pinned Setup	5.899E+06	1.752E+07	2.396E+07	2.051E+07	1.880E+07	1.666E+07	4.895E+06
	Hybrid Setup	2.503E+06	1.799E+07	1.734E+07	1.538E+07	1.506E+07	1.224E+07	1.479E+06
Peak Bearing Deformation (m)	FP Setup	0.030	0.014	0.015	0.016	0.012	0.013	0.027
	LE Setup	0.110	0.113	0.096	0.104	0.101	0.098	0.102
	LE (5%) Setup	0.023	0.025	0.028	0.020	0.019	0.020	0.022
	LE (10%) Setup	0.013	0.017	0.019	0.012	0.011	0.012	0.013
	LE (15%) Setup	0.010	0.015	0.016	0.009	0.008	0.009	0.010
	Pinned Setup	0.026	0.000	0.000	0.000	0.000	0.000	0.028
	Hybrid Setup	0.048	0.018	0.018	0.015	0.013	0.016	0.031

Earthquake combination 2 response indices.

Performance Indices	Bridge Setup	Mid-Span 1	Mid-Span 2	Mid-Span 3	Mid-Span 4	Mid-Span 5	Mid-Span 6
Peak Mid-Span Displacement (m)	FP Setup	0.036	0.045	0.048	0.045	0.038	0.032
	LE Setup	0.115	0.116	0.115	0.113	0.111	0.110
	LE (5%) Setup	0.029	0.031	0.037	0.034	0.028	0.025
	LE (10%) Setup	0.021	0.029	0.036	0.032	0.023	0.018
	LE (15%) Setup	0.019	0.029	0.035	0.032	0.022	0.016
	Pinned Setup	0.033	0.046	0.050	0.045	0.036	0.029
	Hybrid Setup	0.052	0.053	0.048	0.044	0.039	0.034
Peak Mid-Span Acceleration (m/s2)	FP Setup	3.074	3.319	3.409	3.328	3.155	2.962
	LE Setup	3.207	3.293	3.371	3.330	3.241	3.179
	LE (5%) Setup	2.793	3.079	3.416	3.247	2.880	2.707
	LE (10%) Setup	2.703	3.064	3.491	3.273	2.811	2.597
	LE (15%) Setup	2.642	3.038	3.506	3.269	2.762	2.534
	Pinned Setup	2.816	3.226	3.667	3.412	2.945	2.691
	Hybrid Setup	3.481	3.431	3.338	3.284	3.242	3.189

Earthquake combination 3 response indices.

	Bridge Type	West Abutment	Pier 1	Pier 2	Pier 3	Pier 4	Pier 5	East Abutment
Peak Base Shear(N)	FP Setup	4.208E+05	1.401E+06	1.377E+06	1.217E+06	1.169E+06	1.068E+06	3.332E+05
	LE Setup	9.317E+05	1.084E+06	9.223E+05	1.020E+06	1.011E+06	9.840E+05	8.830E+05
	LE (5%) Setup	9.078E+05	9.824E+05	9.291E+05	1.004E+06	9.191E+05	8.506E+05	8.553E+05
	LE (10%) Setup	1.204E+06	1.088E+06	1.181E+06	1.170E+06	1.008E+06	9.718E+05	1.082E+06
	LE (15%) Setup	1.405E+06	1.126E+06	1.335E+06	1.308E+06	1.089E+06	1.008E+06	1.202E+06
	Pinned Setup	1.105E+06	2.189E+06	2.231E+06	2.019E+06	1.824E+06	1.630E+06	9.145E+05
	Hybrid Setup	4.123E+05	1.571E+06	1.423E+06	1.195E+06	1.254E+06	1.233E+06	3.170E+05
Peak Overturning Moment (N.m)	FP Setup	2.123E+06	1.325E+07	1.542E+07	1.466E+07	1.336E+07	1.052E+07	1.758E+06
	LE Setup	1.098E+07	1.181E+07	1.211E+07	1.094E+07	9.775E+06	8.434E+06	6.600E+06
	LE (5%) Setup	1.105E+07	8.664E+06	1.081E+07	9.769E+06	8.341E+06	7.227E+06	6.734E+06
	LE (10%) Setup	1.203E+07	1.027E+07	1.411E+07	1.316E+07	1.062E+07	7.812E+06	7.819E+06
	LE (15%) Setup	1.270E+07	1.103E+07	1.592E+07	1.509E+07	1.192E+07	8.113E+06	8.515E+06
	Pinned Setup	6.357E+06	2.134E+07	2.437E+07	2.409E+07	2.059E+07	1.634E+07	5.329E+06
	Hybrid Setup	2.255E+06	1.670E+07	1.544E+07	1.419E+07	1.422E+07	1.287E+07	1.759E+06
Peak Bearing Deformation (m)	FP Setup	0.037	0.022	0.013	0.017	0.016	0.019	0.033
	LE Setup	0.101	0.106	0.091	0.098	0.095	0.092	0.096
	LE (5%) Setup	0.023	0.028	0.031	0.021	0.021	0.025	0.025
	LE (10%) Setup	0.015	0.020	0.022	0.014	0.012	0.016	0.016
	LE (15%) Setup	0.011	0.017	0.019	0.010	0.009	0.013	0.012
	Pinned Setup	0.030	0.000	0.000	0.000	0.000	0.000	0.028
	Hybrid Setup	0.045	0.021	0.012	0.016	0.016	0.019	0.035

Earthquake combination 3 response indices.

Performance Indices	Bridge Setup	Mid-Span 1	Mid-Span 2	Mid-Span 3	Mid-Span 4	Mid-Span 5	Mid-Span 6
Peak Mid-Span Displacement (m)	FP Setup	0.037	0.044	0.048	0.043	0.036	0.036
	LE Setup	0.110	0.116	0.114	0.106	0.104	0.103
	LE (5%) Setup	0.027	0.033	0.039	0.036	0.027	0.027
	LE (10%) Setup	0.020	0.030	0.037	0.033	0.023	0.019
	LE (15%) Setup	0.019	0.032	0.041	0.036	0.024	0.015
	Pinned Setup	0.033	0.052	0.059	0.052	0.039	0.029
	Hybrid Setup	0.048	0.047	0.044	0.042	0.040	0.039
Peak Mid-Span Acceleration (m/s2)	FP Setup	2.523	3.000	3.137	2.928	2.821	2.582
	LE Setup	2.866	2.908	2.901	2.837	2.760	2.769
	LE (5%) Setup	2.367	2.758	2.859	2.786	2.635	2.319
	LE (10%) Setup	2.490	3.079	3.168	3.062	2.843	2.446
	LE (15%) Setup	2.548	3.242	3.342	3.202	2.952	2.492
	Pinned Setup	2.911	3.884	4.183	3.540	3.465	2.892
	Hybrid Setup	2.852	2.815	2.846	2.890	2.952	3.074

Earthquake combination 4 response indices.

	Bridge Type	West Abutment	Pier 1	Pier 2	Pier 3	Pier 4	Pier 5	East Abutment
Peak Base Shear(N)	FP Setup	4.728E+05	1.612E+06	1.501E+06	1.251E+06	1.367E+06	1.274E+06	3.517E+05
	LE Setup	1.023E+06	1.114E+06	1.016E+06	1.050E+06	9.810E+05	9.059E+05	9.167E+05
	LE (5%) Setup	1.277E+06	1.303E+06	1.199E+06	1.258E+06	1.238E+06	1.180E+06	1.204E+06
	LE (10%) Setup	1.464E+06	1.344E+06	1.272E+06	1.320E+06	1.295E+06	1.217E+06	1.382E+06
	LE (15%) Setup	1.573E+06	1.351E+06	1.300E+06	1.341E+06	1.312E+06	1.221E+06	1.484E+06
	Pinned Setup	1.105E+06	2.456E+06	2.376E+06	1.813E+06	1.874E+06	1.923E+06	8.129E+05
	Hybrid Setup	4.157E+05	1.712E+06	1.589E+06	1.324E+06	1.435E+06	1.362E+06	4.091E+05
Peak Overturning Moment (N.m)	FP Setup	2.347E+06	1.532E+07	1.501E+07	1.430E+07	1.491E+07	1.281E+07	1.790E+06
	LE Setup	1.109E+07	9.866E+06	1.220E+07	9.947E+06	8.799E+06	8.082E+06	6.723E+06
	LE (5%) Setup	1.124E+07	8.708E+06	1.226E+07	1.038E+07	9.363E+06	8.897E+06	7.614E+06
	LE (10%) Setup	1.194E+07	8.849E+06	1.397E+07	1.403E+07	1.079E+07	9.143E+06	8.343E+06
	LE (15%) Setup	1.233E+07	9.337E+06	1.567E+07	1.583E+07	1.202E+07	9.196E+06	8.790E+06
	Pinned Setup	6.363E+06	2.318E+07	2.393E+07	2.101E+07	2.072E+07	1.947E+07	4.748E+06
	Hybrid Setup	2.009E+06	1.636E+07	1.586E+07	1.511E+07	1.565E+07	1.371E+07	2.063E+06
Peak Bearing Deformation (m)	FP Setup	0.041	0.022	0.013	0.018	0.017	0.022	0.039
	LE Setup	0.111	0.110	0.099	0.105	0.100	0.094	0.100
	LE (5%) Setup	0.027	0.032	0.027	0.025	0.023	0.019	0.024
	LE (10%) Setup	0.017	0.022	0.019	0.013	0.012	0.012	0.014
	LE (15%) Setup	0.013	0.018	0.016	0.009	0.008	0.009	0.010
	Pinned Setup	0.036	0.000	0.000	0.000	0.000	0.000	0.033
	Hybrid Setup	0.045	0.024	0.014	0.019	0.020	0.025	0.045

Earthquake combination 4 response indices.

Performance Indices	Bridge Setup	Mid-Span 1	Mid-Span 2	Mid-Span 3	Mid-Span 4	Mid-Span 5	Mid-Span 6
Peak Mid-Span Displacement (m)	FP Setup	0.043	0.046	0.044	0.044	0.045	0.043
	LE Setup	0.119	0.124	0.125	0.120	0.113	0.109
	LE (5%) Setup	0.033	0.037	0.041	0.039	0.035	0.032
	LE (10%) Setup	0.024	0.032	0.042	0.037	0.027	0.023
	LE (15%) Setup	0.021	0.034	0.045	0.039	0.025	0.020
	Pinned Setup	0.037	0.045	0.052	0.045	0.041	0.036
	Hybrid Setup	0.047	0.047	0.047	0.048	0.049	0.049
Peak Mid-Span Acceleration (m/s2)	FP Setup	3.179	3.237	3.219	3.204	3.181	3.130
	LE Setup	3.705	3.648	3.509	3.472	3.494	3.471
	LE (5%) Setup	2.976	3.070	3.125	3.035	3.005	2.929
	LE (10%) Setup	2.913	3.092	3.192	3.035	3.005	2.853
	LE (15%) Setup	2.871	3.103	3.384	3.112	3.007	2.803
	Pinned Setup	3.547	3.641	3.987	3.778	3.705	3.524
	Hybrid Setup	3.322	3.324	3.307	3.287	3.266	3.266

Earthquake combination 5 response indices.

	Bridge Type	West Abutment	Pier 1	Pier 2	Pier 3	Pier 4	Pier 5	East Abutment
Peak Base Shear(N)	FP Setup	4.304E+05	1.609E+06	1.518E+06	1.289E+06	1.306E+06	1.165E+06	3.321E+05
	LE Setup	1.320E+06	1.251E+06	1.378E+06	1.270E+06	1.218E+06	1.180E+06	1.142E+06
	LE (5%) Setup	1.079E+06	1.201E+06	1.084E+06	1.120E+06	1.085E+06	1.056E+06	1.022E+06
	LE (10%) Setup	1.211E+06	1.243E+06	1.278E+06	1.341E+06	1.154E+06	1.089E+06	1.145E+06
	LE (15%) Setup	1.366E+06	1.248E+06	1.388E+06	1.447E+06	1.221E+06	1.100E+06	1.291E+06
	Pinned Setup	1.196E+06	2.396E+06	2.141E+06	1.843E+06	1.700E+06	1.876E+06	1.088E+06
	Hybrid Setup	4.684E+05	1.732E+06	1.631E+06	1.299E+06	1.379E+06	1.275E+06	3.945E+05
Peak Overturning Moment (N.m)	FP Setup	2.281E+06	1.515E+07	1.655E+07	1.560E+07	1.437E+07	1.150E+07	1.810E+06
	LE Setup	1.264E+07	1.601E+07	1.537E+07	1.522E+07	1.375E+07	1.150E+07	7.529E+06
	LE (5%) Setup	1.123E+07	1.009E+07	1.190E+07	1.216E+07	9.576E+06	7.645E+06	6.586E+06
	LE (10%) Setup	1.232E+07	9.861E+06	1.425E+07	1.464E+07	1.127E+07	7.438E+06	7.836E+06
	LE (15%) Setup	1.297E+07	9.866E+06	1.550E+07	1.551E+07	1.180E+07	7.629E+06	8.706E+06
	Pinned Setup	6.869E+06	2.209E+07	2.178E+07	2.182E+07	1.881E+07	1.854E+07	6.335E+06
	Hybrid Setup	2.397E+06	1.712E+07	1.689E+07	1.496E+07	1.529E+07	1.312E+07	1.930E+06
Peak Bearing Deformation (m)	FP Setup	0.045	0.028	0.023	0.028	0.024	0.026	0.040
	LE Setup	0.144	0.126	0.138	0.128	0.121	0.117	0.124
	LE (5%) Setup	0.034	0.034	0.026	0.028	0.026	0.022	0.028
	LE (10%) Setup	0.020	0.023	0.019	0.016	0.014	0.012	0.016
	LE (15%) Setup	0.014	0.018	0.016	0.012	0.010	0.010	0.011
	Pinned Setup	0.036	0.000	0.000	0.000	0.000	0.000	0.033
	Hybrid Setup	0.051	0.031	0.024	0.028	0.025	0.029	0.043

Earthquake combination 5 response indices.

Performance Indices	Bridge Setup	Mid-Span 1	Mid-Span 2	Mid-Span 3	Mid-Span 4	Mid-Span 5	Mid-Span 6
Peak Mid-Span Displacement (m)	FP Setup	0.048	0.054	0.057	0.053	0.048	0.044
	LE Setup	0.160	0.167	0.166	0.157	0.145	0.136
	LE (5%) Setup	0.041	0.044	0.043	0.041	0.039	0.036
	LE (10%) Setup	0.027	0.031	0.039	0.034	0.026	0.024
	LE (15%) Setup	0.022	0.031	0.041	0.036	0.023	0.020
	Pinned Setup	0.036	0.046	0.053	0.047	0.036	0.034
	Hybrid Setup	0.054	0.058	0.057	0.055	0.052	0.048
Peak Mid-Span Acceleration (m/s2)	FP Setup	3.416	3.599	3.556	3.383	3.693	3.333
	LE Setup	4.096	4.129	4.093	4.114	4.136	4.078
	LE (5%) Setup	3.310	3.436	3.317	3.334	3.515	3.252
	LE (10%) Setup	3.119	3.309	3.454	3.317	3.427	3.078
	LE (15%) Setup	3.023	3.309	3.512	3.354	3.381	2.996
	Pinned Setup	3.795	3.733	3.907	3.737	3.770	3.679
	Hybrid Setup	3.499	3.545	3.495	3.458	3.437	3.485

Bibliography

Agrawal, A., Tan, P., Nagarajaiah, S., & Zhang, J. (2009). Benchmark structural control problem for a seismically excited highway bridge—Part I: Phase I problem definition. *Structural Control and Health Monitoring, 16*(5), 509-529.

Aiken, I. (1997). An analytical hysteresis model for elastomeric seismic isolation bearings. *Earthquake Engineering and Structural Dynamics, 26*(2).

Atkinson, G. M. A. G. M. (2009). Earthquake time histories compatible with the 2005 National building code of Canada uniform hazard spectrum. *Canadian Journal of Civil Engineering, 36*(6), 991-1000.

Bagnariol, D., & Au, J. (2000). Seismic Assessment of Provincial Bridges *Phase 1 – Preliminary Screening*: Ministry of Transportation of Ontario

Bridge Office

Engineering Standards Branch.

Canadian Standard Association. (2006). Canadian Highway Bridge Design Code S6-06 (CAN/CSA S6-06) *Canada: Canadian Standard Association, Ontario*.

Delis, E., Malla, R., Madani, M., & Thompson, K. (1996). *Energy dissipation devices in bridges using hydraulic dampers*.

Eröz, M., & DesRoches, R. (2008). Bridge seismic response as a function of the Friction Pendulum System (FPS) modeling assumptions. *Engineering Structures, 30*(11), 3204-3212. doi: 10.1016/j.engstruct.2008.04.032

Gazetas, G. (1987). Seismic response of earth dams: some recent developments. *Soil dynamics and earthquake engineering, 6*(1), 2-47.

Ghobarah, A. A., & Tso, W. K. (1973). Seismic analysis of skewed highway bridges with intermediate supports. *Earthquake Engineering & Structural Dynamics, 2*(3), 235-248. doi: 10.1002/eqe.4290020304

Hardin, B. O. (1965). The nature of damping in sands. *Journal of Soil Mechanics & Foundations Div, 92*(SM5, Proc Paper 490).

Idriss, I., Seed, H. B., & Serff, N. (1974). Seismic response by variable damping finite elements. *Journal of Geotechnical and Geoenvironmental Engineering, 100*(Proc. Paper 10284).

Kotsoglou, A., & Pantazopoulou, S. (2007). Bridge–embankment interaction under transverse ground excitation. *Earthquake Engineering & Structural Dynamics, 36*(12), 1719-1740.

Makris, N. (1994). Soil–pile interaction during the passage of rayleigh waves: An analytical solution. *Earthquake Engineering & Structural Dynamics, 23*(2), 153-167. doi: 10.1002/eqe.4290230204

Makris, N., & Chang, S. P. (2000). Effect of viscous, viscoplastic and friction damping on the response of seismic isolated structures. *Earthquake Engineering & Structural Dynamics, 29*(1), 85-107.

Makris, N., & Gazetas, G. (1992). Dynamic pile soil pile interaction. Part II: Lateral and seismic response. *Earthquake Engineering & Structural Dynamics, 21*(2), 145-162.

Makris, N., & Zhang, J. (2000). Time domain viscoelastic analysis of earth structures. *Earthquake Engineering & Structural Dynamics, 29*(6), 745-768.

Makris, N., & Zhang, J. (2001). Seismic response analysis of highway overcrossings including soil-structure interaction: Pacific Earthquake Engineering Research Center, College of Engineering, University of California, Berkeley.

Makris, N., & Zhang, J. (2003). *Structural characterization and seismic response analysis of a highway overcrossing equipped with elastomeric bearings and fluid dampers: a case study*: Pacific Earthquake Engineering Research Center.
Makris, N., & Zhang, J. (2004). Seismic response analysis of a highway overcrossing equipped with elastomeric bearings and fluid dampers. *Journal of Structural Engineering, 130*(6).
Maragakis, E. A., & Jennings, P. C. (1987). Analytical models for the rigid body motions of skew bridges. *Earthquake Engineering & Structural Dynamics, 15*(8), 923-944. doi: 10.1002/eqe.4290150802
Maurer, S. Sliding Isolation Pendulum Bearings, from http://www.maurer-soehne.com/structural_protection_systems/seismic_devices/isolators/sliding_isolation_pendulum_bearings/
McCallen, D., & Romstad, K. (1994). Dynamic analyses of a skewed short-span, box-girder overpass. *Earthquake spectra, 10*(4), 729-755.
McKenna, F., McGann, C., Arduino, P., & Harmon, J. A. (2010). OpenSees Laboratory.
Meng, J. Y., & Lui, E. M. (2002). Refined stick model for dynamic analysis of skew highway bridges. *Journal of Bridge Engineering, 7*, 184.
Mitchell, D. M. D., Paultre, P. P. P., Tinawi, R. T. R., Saatcioglu, M. S. M., Tremblay, R. T. R., Elwood, K. E. K., . . . DeVall, R. D. V. R. (2010). Evolution of seismic design provisions in the National building code of Canada. *Canadian Journal of Civil Engineering, 37*(9), 1157-1170.
Murat Dicleli, P. (2002). Seismic design of lifeline bridge using hybrid seismic isolation. *Journal of Bridge Engineering, 7*, 94.
Naeim, F., & Kelly, J. M. (1999). *Design of seismic isolated structures: from theory to practice*: Wiley.
Nagarajaiah, S., Narasimhan, S., Agrawal, A., & Tan, P. (2009). Benchmark structural control problem for a seismically excited highway bridge—Part III: Phase II Sample controller for the fully base isolated case. *Structural Control and Health Monitoring, 16*(5), 549-563.
Priestley, M. J. N., & Seible, F. (1996). *Seismic design and retrofit of bridges*: Wiley-Interscience.
Seed, H. B., & Idriss, I. (1970). Soil moduli and damping factors for dynamic response analyses: Berkeley, Calif.: University of California.
Seed, H. B., & Idriss, I. M. (1969). Influence of soil conditions on ground motions during earthquakes. *Journal of the soil mechanics and Foundations division, ASCE, 95*, 99-137.
Tatsuoka, F., Iwasaki, T., & Takagi, Y. (1978). Hysteretic damping of sands under cyclic loading and its relation to shear modulus. *Soils and Foundations, 18*(2), 25-40.
Walker, R. A., & Karbhari, V. M. (2007). Durability based design of FRP jackets for seismic retrofit. *Composite Structures, 80*(4), 553-568. doi: 10.1016/j.compstruct.2006.07.003
Yi Meng, J., & Lui, E. M. (2000). Seismic analysis and assessment of a skew highway bridge. *Engineering Structures, 22*(11), 1433-1452. doi: 10.1016/s0141-0296(99)00097-8
Yu, K. (2010). Day 5 Report on Chile Earthquake, from http://www.degenkolb.com/2010/03/22/day-5-report-on-chile-earthquake-by-degenkolb-team-2/
Zhang, J., & Makris, N. (2002). Seismic Response Analysis of Highway Overcrossings Including Soil-Structure Interaction: John Wiley & Sons.